Mechanical Response of Nanocrystalline Ice-Contained Methane Hydrates
Key Role of Water Ice

Cao, Pinqiang; Ning, Fulong; Wu, Jianyang; Cao, Boxiao; Li, Tianshu; Sveinsson, Henrik Andersen; Liu, Zhichao; Vlugt, Thijs J.H.; Hyodo, Masayuki

DOI
10.1021/acsami.0c00972

Publication date
2020

Document Version
Accepted author manuscript

Published in
ACS applied materials & interfaces

Citation (APA)
Cao, P., Ning, F., Wu, J., Cao, B., Li, T., Sveinsson, H. A., Liu, Z., Vlugt, T. J. H., & Hyodo, M. (2020). Mechanical Response of Nanocrystalline Ice-Contained Methane Hydrates: Key Role of Water Ice. *ACS applied materials & interfaces*, *12*(12), 14016-14028. https://doi.org/10.1021/acsami.0c00972

Mechanical Response of Nanocrytalline Ice-Contained Methane Hydrates: Key Role of Water Ice

Pinqiang Cao [1, 2, 3], Fulong Ning [1, 4, *], Jianyang Wu [3, 5, *], Boxiao Cao [2], Tianshu Li [2], Henrik Andersen Sveinsson [6], Zhichao Liu [1, 4], Thijs J.H. Vlugt [7], Masayuki Hyodo [8],

[1] Faculty of Engineering, China University of Geosciences, Wuhan, Hubei 430074, China.

[2] Department of Civil and Environmental Engineering, The George Washington University, Washington, DC 20052, U.S.A

[3] Department of Physics, Jiujiang Research Institute, Research Institute for Biomimetics and Soft Matter, Fujian Provincial Key Laboratory for Soft Functional Materials Research, Xiamen University, Xiamen 361005, China

[4] National Center for International Research on Deep Earth Drilling and Resource Development, Wuhan, Hubei 430074, China.

[5] NTNU Nanomechanical Lab, Department of Structural Engineering, Norwegian University of Science and Technology (NTNU), Trondheim N-7491, Norway

[*]Email: nflzx@cug.edu.cn; jianyang@xmu.edu.cn

[6] The Njord Center, Department of Physics, University of Oslo, Oslo, 0316, Norway

[7] Process & Energy Department, Delft University of Technology, Leeghwaterstraat 39, 2628CB Delft, The Netherlands

[8] Graduate School of Science and Technology for Innovation, Yamaguchi University, Yamaguchi City, Yamaguchi 753-8511, Japan

Email address:

Pinqiang Cao: Pinqiang@cug.edu.cn;

Boxiao Cao: caoboxiao@gmail.com;

Tianshu Li: tsli@gwu.edu;

Henrik Andersen Sveinsson: henrik.sveinsson@me.com;

Zhichao Liu: liuzhichao121215@163.com;

Thijs J.H. Vlugt: T.J.H.Vlugt@tudelft.nl;

Masayuki Hyodo: hyodo@yamaguchi-u.ac.jp;

*To whom correspondence should be addressed: nflzx@cug.edu.cn; jianyang@xmu.edu.cn;

Abstract: Water ice and gas hydrates can co-exist in the permafrost and polar regions on Earth and in the Universe. However, the role of ice in the mechanical response of ice-contained methane hydrates is still unclear. Here, we conduct direct million-atom molecular simulations of ice-contained polycrystalline methane hydrates and identify a crossover in the tensile strength and average compressive flow stress due to the presence of ice. The average mechanical shear strengths of hydrate-hydrate bicrystals are twice as large as those of hydrate-ice bicrystals. The ice content, especially below 70%, shows the significant effect on the mechanical strengths of the polycrystals, which is mainly governed by the proportions of the hydrate-hydrate grain boundaries (HHGBs), the hydrate-ice grain boundaries (HIGBs), and the ice-ice grain boundaries (IIGBs). Quantitative analysis of the microstructure of the water cages in the polycrystals reveals the dissociation and reformation of various water cages due to mechanical deformation. These findings provide molecular insights into the mechanical behavior and microscopic deformation mechanisms of ice-contained methane hydrate systems on Earth and in the Universe.

Introduction

Gas hydrates are ice-like host-guest substances that trap suitable-sized gas molecules in the host hydrogen(H)-bonded water networks of water cages [1-3]. They usually occur as three common structures: structure I (sI), structure II (sII), and structure H (sH) [1,4]. Structurally, one unit cell of an sI hydrate structure consists of 46 H_2O molecules that form eight cages: two small cages (5^{12}) and six large cages ($5^{12}6^2$) [1]. With regard to the sII and sH crystal structures, larger cages, *e.g.*, $5^{12}6^4$ cage in the sII structures and the $4^35^66^3$ and $5^{12}6^8$ cages in the sH structures, have been identified [1,5,6]. Other hydrate structures have also been discovered or predicted, *e.g.*, sT, sK, sIII, sL and EMT [7-11]. Naturally on Earth, gas hydrates dominantly occur in arctic or permafrost regions and continental margins [12-14]. Driven by the abundance and energy significance of sI gas hydrates, their physico-chemical characteristics have been investigated extensively [1,2,15]. To date, the energy (*e.g.*, methane, ethane) stored in natural gas hydrate deposits is conservatively estimated to be approximately twice that of the conventional fossil fuels found on Earth [16,17].

Because of the conditions (*e.g.*, low temperature and high pressure) [14] at which they form, gas hydrates are very sensitive to changes in environmental conditions. Therefore, they can easily be destabilized by changes in the thermodynamic conditions. Furthermore, various external forces destabilize the environmental conditions of the gas hydrates reservoirs, resulting in the geomechanical instability of the gas-hydrate-bearing sediments. The destabilization of gas-hydrate-bearing sediments causes profound negative impacts, *e.g.*, global climate changes [18-20] and geological hazards [21-23]. This clearly suggests that

gas hydrates have practical implications for seafloor stability, safety, and the economics of conventional petroleum development and the future gas recovery from gas hydrate deposits. Thus, in the past few decades, there have been numerous attempts to characterize the mechanical properties of gas hydrates using both experimental and theoretical techniques [24-30]. For example, using laboratory triaxial deformation apparatus, polycrystalline methane hydrates are more creep-resistant than polycrystalline ice under the same conditions [25]. Moreover, they exhibit strain hardening at a higher strain than ice in constant-strain-rate triaxial compressional deformation experiments [27,28]. This hardening phenomenon may be attributed, or partially attributed, to the stoichiometry change (*e.g.*, ex-solution or disproportionation), however, the true reason for this hardening phenomenon remains unclear. Interestingly, strain hardening of methane hydrates was also observed microscopically, due to a lack of long-distance diffusion of methane molecules when methane hydrates are confined to a finite-size area [31]. By using large-scale molecular dynamic (MD) simulations, it was determined that nanocrytalline polycrystalline methane hydrates exhibit pronounced Hall-Petch and inverse Hall-Petch mechanical strength relationships [29], that resemble those of other solid substances [32-35]. Grain boundary (GB) decohesion, GB sliding and hydrate phase transition are mainly responsible for such interesting mechanical behaviors [29]. Previous studies have shown that although gas hydrates and ice are both solid state substances mainly composed of frozen water, there are significant differences in the mechanical behavior between methane hydrates and water ice [25,27,28,36,37]. Although inverse Hall-Petch weakening is also found in nanocrytalline polycrystalline ice [38], the plastic deformation of nanocrytalline ice polycrystals is mainly governed by a combination of strain-induced amorphization, collective GB sliding,

and dislocation nucleation and propagation [38].

Notably, gas hydrates also occur in deep polar glacial ice cores, *e.g.*, the Antarctic ice cores [39-43] and the ice cores from Dye-3 Greenland [44], indicating that gas hydrates can occur accompanied by water ice in low temperature regions on Earth. Gas hydrates may coexist with water ice in other regions of the solar systems and the outer solar systems, *e.g.*, notably icy moons (Titan) of the giant planets, Neptune, and Uranus [45-47]. Recent research shows that the presence of a thin layer of gas hydrates (the most likely methane hydrates), acting as a thermal insulator at the base of the Pluto's ice shell, can elucidate both the long-term occurrence of an buried ocean and the maintenance of ice shell thickness contrasts [48]. Ice-contained gas hydrates is the most likely to occur in this transition area from the ice shell to subsurface oceans. Consequently, understanding the fundamental mechanical behaviors of ice-contained gas hydrates is important for various gas hydrate issues, *e.g.* gas recovery from cold regions on Earth, geological instability in ice-contained gas hydrates reservoir, and planetary evolution scenarios.

To date, very limited investigations have been conducted, which have concentrated on the mechanical properties of gas hydrates containing water ice [49-51]. The results showed that the mechanical strength of laboratory-formed ice-contained methane hydrates increases as temperature decreases and the ice content increases within in the range of 70%-100%, exhibiting an elastoplastic strain hardening behavior. Despite those important findings, the deformation mechanisms of gas hydrates containing water ice remain largely unknown, especially the role of water ice in the mechanical response at the molecular scale is unclear. The molecular-level details of their mechanical instability are not easily determined

through experiments due to the spatiotemporal resolution limits of the-state-of-art experimental techniques; however, these molecular details can be determined using molecular simulation techniques. In this study, for the first time, large-scale molecular simulations based on coarse-grained mW water models were employed to investigate the role of water ice in the mechanical behaviors of polycrystalline methane hydrates containing water ice. Based on our calculation results, we find that water ice plays a key role in the mechanical behaviors of the polycrystals. The mechanical strength of the polycrystals is mainly governed by the proportions of the hydrate-hydrate grain boundaries (HHGBs), the hydrate–ice grain boundaries (HIGBs), and the ice–ice grain boundaries (IIGBs). Our work sheds light on the mechanical behaviors of H_2O-based solid crystals and improves our understanding of the mechanical response of the sediments that contain them, which is needed for safe gas hydrate exploration and exploitation in permafrost regions on Earth. Even more significantly, our findings can be used to predict and understand planetary mechanical stability and evolution of the solar systems and the outer solar systems throughout the Universe, where clathrate hydrates are embedded in a cryosphere of large icy bodies.

Results and Discussion

Microstructures of Bi- and Poly-crystalline Ice-Contained Methane Hydrates

Both naturally occurring and artificial gas hydrates are typically polycrystalline substances, and the crystalline grains within them are cohesively contacted with each other in random crystallographic

orientations. Figures 1a and 1b illustrate the molecular structures of $CH_4@5^{12}$ and $CH_4@5^{12}6^2$ water cages, respectively. The small $CH_4@5^{12}$ and large $CH_4@5^{12}6^2$ molecular water cages are composed of 12 pentagonal faces and 12 pentagonal plus 2 hexagonal faces, respectively. Figure 1c shows the molecular structure of a cubic monocrystalline sI methane hydrate. Figures 1d-f show molecular structures of relaxed ice-ice (II), hydrate-ice (HI) and hydrate-hydrate (HH) bicrystals, respectively, and the grain boundaries (GBs) in these bicrystals are highlighted for clarification. It has been observed that the structures of the GBs depend on crystalline substances and the contacting crystalline planes. As shown in Figure 1d, the water molecules located at the GBs of the II bicrystal form ordered membered rings (green: five-membered ring; purple: six-membered ring; and red: seven-membered ring), indicating that the IIGB is a crystalline-like structure. The formation of defective five- and seven-membered rings is consistent with previous studies [52-54]. However, the GBs of the HI and HH bicrystals are semicrystalline structures (Figures 1e and 1f). New water cages can form and become disorderly distributed in the GBs, in which the 5^{12}, $5^{12}6^2$, $5^{12}6^3$, $5^{12}6^4$, unidentified water and methane molecular structures are highlighted by green, yellow, purple, red, blue and white, respectively. Such semicrystalline structures are consistent with the molecular structures of hydrates formed in the presence of ice [55,56]. Moreover, these results are consistent with the results of previous investigations [29]. Figures 1g-i show perspective views of the molecular structures of 3-dimensional (3D) polycrystals with an average grain size of around 6.58 nm and water ice contents of 100%, 50% and 0%, respectively. For the hydrate structures in the polycrystals, all water cages are initially fully occupied by methane molecules. The methane hydrate in the polycrystals is rendered by either red or yellow to highlight the GBs. The

water ice structures in the polycrystals are colored according to the identified structural phases; the hexagonal, cubic, and unidentified water molecules are rendered by orange, light blue and white, respectively, for clarification. Similar to the bicrystals, defective structures are dominant in the spatial networks of the disordered GBs in the polycrystals. Notably, only a very small amount cubic ice is formed in the IIGBs and HIGBs due to annealing (Figure 1h).

GB Structure-Dependence of Mechanical Properties of Bicrystals

Tensile and Compressive Behavior of Bicrystals

Figures 2a and 2b show the overall uniaxial stress-strain curves of bicrystalline hydrate-ice with different connecting crystallographic planes under both tension and compression loads that are perpendicular to the straight GBs at 223.15 K and 10 MPa, respectively. Three distinct deformation stages caused by tensile strain can be roughly identified in all of the bicrystalline hydrate-ice structures. Initially, in the first deformation stage, all of the bicrystals exhibit linear stress-strain curves, indicating linearly elastic behavior. In the second deformation stage, the tensile stress-strain curves are nonlinear due to significant stretching and dissociation of the H-bonds in the bicrystals. Finally, in the third stage, a sudden drop in the tensile stress to almost zero occurs in the mechanical loading curves, indicating brittle failure of the bicrystals. This is consistent with the mechanical behavior of monocrystalline methane hydrates, hexagonal ice, and II bicrystals at some specific conditions [29,38]. Similarly, such the tensile mechanical response is also observed in HH bicrystals (Figure 2c). Intriguingly, the maximum tensile strength of the HI bicrystals is not strongly related to the connecting crystallographic planes.

However, this behavior is not observed in HH bicrystals, in which the $\{1\,1\,0\}|\{1\,1\,1\}$ GB structure presents a maximum tensile strength of around 530 MPa. Whereas, in the $\{1\,0\,0\}|\{1\,1\,0\}$ GB structure, it is about 405 MPa, which is lower than that of the HI bicrystals. The differences in sensitivity to the connecting crystalline planes between hydrate-ice and hydrate-hydrate bicrystals are mainly attributed to the different water structures at interfacial regions. The grain boundary structures in HI and HH bicrystals are mostly connected with disordered water molecules. Besides the common water cages, such as 5^{12}, and $5^{12}6^2$, some uncommon water cages, *e.g.*, $5^{12}6^3$, can also occur at HI and HH bicrystals. However, the larger water cages (*e.g.*, $5^{12}6^4$) is also observed at hydrate-hydrate grain boundaries in HH bicrystals (Figure 1f). Moreover, more uncommon larger water cages, *e.g.*, $5^{12}6^3$ and $5^{12}6^4$ in HH bicrystals is found than these of HI bicrystals (Figures 1e-1f). More intrinsically, water cage structures are connected with several types of membered rings. Disordered water molecules at grain boundaries can also form membered rings, which is similar to those of the ice-ice grain boundaries (Figure 1d). On the other hand, guest molecules trapped in the polyhedral water cages formed by host water molecules greatly affect the molecular-level structures of the grain boundaries, and water cage occupancy of guest methane molecules will also influence the stability of water cages [29]. The metastable large cages and their occupancy at GBs can partially explain the difference in tensile strength between HI and HH bicrystals. By comparing with previous studies of II bicrystals [38], the ultimate tensile strength of the II bicrystals are higher than those of both the HI and HH bicrystals. This indicates that the GB structures of bicrystalline ice-ice are more mechanically robust than those of HI and HH bicrystals under tension. However, upon pressurization, the HI bicrystals show more complex loading curves. Six deformation

stages were roughly identified according to the loading curves of the HI bicrystals in Figure 2b, demonstrating their more complicated deformation mechanism. The first and second deformation stages are similar to the tensile case. In the third deformation phase, depending on the GB structures of the HI bicrystals, the compressive stresses gradually decrease by approximately 30-60 MPa from the first peak strengths within the finite strain regimes. This differs from the tensile case, in which extreme decreases in stress occur. In the fourth deformation stage, interestingly, the compressive stresses once more increase as the applied strain increases. When the critical strain is reached, the compressive stress reaches at the second peak. However, the mechanical strength corresponding to the second peak is higher than that of the first peak. This is in contrast with the HH bicrystal case (Figure 2d) and demonstrates the distinct plastic deformation characteristics of HI bicrystals. In the fifth deformation stage, much deeper stress drops are observed, implying significant plastic deformation. Finally, the mechanical loading curve of the last deformation stage is characterized by a nearly constant compressive flow stress. In comparison, the maximum compressive strength of the HH bicrystals are higher than those of the HI bicrystals, but they are comparable to those of the II bicrystals [38]. Figure 2e shows the corresponding tensile and compressive elastic moduli of the HI bicrystals. It is observed that the elastic modulus of the HI bicrystals varies from around 6.2 to 7.5 GPa, depending on the relative contributions of the GB accommodation structure and the bulk of the crystals. The Young's modulus was determined by linearly fitting the stress-strain curves in the elastic strain regime (See Supplementary Materials sections S4. Mechanical Parameters). With regard to the HH bicrystals, the elastic modulus ranges from 6.75 to 7.5 GPa (Figure 2f). Both the HI and HH bicrystals are elastically softer than the ice and

methane hydrate monocrystals [29,31,57,58], as well as the II bicrystals [38]. The asymmetry of tension-compression responses in the molecular structures in these bicrystals mainly explains the large difference of Young's modulus between tension and compression loads for some cases, such as HI bicrystals with $\{11\bar{2}0\}|\{1\,1\,0\}$, $\{0\,0\,0\,1\}|\{1\,1\,0\}$, and $\{01\bar{1}0\}|\{1\,0\,0\}$ GB structures.

In order to reveal the mechanical deformation mechanism, several typical structures of one hydrate-ice bicrystal with a $\{01\bar{1}0\}|\{1\,0\,0\}$ GB structure were captured under mechanical straining (See Figures 2g-2i, and Supplementary Materials Figure S1). Under elastic tension and compression, the first deformation stage is mainly characterized by misshapen water cages in the hydrates and hexagonal ice lattices, as well as the GB accommodation. In the second deformation stage, significant changes in the GB structures are dominant. It can be observed that the latticed water ice at the GBs is more easily dissociated than that of the water cages in the hydrates. However, after the bicrystals yield, there are differences in the plastic deformation characteristics. Apparently, separation of the bicrystal occurs at the GBs as the tensile strain becomes greater than the yield strain, resulting in the release of the methane molecules trapped at the GBs (Figure 2g, Supplementary Materials Figure S1a, and Movies S1-S2). Such tension induced direct separation is also observed in other HI bicrystals (Supplementary Materials Movies S5 and S7) and all HH bicrystals (Supplementary Materials Figure S2a, Movies S9, S10, S13, and S15). For the compressive load case (See Supplementary Materials Figure S1b and Movies S3-S4), more complicated structural changes occur to eliminate the mechanical stress as indicated by the loading curves of Figure 2b. Intriguingly, the latticed ice of the bicrystals firstly destabilizes by fracturing

(Figure 2h) when the applied compressive strain becomes larger than the strain at the first mechanical peak stress, which corresponds to the third mechanical stage (Figure 2b). This indicates that sI methane hydrates are more mechanically robust than hexagonal ice at low temperature from our deformational simulations, which is in agreement with the results of previous theoretical and experimental investigations [25,29]. Moreover, the rotation of the fractured ice and the emission of the dislocations in the fractured ice are found at the same time. The dislocations highlighted by solid colored segments are mainly identified as $1/3\langle 1\ \bar{2}\ 1\ 0\rangle$ (See Supplementary Materials Figure S1b and Movies S4). This results in the distinct recovery of the mechanical stress in the fourth deformation stage. The appearance of two peak stresses can be attributed to the different mechanical strengths between monocrystalline hydrate and hexagonal ice. The higher second peak in mechanical strength than the first peak ones mainly results from the higher mechanical strength of the monocrystalline hydrate, the dislocation nucleation in the ice part, and the lattice reconstruction of the ice. Then, further compression leads to fracturing and amorphization of the hydrate in the HI bicrystals, which is accompanied by the amorphization of the hexagonal ice (Figure 2i, and Supplementary Materials Movies S3-S4). Similar structure changes were also be found in other HI bicrystals (See Supplementary Materials Movies S6, S8). For HH bicrystals under compression, crystal cleavage occurs on both sides of bicrystals under compression (See Figure S2b, Supplementary Materials Movies S11-S12, S14, and S16) after the drop of the mechanical stress (Figure 2d).

Shear Behavior of Bicrystals

Figure 3a exhibits the mechanical shear stress-strain curves of the hydrate-ice bicrystals. Three deformation stages can be concluded. Initially, all of the HI bicrystals show linearly elastic shear response. However, the shear elasticity strongly depends on the GB structure. By comparison, the HI bicrystal with a $\{11\bar{2}0\}|\{1\,0\,0\}$ structure exhibits the highest mean shear modulus along the $\frac{(1\,1\,\bar{2}\,0)[0\,0\,0\,1]}{(1\,0\,0)[0\,1\,0]}$ direction, while the one with a $\{0\,0\,0\,1\}|\{1\,0\,0\}$ structure shows the lowest mean shear modulus along the $\frac{(0\,0\,0\,1)[0\,1\,\bar{1}\,0]}{(1\,0\,0)[0\,1\,0]}$ direction. The second deformation stage is characterized by the drop of the shear loading stress, indicating failure of the bicrystals. Overall, the average shear strength of the HI bicrystals is around two times lower than that of the HH bicrystals (See Supplementary Materials Figure S3a), indicating that the HHGBs and HIGBs have distinct cohesive forces. Finally, the shear loads of the bicrystals are featured by sawtooth-like shear stress-strain curves. Oscillations in the shear strength are detected during the shear deformation stage, suggesting that the bicrystals undergo a series of repeating local shear strain and stress relaxation processes. Such mechanical behaviors are also observed in the HH bicrystals (See Supplementary Materials Figure S3a). This is in good agreement with the mechanical shear behaviors of ice-ice bicrystals along the $\frac{(1\,1\,\bar{2}\,0)[0\,1\,\bar{1}\,0]}{(0\,0\,0\,1)[0\,1\,\bar{1}\,0]}$, $\frac{(1\,1\,\bar{2}\,0)[0\,0\,0\,1]}{(0\,1\,\bar{1}\,0)[0\,0\,0\,1]}$, and $\frac{(0\,0\,0\,1)[1\,1\,\bar{2}\,0]}{(0\,1\,\bar{1}\,0)[1\,1\,\bar{2}\,0]}$ directions [38]. By comparison, the average shear strength of the HI and HH bicrystals can be either higher or lower than those of the II bicrystals [38], which can be partially attributed to the difference in the crystal face binding energy (See Supplementary

Materials Figure S24). On the other hand, the shear strength of ice-ice bicrystals is closely related to the shear directions [38]. Figures 3b-3g show the typical structural evolutions of the HI bicrystals with $\{11\bar{2}0\}|\{1\,0\,0\}$GB structures subjected to $\frac{(1\,1\,\bar{2}\,0)[0\,1\,\bar{1}\,0]}{(1\,0\,0)[0\,0\,1]}$directional shear load. A specific region covering hydrate, GBs and ice is highlighted by gray to reveal shear deformation characteristics. Grain boundary sliding is detected and indicated by the highlighted region (Figures 3d, 3g, and Supplementary Materials Movies S17-S18), This shows that grain boundary sliding is responsible for the relaxations in the sawtooth-like fluctuations of the shear strength on the loading curves. The GB sliding is accompanied by reformation and dissociation of membered rings (*e.g.* five-, six-, seven- membered rings) at the GBs, indicating the subsequent healing of the interface. Unlike the tension case, the thickness of the GBs does not change during GB sliding. GB sliding is also detected in the HH bicrystals (See Supplementary Materials Figures S3b-g, and Movies S19-S20).

Mechanical Behavior of Ice-Contained Hydrate Polycrystals

GB Microstructure of Ice-Contained Polycrystalline Methane Hydrates

Both polycrystalline methane hydrate and ice have complex 3D network grain boundaries, which are mainly composed of H-bonded water structures. Previous investigations have shown that polycrystalline methane hydrates have different mechanical characteristics from polycrystalline ice [29,38]. Experimental observations using a field-emission scanning electron microscope (FE-SEM) revealed clear IIGBs, HIGBs and HHGBs in micrometer-sized polycrystals with polyhedral faces [59,60]. Figure 4 shows the

cross-sectional snapshots of hydrate polycrystals with 50% water ice. The centro-symmetry parameter (CSP) is employed to differentiate hydrate grains, water ice grains, and GBs. As shown in Figures 4a and 4b, the water molecules in GBs of the polycrystals show different CSP values with those in the crystalline grain interiors, indicating different local lattice disorder between the GBs and crystalline grain interiors. The distribution of the molecular potential energy and the *von Mises* stress in the polycrystals reveals that the GBs possess higher potential energies and are higher stress-concentrated than the internal crystalline grains (Figures 4c-f). Figures 4g-i show the typical localized relaxed microstructures of the IIGBs, HIGBs and HHGBs in the polycrystals, respectively. The GBs in the polycrystals are similar to the bicrystals after relaxation with MD.

Tensile and Compressive Properties of Ice-Contained Hydrate Polycrystals

Figures 5a and 5b show the uniaxial tensile and compressive stress-strain curves of methane hydrate polycrystals containing different water ice contents at 223.15 K and 10 MPa, respectively. Both the tensile and compressive mechanical response are significantly different from those of the HI and HH bicrystals. Similar to those of conventional polycrystalline pure metals, ices, and methane hydrates, our results suggest that the topology and density of the GBs play a crucial role in the mechanical behavior of ice-contained hydrate polycrystalline solids. Ice-contained hydrate polycrystals show ductile mechanical characteristics. Furthermore, for example, the polycrystals with 0% ice content contain the 3D network grain boundaries as shown in Figures 5g-5i. Therefore, the stress-strain response of polycrystals with 0% ice content is closely related to the synergistic response of 3D network grain boundaries. In contrast, the

HH bicrystals have only one hydrate-hydrate grain boundary. Such difference in the grain boundaries can account for the different stress-strain response of polycrystals with 0% ice content (Figure 5) and the HH bicrystals (Figure 2). Upon tension, either four or five distinct deformation stages can be roughly identified, depending on the water ice content. Initially, ice-contained hydrate polycrystals exhibit a linearly elastic response under both tensile and compressive loads. Subsequently, the slopes of the stress-strain curves decrease gradually with increasing mechanical strain, and the maximum mechanical strengths reach the critical strains. This is due to the fact that coupled elastoplastic deformation occurs instead of nonlinear elastic deformation, due to the spatial network of the GBs. Intriguingly, the reduction in mechanical stiffness is closely related to the ice content of the polycrystals. Polycrystals with a low ice content are more mechanically robust than those with a high ice content. The third deformation stage is characterized by a clear drop of tensile stress on the mechanical loading curves, indicating significant structural changes in the polycrystals. In the fourth deformation stage, the post-peak stress-strain curves of polycrystals with a high water ice content exhibit a long-range strain-hardening (*e.g.*, strain ranging from about 0.1 to 0.25 for 100% water ice content) behavior. However, polycrystals with a low water ice content exhibit an initially short-range strain-hardening (*e.g.*, strain ranging from about 0.1 to 0.15 for 0% water ice content) behavior, and then, they exhibit a strain-softening behavior corresponding to the last deformation stage of polycrystals with a low water ice content, similar to the tensile failure as shown in Figure 2a and 2c. In sharp contrast, upon compression, three distinct deformation stages are identified. The first and second deformation stages are similar to the tension case. In the last loading stage, all of the polycrystals deform with a monotonic

strain-softening. Both the maximum tensile and compressive strengths are lower than those of the monocrystalline ice, methane hydrates, and hydrate-ice bicrystals. This is because polycrystals contain a high density of 3D grain boundary structures.

Figures 5c and 5d are plots of the maximum tensile strength and average compressive flow strength as a function of the ice grain content of the polycrystals, respectively. Although the polycrystals are mainly composed of water molecules, they exhibit significantly distinct mechanical performances, which strongly depend on the ice content (See Supplementary Materials Table S1 and Figure 5). The polycrystals are mechanically weakened when water ice is present. This indicates that, at low temperature, the geo-mechanical performance of gas hydrate reservoirs become weakened when water ice forms. Intriguingly, transitional behavior is observed in both the maximum tensile and compressive flow stresses of ice-contained hydrate polycrystals. For ice contents of 0% to 70%, the polycrystals are monotonically weakened for maximum tensile and compressive flow stresses of around 410 to 230 MPa and 425 to 305 MPa, respectively. However, as the polycrystals become dominated by ice grains (> 70%), they are strengthened for maximum tensile and compressive flow stresses of around 230 to 250 MPa and 305 to 310 MPa, respectively. This strengthening behavior was also observed in experiments conducted on the mechanical strength of polycrystals with ice content of 70% to 100% [49]. By comparing the two critical structures, in other, polycrystals composed of 100% nanocrystalline ice and 100% nanocrystalline hydrate, we determined that the polycrystalline methane hydrates have a higher mechanical strength than polycrystalline ice, which is in good agreement with the experimental findings

where the crystalline grains are micron to millimeter-sized [25]. However, it is noted that, as a result of limitations of MD technique, our simulations reveal the mechanical behaviors of icing water-based nanostructures under a high deformation rate. More importantly, these findings could provide the detailed information at microscopic scale for the mechanical behaviors of methane hydrates containing water ice. Due to the fact that the mechanical strength of polycrystalline materials closely depends on grain size, grain morphology, and grain boundary structure, for example, the polycrystalline methane hydrates exhibit a Hall-Petch effect as the grains are larger than a critical size [29]; and the Hall-Petch effect is also experimentally found in polycrystalline ice [33,61]; and the polycrystalline methane hydrates and ice both show an inverse Hall-Petch effect when the grains are smaller than a critical size [29,38]. To show the converged results as the models are enlarged, a large number of works should be carried out in the future.

Our molecular simulations indicate that the mechanical strength of ice-embedded hydrate polycrystals significantly depends on the ice content. Surprisingly, we find that an apparent crossover in both the tensile strength and the average compressive flow stress. This transitional behavior can be mainly attributed to the 3D network GBs and the proportions of IIGBs, HIGBs, and HHGBs in the polycrystals. In general, as shown in Figure 5e, we find that the percentages of IIGBs, HIGBs, and HHGBs in the polycrystals are changing with the changing ice content. For example, the percentages of IIGBs, HIGBs, and HHGBs are approximately 33.62%, 62.23%, and 4.15%, respectively in a given polycrystal with an ice content of 70%. This corresponds to the weakest mechanical strength of the polycrystals with an ice

content of 70% in our molecular simulations. Furthermore, taking into account mechanical strengths of GBs as shown in Figure 5f, these results offer a reasonable explanation for the transitional behavior in the mechanical strength of the polycrystals. The HIGBs have the lowest average shear strengths, whereas the HHGBs have the highest average shear strength. Moreover, our investigations of bicrystals show that the average shear strength of the HH bicrystals is around two times higher than that of the HI bicrystals. However, the IIGBs have an average shear strength intermediate between those of the HHGBs and HIGBs. The IIGBs also exhibit the largest fluctuations in shear strengths, ranging from about 30 MPa to 200 MPa, depending on the combinations of ice crystal planes. For a given 3D polycrystal containing a similar number of crystalline grains, as the ice content increases, the proportion of HHGBs in the 3D networked GBs decreases, and the proportion of IIGBs increases. Therefore, the distinct cohesive forces between the HHGBs and HIGBs and the proportions of the IIGBs, HIGBs, and HHGBs are most likely responsible for the decrease in the maximum tensile and compressive flow stresses as the ice content increases from 0 to 70%. The higher mechanical strengths of the IIGBs than those of the HIGBs, the largest proportion of the IIGBs, and the dislocation nucleation in the ice grains mainly account for the increasing mechanical strength, rather than weak GB sliding induced by shear forces. In the polycrystalline samples, the 3D networks of GBs are very complex. The quantitative changes in the mechanical strengths of ice-embedded hydrate polycrystals significantly depend on the percentages of the IIGBs, HIGBs, and HHGBs. In nature, more or less structured water always occurs between hydrates and sediment minerals [62,63]. The water adsorbed on mineral surfaces possesses extreme densities, and the water in the first adsorbed layer shows low chemical potential. These implies a

mechanical stability limit of gas-hydrate-bearing sediments. Future studies, *e.g.*, the interface mechanics between hydrates and minerals, are inspired. Figures 5g-i show the typical localized structures captured from the polycrystals with an ice content of 50% in the initial state and relaxed state. Different GBs are clearly clarified. These results can help us to understand the 3D network of GBs.

Deformation Mechanisms in Ice-Contained Hydrate Polycrystals

To further reveal the deformation mechanisms responsible for the mechanical stress-strain response of polycrystals under mechanical straining at the molecular level, microstructural developments of a hydrate polycrystal with an ice content of 50% are captured and shown in Figure 6. The initial elastic mechanical response of the polycrystals primarily results from the stretching of the crystalline methane hydrate, the ice grains, and the accommodation of the complex GBs. The following non-elastic response of the hydrate-ice polycrystals mainly comes from deformational changes in the microstructural morphology of the polycrystals, involving GBs such as HIGBs, HHGBs, and IIGBs, and the phase transformation of ice. Under tension, the remarkable strain-softening behavior following the maximum tensile stress is mainly explained by collective GB sliding (Figures 6a-6f). Intriguingly, as a result of the shear forces, both the ice and hydrate grains are able to rotate in the strain-softening stage (Figure 6j). Ice-contained hydrate polycrystals mainly show intergranular failure behavior, emitting from the GB junctions (GBJs). As the tensile strain is increased by the rapid GB sliding, nano-voids develop at the GBJs (Figures 6c and 6f). These structural response leads to the release of the applied elastic strain in the nanocrystalline grains. The slight strain-hardening behavior that occurs after the rapid

strain-softening behavior of hydrate polycrystals with water ice contents of 40%-100% (Figure 5a). This strain-hardening behavior is mainly attributed to the nano-grain arrangements and the phase transformation of ice. For example, a given pure ice polycrystal has approximately 10265, 13463, and 14720 water molecules in cubic ice form at the strains of 0.15, 0.20, and 0.25, respectively (See Supplementary Materials Figure S25). The strain-hardening behavior observed in II bicrystals with $\{1\ 1\ \bar{2}\ 0\}\,|\,\{0\ 0\ 0\ 1\}$ structure along the $\frac{(1\ 1\ \bar{2}\ 0)[0\ 0\ 0\ 1]}{(0\ 0\ 0\ 1)[1\ 1\ \bar{2}\ 0]}$ direction also results from the shear strain-induced large-scale structural transition from the stable hexagonal phase to the metastable cubic phase [38]. Upon compression, the collective GB sliding also results in the strain-softening behavior (Figures 6g-6i). Moreover, the phase transformation of ice is also observed in the compressive ductile flow stage. Under larger compressive strains, the crystalline grains diminish in size and the number of disordered water and methane molecules at the GBs and GBJs increases. The latticed destruction of the nano-grains initially takes place near the GBs and GBJs, and then, it propagates into the interior of the grains. The polycrystals are further mechanically weakened because the water-dominated structures are amorphized at the GBs. Moreover, under compression, dislocation nucleation is identified in the water ice grains of the polycrystals, but does not observed in the hydrate grains. These findings are consistent with the results of previous theoretical and experimental studies [38,64-66].

Dynamics of Water Cages in Ice-Contained Hydrate Polycrystals

To provide an in-depth understanding of the structural evolutions within nanograin sI hydrate-ice polycrystals under mechanical loading, eight types of water cages and amorphous water molecules are

identified during deformation. The total number of water cages identified in sI hydrate polycrystals containing water ice under tensile and compressive strains are counted (See Supplementary Materials Figures S4-S23). Notably, besides the normal sI 5^{12} and $5^{12}6^2$ water polyhedral cages, many other water cages are also identified, *e.g.*, the $5^{12}6^3$, $5^{12}6^4$, $4^15^{10}6^2$, $4^15^{10}6^3$, $4^15^{10}6^4$ and $4^35^66^3$ cages. In terms of the number of cages prior to deformation, from greatest to least, the cages are $5^{12}6^2$, 5^{12}, $4^15^{10}6^2$, $5^{12}6^3$, $4^15^{10}6^3$, $4^15^{10}6^4$, $5^{12}6^4$, and $4^35^66^3$ for polycrystals with a given ice content (See Supplementary Materials Figures S4-S23). The number of cages is strongly dependent on the methane hydrate content in the polycrystal; a higher content of methane hydrate grains it has, a larger number of those cages it shows. These results indicate that various water cages are able to form at the GBs and GBJs, resulting in the cohesive GB structures of polycrystals. Under tension (See Supplementary Materials Figures S4-S13), for polycrystals with low ice contents (See Supplementary Materials Figures S4-S7), the number of 5^{12} and $5^{12}6^2$ cages initially decreases much violently. With the increasing ice content (See Supplementary Materials Figures S8-S10), the number of cages initially decreases slightly, which differs from that of the polycrystals with low ice contents discussed above. This suggests that the water cages, *e.g.*, 5^{12} and $5^{12}6^2$, dissociate at the HHGBs, HIGBs, and GBJs. However, for polycrystals with high ice contents (See Supplementary Materials Figures S11-S13), the number of identified sI polyhedral 5^{12} and $5^{12}6^2$ cages slightly declines prior to yielding. As the tensile strain reaches its critical value, the number of those cages increases with increasing tensile strain. Concerning the $5^{12}6^3$, $5^{12}6^4$, $4^15^{10}6^2$, $4^15^{10}6^3$, $4^15^{10}6^4$ and $4^35^66^3$ cages, complex changes in the average number of cages can be observed, depending on the type of cage and the ice content. For example, for the polycrystals containing 90% water ice (See

Supplementary Materials Figures S13), the number of $5^{12}6^3$ cage increases during the entire loading process, while a negligible change in the number of $5^{12}6^4$ cage and a decrease in the number of $4^15^{10}6^4$ cage are observed (See Supplementary Materials Figures S13c, S13d and S13g). Moreover, the average number of $4^15^{10}6^2$ and $4^15^{10}6^3$ cages in the polycrystals initially increase, but after this, they decrease (See Supplementary Materials Figures S13e and S13f). Interestingly, the polycrystals show initially decrease, and then, the average number of $4^35^66^3$ cage increases (See Supplementary Materials Figure S13h). These complex changes in the water cages indicate the complex recrystallization and amorphization dynamics of the molecular water cages in the polycrystals under tension. With increasing methane hydrate grains in the polycrystals (See Supplementary Materials Figures S4-S13), a more significant reduction in the number of cages ($5^{12}6^3$, $5^{12}6^4$, $4^15^{10}6^2$, $4^15^{10}6^3$, $4^15^{10}6^4$ and $4^35^66^3$ cages) is recognized in the early deformation stage of polycrystals with a higher number of methane hydrate grains (See Supplementary Materials Figures S4-S9). In the late-stage of deformation, the reduction in the number of cages is not significant, and an increase in the number of some of the water cages (*e.g.*, $5^{12}6^3$, $5^{12}6^4$, and $4^15^{10}6^2$ cages) is detected in polycrystals with specific hydrate contents (See Supplementary Materials Figures S4-S6). Intriguingly, unlike the changes in the number of water cages, the polycrystals with high ice contents (See Supplementary Materials Figures S8-S13) mainly present a monotonic increase in the number of amorphous water molecules, indicating the global dissociation of water-dominant polycrystals. Additionally, the number of amorphous water molecules in polycrystals with different ice contents significantly increases in the early stretching stage (See Supplementary Materials Figures S4-S13), whereas in the late stage of deformation, the increase in the number of

amorphous water molecules is less significant (See Supplementary Materials Figures S8-S13), and a slight decrease in the number of amorphous water molecules can even occur (See Supplementary Materials Figures S4-S7).

For the case of polycrystals subjected to compressive straining, the number of water cages and amorphous water molecules also changes as the strain changes. As shown in Supplementary Materials Figures S14-S23, hydrate polycrystals with ice contents of 20%-90% (See Supplementary Materials Figures S16-S23) exhibit a monotonic reduction in the number of 5^{12} and $5^{12}6^2$ water cages during the whole deformation process, which differs from hydrate polycrystals under tension. This reduction becomes more significant as the ice content decreases. For hydrate polycrystals containing low ice content (<10%) (See Supplementary Materials Figures S14-S15), the number of 5^{12} and $5^{12}6^2$ water cages initially increases, but then, it decreases during deformation. This indicates that low pressurization (smaller compressive strains) enhances the formation of 5^{12} and $5^{12}6^2$ cages at the GBs and GBJs of the polycrystals; whereas, in contrast to that depressurization (tension) causes the dissociation of these cages. However, large pressurization (larger compressive strains) results in the dissociation of 5^{12} and $5^{12}6^2$ cages (See Supplementary Materials Figures S14-S15). With regard to the large $5^{12}6^3$, $5^{12}6^4$, $4^15^{10}6^2$, $4^15^{10}6^3$, $4^15^{10}6^4$, and $4^35^66^3$ cages, a different change in their numbers occurs. Hydrate polycrystals containing different ice contents exhibit a transition in their number of these cages; the number of cages initially declines, and then, it increases under the compressive straining. As the ice content becomes less and less, the transition behavior becomes more significant. This indicates new water cage formation

during collective GB sliding in the post deformation stage. For amorphous water molecules, an almost linear increase in the number of water molecules is identified for all polycrystals. This increase in the number of amorphous water molecules suggests the global dissociation of ice-embedded hydrate polycrystals during mechanical straining, although localized recrystallization of water cages occurs. Based on the analysis of water cages and amorphous water molecules during deformation, complicated structural transformation of nanograin ice-contained hydrate polycrystals can occur under mechanical deformation. Such findings provide the detailed molecular information for deformation mechanism.

Conclusion

The mechanical instability of gas hydrates can trigger global climate change and geohazards in both terrestrial and extraterrestrial environments. At cold regions, *e.g.,* the permafrost regions on Earth and the cryospheres of large icy bodies throughout the Universe, natural gas hydrates often coexist with water ice. In this work, we conclude that hydrate-ice and hydrate-hydrate bicrystals show comparable tensile and compressive strengths. However, in particular, the average mechanical shear strengths of hydrate-hydrate bicrystals are twice as large as those of hydrate-ice bicrystals. Upon tension, both hydrate-ice and hydrate-hydrate bicrystals exhibit brittle failure, initiating from the grain boundaries. Upon compression, two apparent peaks occur on the stress-strain curves prior to the steady compression flow stresses of the hydrate-ice bicrystals; whereas only one peak occurs for the hydrate-hydrate bicrystals. Subjected to shearing, all of the bicrystals exhibit a sawtooth-like mechanical stress response due to grain boundary sliding and the subsequent healing of the interface structures. For ice-contained

methane hydrate polycrystals, both the ultimate tensile strength and the average compressive flow stress strongly depend on the ice content. For ice contents of 0% and 70%, the polycrystals are mechanically weakened; whereas for ice contents of 70% to 100%, they are strengthened. The later result is consistent with previous experimental measurements of polycrystals with ice contents of 70%-100%. Combining with the calculated results of bicrystals, we demonstrate that the mechanical strengths of ice-contained polycrystals are mainly dominated by the proportions of HHGBs, HIGBs, and IIGBs, resulting from that the mechanical strengths of the HHGBs and IIGBs are much higher than those of the HIGBs. This may raise an interesting question: Can the pure clathrate hydrate or hydrate with ice layer support the top ice shell on Pluto? If not, how much ice should occur in the hydrate layer at most or at least? Our future work will try to investigate it by micro- and macro-mechanical calculations. Furthermore, quantitative analysis of the microstructures of the water cages in the polycrystals indicates the dissociation and reformation of various water cages including normal (*e.g.*, 5^{12} and $5^{12}6^2$) and abnormally large (*e.g.*, $4^15^{10}6^2$, $5^{12}6^3$, $4^15^{10}6^3$, $4^15^{10}6^4$, $5^{12}6^4$, and $4^35^66^3$) water cages during mechanical tensile and compressive loading. Plastic deformation in polycrystals is mainly governed by grain boundary sliding, grain rotation, and solid-state phase transformation in the ice and hydrate grains. This plastic deformation is also accompanied by the complex competitive dynamics of recrystallization and amorphization of the molecular hydrate water cages and ice structures. In contrast, upon compression, dislocation nucleation occurs in ice grains. Our findings improve our understanding of the mechanical instability of ice-contained methane hydrate systems on Earth, and the evolution of the planetary mechanical stability of methane hydrates embedded in the cryosphere of large icy bodies throughout the Universe.

Methods

Our molecular simulations were carried out based on the monatomic model derived from the Stillinger-Weber (SW) potential, which describes both water and methane molecules. Each water and methane molecule is represented as a single interaction site, respectively, in the monatomic model [67,68]. Such a coarse-grained mW water model is computationally efficient and can accurately describe the thermodynamic and mechanical properties of water, ice, and methane hydrate. Despite the coarse-grained mW water model eliminates the electrostatic interactions for the sake of computational efficiency, it can also accurately capture the mechanical properties of methane hydrate and ice, compared with other popular full atomistic water interaction models *e.g.,* SPC/E, TIP4P, TIP4P/2005 and TIP4P/ICE. The efficient performance of such mW water model has been verified in previous studies [29]. Mechanical loadings subjected to all of the bicrystals and polycrystals were performed by the deformation control technique. Such technique has been widely used to study the mechanical properties of nano-systems. All deformation procedures were performed at a strain rate of 1.0×10^8 s^{-1}. More simulation details are provided in Supplementary Materials Sections S1-S5 (Section S1. System Preparations, Section S2. Forcefield for System Simulations, Section S3. Mechanical Test Simulations, Section S4. Mechanical Parameters, Section S5. Quantitative Analysis of Water Cages, Section S6. Crystal Face Binding Energy, Section S7. Centro-Symmetry Parameter, and Section S8. Average Percentages of Three Grain Boundary Types)

Acknowledgments

Funding: This work was financially supported by Qingdao National Laboratory for Marine Science and Technology Open Fund (QNLM2016ORP0203), the National Natural Science Foundation of China (Grant Nos. 41672367, 11772278, 11502221, and 51274177), the State Scholarship Fund of China Scholarship Council, the National Key Research and Development Program of China (2017YFC0307600), the Fundamental Research Funds for the Central Universities (Xiamen University: Grant Nos. 20720180014, 20720180018, and 20720160088), Fujian Provincial Department of Science & Technology (2017J05028), the Scientific Research Foundation for the Returned Overseas Chinese Scholars from State Education Ministry, "111" Project (B16029) and the 1000 Talents Program from Xiamen University. We thank Y. Yu and Z. Xu from Information & Network Center for Computational Science of Xiamen University for the help with the high-performance of supercomputers. And the High Performance Computing Center of China University of Geosciences (Wuhan) are also acknowledged. **Author contributions:** J. W. and F. N. conceived the research study. P. C. performed the molecular dynamics simulations. B. C., T. L., and P. C. analyzed the water cage data. P. C. draw all the pictures and wrote the original manuscript with input from all authors. J. W., F. N., and T. L. polished the manuscript (review and editing). All authors discussed the results and commented on the manuscript. **Competing interests:** The authors declare that they have no competing interests. **Data and materials availability:** All data needed to evaluate the conclusions in the paper are present in the paper and/or the Supplementary Materials. Additional data related to this paper may be requested from the authors.

References

(1) Sloan, E. D. Fundamental Principles and Applications of Natural Gas Hydrates. *Nature* **2003**, *426*, 353-363.

(2) McMullan, R. K.; Jeffrey, G. A. Polyhedral clathrate hydrates. IX. Structure of ethylene oxide hydrate. *J. Chem. Phys.* **1965**, *42*, 2725.

(3) Ripmeester, J. A.; Ratcliffe, C. I. Xenon-129 NMR studies of clathrate hydrates: new guests for structure II and structure H. *J. Phys. Chem.* **1990**, *94*, 8773-8776.

(4) Koh, C. A. Towards a fundamental understanding of natural gas hydrates. *Chem. Soc. Rev.* **2002**, *31*, 157-167.

(5) Sloan, E. D. Gas Hydrates: Review of Physical/Chemical Properties. *Energy Fuels* **1998**, *12*, 191-196.

(6) Kirchner, M. T.; Boese, R.; Billups, W. E.; Norman, L. R. Gas Hydrate Single-Crystal Structure Analyses. *J. Am. Chem. Soc.* **2004**, *126*, 9407-9412.

(7) Udachin, K. A.; Ratcliffe, C. I.; Ripmeester, J. A. A Dense and Efficient Clathrate Hydrate Structure with Unusual Cages. *Angew. Chem. Int. Ed.* **2001**, *40*, 1303-1305.

(8) Vatamanu, J.; Kusalik, P. G. Unusual Crystalline and Polycrystalline Structures in Methane Hydrates. *J. Am. Chem. Soc.* **2006**, *128*, 15588-15589.

(9) Huang, Y.; Zhu, C.; Wang, L.; Cao, X.; Su, Y.; Jiang, X.; Meng, S.; Zhao, J.; Zeng, X. C. A new phase diagram of water under negative pressure: The rise of the lowest-density clathrate s-III. *Sci. Adv.* **2016**, *2*, e1501010.

(10) Liu, Y.; Huang, Y.; Zhu, C.; Li, H.; Zhao, J.; Wang, L.; Ojamäe, L.; Francisco, J. S.; Zeng, X. C. An ultralow-density porous ice with the largest internal cavity identified in the water phase diagram. *Proc. Natl. Acad. Sci.* **2019**, *116*, 12684-12691.

(11) Liu, Y.; Ojamäe, L. Clathrate ice sL: a new crystalline phase of ice with ultralow density predicted by first-principles phase diagram computations. *PCCP* **2018**, *20*, 8333-8340.

(12) Holbrook, W. S.; Hoskins, H.; Wood, W. T.; Stephen, R. A.; Lizarralde, D. Methane Hydrate and Free Gas on the Blake Ridge from Vertical Seismic Profiling. *Science* **1996**, *273*, 1840.

(13) Collett, T. S.; Lee, M. W. Reservoir Characterization of Marine and Permafrost Associated Gas Hydrate Accumulations with Downhole Well Logs. *Ann. N. Y. Acad. Sci.* **2000**, *912*, 51-64.

(14) Kvenvolden, K. A. A review of the geochemistry of methane in natural gas hydrate. *Org. Geochem.* **1995**, *23* 997-1008.

(15) Stackelberg, M. v.; Müller, H. R. On the Structure of Gas Hydrates. *J. Chem. Phys.* **1951**, *19*, 1319.

(16) Kvenvolden, K. A. Methane hydrate - A major reservoir of carbon in the shallow geosphere? *Chem. Geol.* **1988**, *71*, 41-51.

(17) Collett, T. S. Energy resource potential of natural gas hydrates. *AAPG Bulletin* **2002**, *86*, 1971-1992.

(18) Glasby, G. P. Potential impact on climate of the exploitation of methane hydrate deposits offshore. *Mar. Pet. Geol.* **2003**, *20*, 163-175.

(19) Lelieveld, J.; Crutzen, P. J. Indirect chemical effects of methane on climate warming. *Nature* **1992**, *355*, 339-342.

(20) Dickens, G. R. Rethinking the global carbon cycle with a large, dynamic and microbially mediated gas hydrate capacitor. *Earth. Planet. Sci. Lett.* **2003**, *213*, 169-183.

(21) Brown, H. E.; Holbrook, W. S.; Hornbach, M. J.; Nealon, J. Slide structure and role of gas hydrate at the northern boundary of the Storegga Slide, offshore Norway. *Mar Geol.* **2006**, *229*, 179-186.

(22) MacDonald, I. R.; Guinasso , N. L.; Sassen, R.; Brooks, J. M.; Lee, L.; Scott, K. T. Gas hydrate that breaches the sea floor on the continental slope of the Gulf of Mexico. *Geology* **1994**, *22*, 699-702.

(23) Xu, W.; Germanovich, L. N. Excess pore pressure resulting from methane hydrate dissociation in marine sediments: A theoretical approach. *J. Geophys. Res.-Solid Earth* **2006**, *111*, B01104.

(24) Ning, F.; Yu, Y.; Kjelstrup, S.; Vlugt, T. J. H.; Glavatskiy, K. Mechanical properties of clathrate hydrates: status and perspectives. *Energy Environ. Sci.* **2012**, *5*, 6779-6795.

(25) Durham, W. B.; Kirby, S. H.; Stern, L. A.; Zhang, W. The strength and rheology of methane clathrate hydrate. *J. Geophys. Res.-Solid Earth* **2003**, *108*, B4.

(26) Durham, W. B.; Stern, L. A.; Kirby, S. H. Ductile flow of methane hydrate. *Can. J. Phys.* **2003**, *81*, 373-380.

(27) Stern, L. A.; Kirby, S. H.; Durham, W. B. Peculiarities of methane clathrate hydrate formation and solid-state deformation, including possible superheating of water Ice. *Science* **1996**, *273*, 1843-1848.

(28) Stern, L. A.; Kirby, S. H.; Durham, W. B. Polycrystalline Methane Hydrate: Synthesis from Superheated Ice, and Low-Temperature Mechanical Properties. *Energy Fuels* **1998**, *12*, 201-211.

(29) Wu, J.; Ning, F.; Trinh, T. T.; Kjelstrup, S.; Vlugt, T. J. H.; He, J.; Skallerud, B. H.; Zhang, Z. Mechanical instability of monocrystalline and polycrystalline methane hydrates. *Nat. Commun.* **2015**, *6*, 8743.

(30) Helgerud, M. B.; Waite, W. F.; Kirby, S. H.; Nur, A. Elastic wave speeds and moduli in polycrystalline ice Ih, sI methane hydrate, and sII methane-ethane hydrate. *J. Geophys. Res.-Solid Earth* **2009**, *114*, B02212.

(31) Jia, J.; Liang, Y.; Tsuji, T.; Murata, S.; Matsuoka, T. Microscopic Origin of Strain Hardening in Methane Hydrate. *Sci. Rep.* **2016**, *6*, 23548.

(32) Cole, D. M. Strain-rate and grain-size effects in ice. *J. Glaciol.* **1987**, *33*, 274-280.

(33) Currier, J.; Schulson, E. The tensile strength of ice as a function of grain size. *Acta Metall.* **1982**, *30*, 1511-1514.

(34) Schiotz, J.; Di Tolla, F. D.; Jacobsen, K. W. Softening of nanocrystalline metals at very small grain sizes. *Nature* **1998**, *391*, 561-563.

(35) Wu, J.; Cao, P.; Zhang, Z.; Ning, F.; Zheng, S.-s.; He, J.; Zhang, Z. Grain-Size-Controlled Mechanical Properties of Polycrystalline Monolayer MoS2. *Nano Lett.* **2018**, *18*, 1543-1552.

(36) Durham, W. B.; Stern, L. A. Rheological properties of water ice-applications to satellites of the outer planets. *Ann. Rev. Earth Planet. Sci.* **2001**, *29*, 295-330.

(37) Cao, P.; Wu, J.; Zhang, Z.; Fang, B.; Ning, F. Mechanical Properties of Methane Hydrate: Intrinsic Differences from Ice. *J. Phys. Chem. C* **2018**, *122*, 29081-29093.

(38) Cao, P.; Wu, J.; Zhang, Z.; Fang, B.; Peng, L.; Li, T.; Vlugt, T. J. H.; Ning, F. Mechanical properties of bi- and poly-crystalline ice. *AIP Advances* **2018**, *8*, 125108.

(39) Miller, S. L. Clathrate Hydrates of Air in Antarctic Ice. *Science* **1969**, *165*, 489.

(40) Ikeda, T.; Fukazawa, H.; Mae, S.; Pepin, L.; Duval, P.; Champagnon, B.; Lipenkov, V. Y.; Hondoh, T. Extreme fractionation of gases caused by formation of clathrate hydrates in Vostok Antarctic Ice. *Geophys. Res. Lett.* **1999**, *26*, 91-94.

(41) Takeya, S.; Nagaya, H.; Matsuyama, T.; Hondoh, T.; Lipenkov, V. Y. Lattice Constants and Thermal Expansion Coefficient of Air Clathrate Hydrate in Deep Ice Cores from Vostok, Antarctica. *J. Phys. Chem. B* **2000**, *104*, 668-670.

(42) Uchida, T.; Hondoh, T.; Mae, S.; Lipenkov, V. Y.; Duval, P. Air-hydrate crystals in deep ice-core samples from Vostok Station, Antarctica. *J. Glaciol.* **1994**, *40*, 79-86.

(43) Price, P. B. Kinetics of Conversion of Air Bubbles to Air Hydrate Crystals in Antarctic Ice. *Science* **1995**, *267*, 1802.

(44) Shoji, H.; Langway, C. C. Air hydrate inclusions in fresh ice core. *Nature* **1982**, *298*, 548-550.

(45) Guillot, T. The Interiors of Giant Planets: Models and Outstanding Questions. *Ann. Rev. Earth Planet. Sci.* **2005**, *33*, 493-530.

(46) Lunine, J. I.; Stevenson, D. J. Clathrate and ammonia hydrates at high pressure: Application to the origin of methane on Titan. *Icarus* **1987**, *70*, 61-77.

(47) Fortes, A. D. Titan's internal structure and the evolutionary consequences. *Planet. Space Sci.* **2012**, *60*, 10-17.

(48) Kamata, S.; Nimmo, F.; Sekine, Y.; Kuramoto, K.; Noguchi, N.; Kimura, J.; Tani, A. Pluto's ocean is capped and insulated by gas hydrates. *Nat. Geosci.* **2019**, *12*, 407-410.

(49) Li, Y.; Song, Y.; Liu, W.; Yu, F. Experimental Research on the Mechanical Properties of Methane Hydrate-Ice Mixtures. *Energies* **2012**, *5*, 181-192.

(50) Li, Y.; Zhao, H.; Yu, F.; Song, Y.; Liu, W.; Li, Q.; Yao, H. Investigation of the Stress–Strain and Strength Behaviors of Ice Containing Methane Hydrate. *J. Cold Regions. Eng* **2012**, *26*, 149-159.

(51) Li, Y.; Liu, W.; Song, Y.; Yang, M.; Zhao, J. Creep behaviors of methane hydrate coexisting with ice. *J. Nat. Gas. Sci. Eng.* **2016**, *33*, 347-354.

(52) Mochizuki, K.; Matsumoto, M.; Ohmine, I. Defect pair separation as the controlling step in homogeneous ice melting. *Nature* **2013**, *498*, 350-354.

(53) Donadio, D.; Raiteri, P.; Parrinello, M. Topological Defects and Bulk Melting of Hexagonal Ice. *J. Phys. Chem. B* **2005**, *109*, 5421-5424.

(54) Grishina, N.; Buch, V. Structure and dynamics of orientational defects in ice I. *J. Chem. Phys.* **2004**, *120*, 5217-5225.

(55) Pirzadeh, P.; Kusalik, P. G. Molecular Insights into Clathrate Hydrate Nucleation at an Ice–Solution Interface. *J. Am. Chem. Soc.* **2013**, *135*, 7278-7287.

(56) Nguyen, A. H.; Koc, M. A.; Shepherd, T. D.; Molinero, V. Structure of the Ice–Clathrate Interface. *J. Phys. Chem. C* **2015**, *119*, 4104-4117.

(57) Shimizu, H.; Kumazaki, T.; Kume, T.; Sasaki, S. Elasticity of single-crystal methane hydrate at high pressure. *Phys. Rev. B* **2002**, *65*, 212102.

(58) Gagnon, R. E.; Kiefte, H.; Clouter, M. J.; Whalley, E. Elastic constants of ice Ih, up to 2.8 kbar, by Brillouin spectroscopy. *J. Phys. Colloques* **1987**, *48*, C1-23-C21-28.

(59) Kuhs Werner, F.; Klapproth, A.; Gotthardt, F.; Techmer, K.; Heinrichs, T. The formation of meso - and macroporous gas hydrates. *Geophys. Res. Lett.* **2000**, *27*, 2929-2932.

(60) Falenty, A.; Salamatin, A. N.; Kuhs, W. F. Kinetics of CO_2-Hydrate Formation from Ice Powders: Data Summary and Modeling Extended to Low Temperatures. *J. Phys. Chem. C* **2013**, *117*, 8443-8457.

(61) Cole, D. M. Grain Size and the Compressive Strength of Ice. *Journal of Energy Resources Technology* **1985**, *107*, 369-374.

(62) Kvamme, B.; Selvåg, J.; Saeidi, N.; Kuznetsova, T. Methanol as a hydrate inhibitor and hydrate activator. *PCCP* **2018**, *20*, 21968-21987.

(63) Kvamme, B.; Kuznetsova, T.; Kivelæ, P.-H. Adsorption of water and carbon dioxide on hematite and consequences for possible hydrate formation. *PCCP* **2012**, *14*, 4410-4424.

(64) Liu, F.; Baker, I.; Dudley, M. Dislocation-grain boundary interactions in ice crystals. *Philos. Mag. A* **1995**, *71*, 15-42.

(65) Webb, W. W.; Hayes, C. E. Dislocations and plastic deformation of ice. *Philos. Mag.* **1967**, *16*, 909-925.

(66) Hayes, C.; Webb, W. Dislocations in ice. *Science* **1965**, *147*, 44-45.

(67) Molinero, V.; Moore, E. B. Water Modeled as an Intermediate Element between Carbon and Silicon. *J. Phys. Chem. B* **2009**, *113*, 4008-4016.

(68) Jacobson, L. C.; Molinero, V. A Methane-Water Model for Coarse-Grained Simulations of Solutions and Clathrate Hydrates. *J. Phys. Chem. B* **2010**, *114*, 7302-7311.

Figures and Tables

Figure 1:

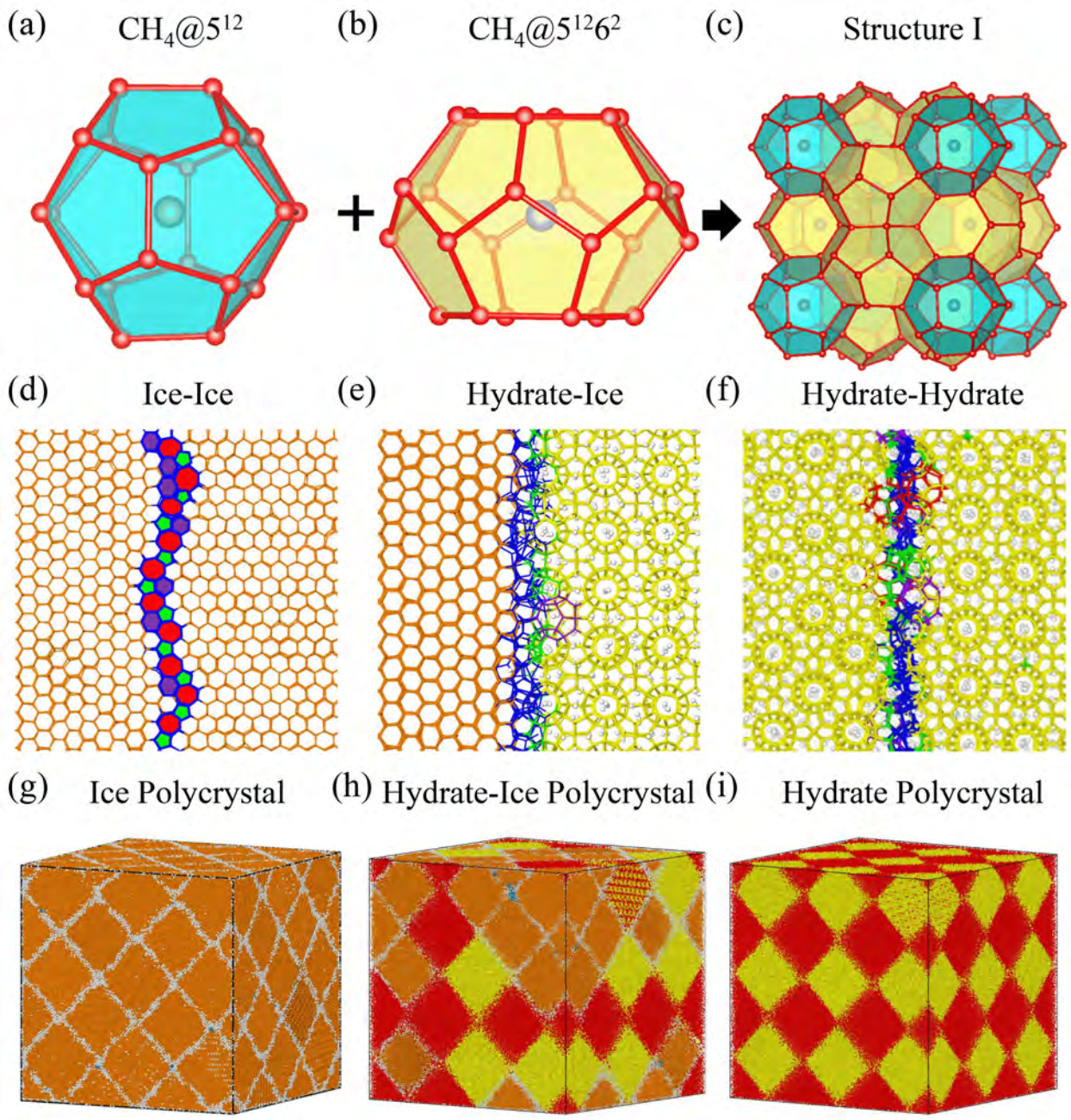

Figure 1. Molecular structures of methane hydrates. (a)-(c) Water molecular cages of $CH_4@5^{12}$

composed of 12 pentagonal faces, $CH_4@5^{12}6^2$ composed of 12 pentagonal and 2 hexagonal faces, and the sI crystal structure of methane hydrate, respectively. (d)-(f) Localized grain boundary structures of ice-ice (II), hydrate-ice (HI), and hydrate-hydrate (HH) bicrystals, respectively. (In Figure 1d, green: five-membered ring, purple: six-membered ring, and red: seven-membered ring. In Figure 1e and 1f, 5^{12}, $5^{12}6^2$, $5^{12}6^3$, $5^{12}6^4$, unidentified water and methane molecular structures are highlighted by green, yellow, purple, red, blue and white, respectively. In Figure 1d and 1e, the hexagonal ice and unidentified water structures are rendered by orange and blue for clarification, respectively) (g)-(i) 3-dimensional (3D) polycrystals of ice-contained methane hydrates with an average grain size of around 6.58 nm with ice content of 100%, 50%, and 0%, respectively. Ice is colored according to the identified type of structural phase; the hexagonal, cubic and unidentified water structures are rendered by orange, light blue and white for clarification, respectively. The methane hydrates are rendered by either red or yellow for clarification.

Figure 2:

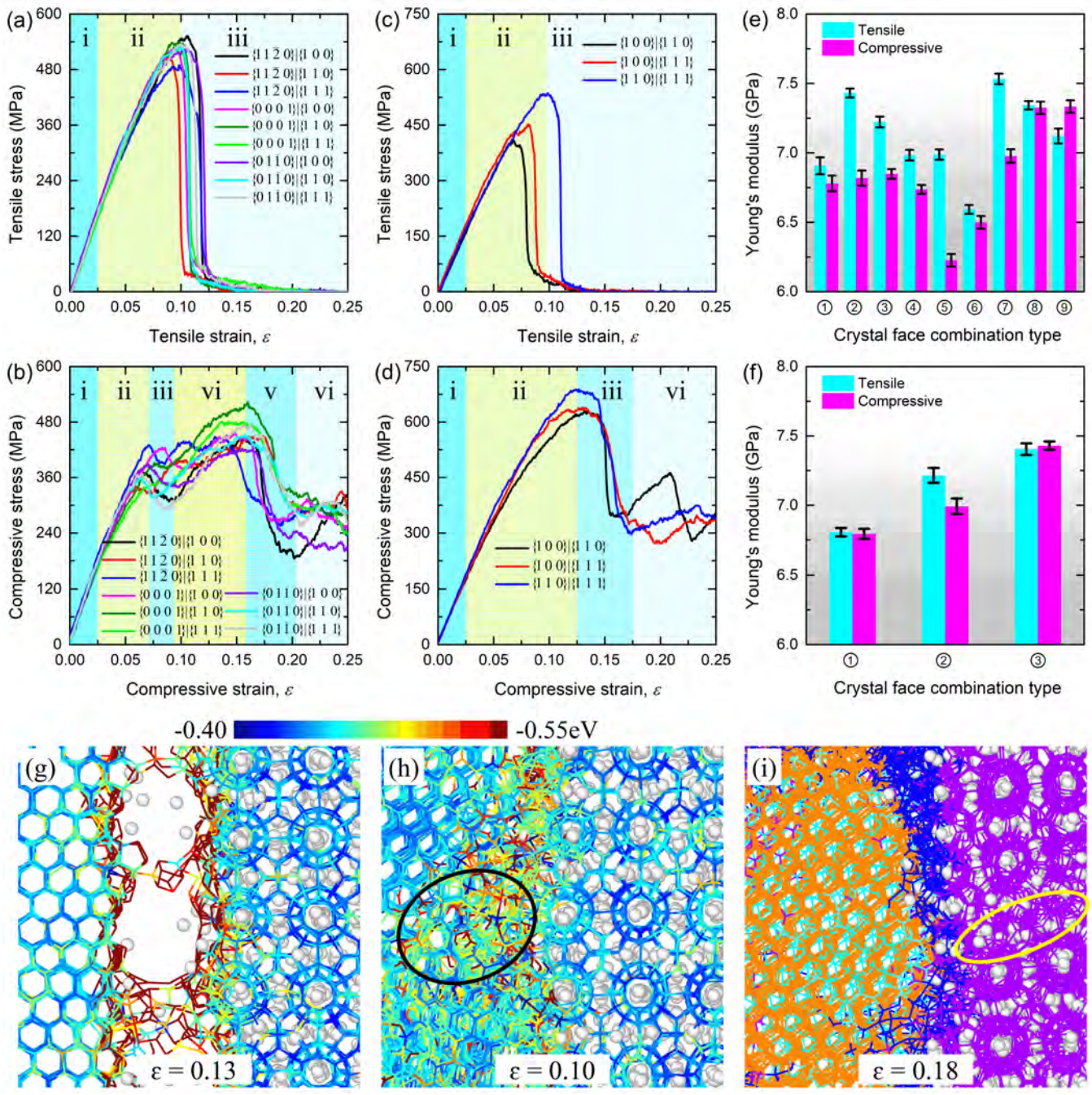

Figure 2. Mechanical response of bicrystals. (a)-(b) Mechanical tensile and compressive response of hydrate-ice (HI) bicrystals under tension and compression, respectively. (c)-(d) Mechanical tensile and compressive response of hydrate-hydrate (HH) bicrystals under tension and compression, respectively.

(e) Histograms of the Young's modulus of HI bicrystals. ①-⑨ represent $\{11\bar{2}0\}|\{1\,0\,0\}$, $\{11\bar{2}0\}|\{1\,1\,0\}$, $\{11\bar{2}0\}|\{1\,1\,1\}$, $\{0\,0\,0\,1\}|\{1\,0\,0\}$, $\{0\,0\,0\,1\}|\{1\,1\,0\}$, $\{0\,0\,0\,1\}|\{1\,1\,1\}$, $\{01\bar{1}0\}|\{1\,0\,0\}$, $\{01\bar{1}0\}|\{1\,1\,0\}$, and $\{01\bar{1}0\}|\{1\,1\,1\}$, respectively, in Figure 2c. $\{11\bar{2}0\}$, $\{0\,0\,0\,1\}$, and $\{01\bar{1}0\}$ planes are three common crystallographic planes of hexagonal ice. The $\{1\,0\,0\}$, $\{1\,1\,0\}$, and $\{1\,1\,1\}$ planes of the sI hydrates are considered in this study (f) Histograms of the Young's modulus of HH bicrystals. ①-③ represent $\{1\,0\,0\}|\{1\,1\,0\}$, $\{1\,0\,0\}|\{1\,1\,1\}$, and $\{1\,1\,0\}|\{1\,1\,1\}$, respectively, in Figure 2f. The $\{1\,0\,0\}$, $\{1\,1\,0\}$, and $\{1\,1\,1\}$ planes of sI hydrate are considered in this study. (g) Localized snapshots of HI bicrystals with $\{01\bar{1}0\}|\{1\,0\,0\}$ grain boundary structures at a tensile strain of 0.13. (h) Localized snapshots of HI bicrystals with $\{01\bar{1}0\}|\{1\,0\,0\}$ grain boundary structures at a compressive strain of 0.10. The latticed ice fracturing areas are marked by a black ellipse in Figure 2h. (i) Localized snapshots of HI bicrystals with $\{01\bar{1}0\}|\{1\,0\,0\}$ grain boundary structures at a compressive strain of 0.18. The latticed hydrate fracturing areas are marked by a yellow ellipse in Figure 2i. The water particles in snapshots #(g)-(h) are rendered according to their potential energy. The water particles which form the hexagonal ice in snapshots #(i) are colored according to the identified type of structural phase; the hexagonal, cubic and unidentified water structures are rendered by orange, sky-blue and blue for clarification, respectively. The water particles which form the sI structure methane hydrates in snapshots #(i) are colored by purple. All methane particles in (g)-(i) are rendered by white for clarification.

Figure 3:

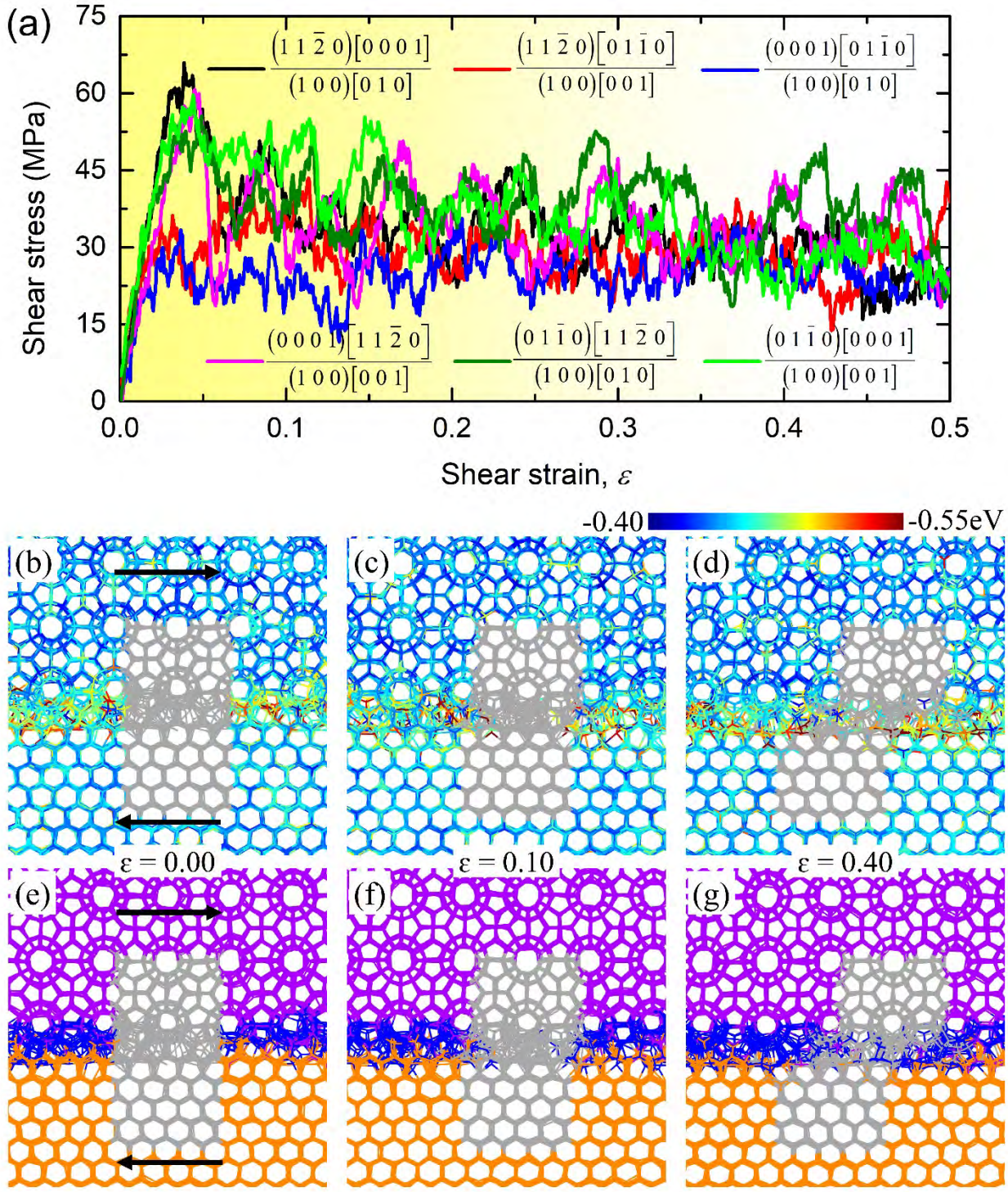

Figure 3. Mechanical shear response of hydrate-ice (HI) bicrystals. (a) Mechanical shear

stress-strain curves of HI bicrystals with different grain boundary structures under nonequivalent directional shear deformation, respectively. (b)-(g) Localized snapshots of HI bicrystals with $\{11\bar{2}0\}|\{1\,0\,0\}$ grain boundary structures subjected to $\frac{(1\,1\,\bar{2}\,0)[0\,1\,\bar{1}\,0]}{(1\,0\,0)[0\,0\,1]}$directional shear loadings at different strains, respectively. The black arrows indicate the shear loading directions. The water particles in (b)-(d) are rendered according to their potential energy. The water particles which form hexagonal ice in (e)-(g) are colored according to the identified type of structural phase; the hexagonal, cubic and unidentified water structures are rendered by orange, sky-blue and blue for clarification, respectively. The water particles which form sI structure methane hydrate in (e)-(g) are colored by purple. All methane particles are removed to clearly observe the grain boundary changes. The selected water particles are rendered by gray in (b)-(g) to monitor grain boundary sliding.

Figure 4:

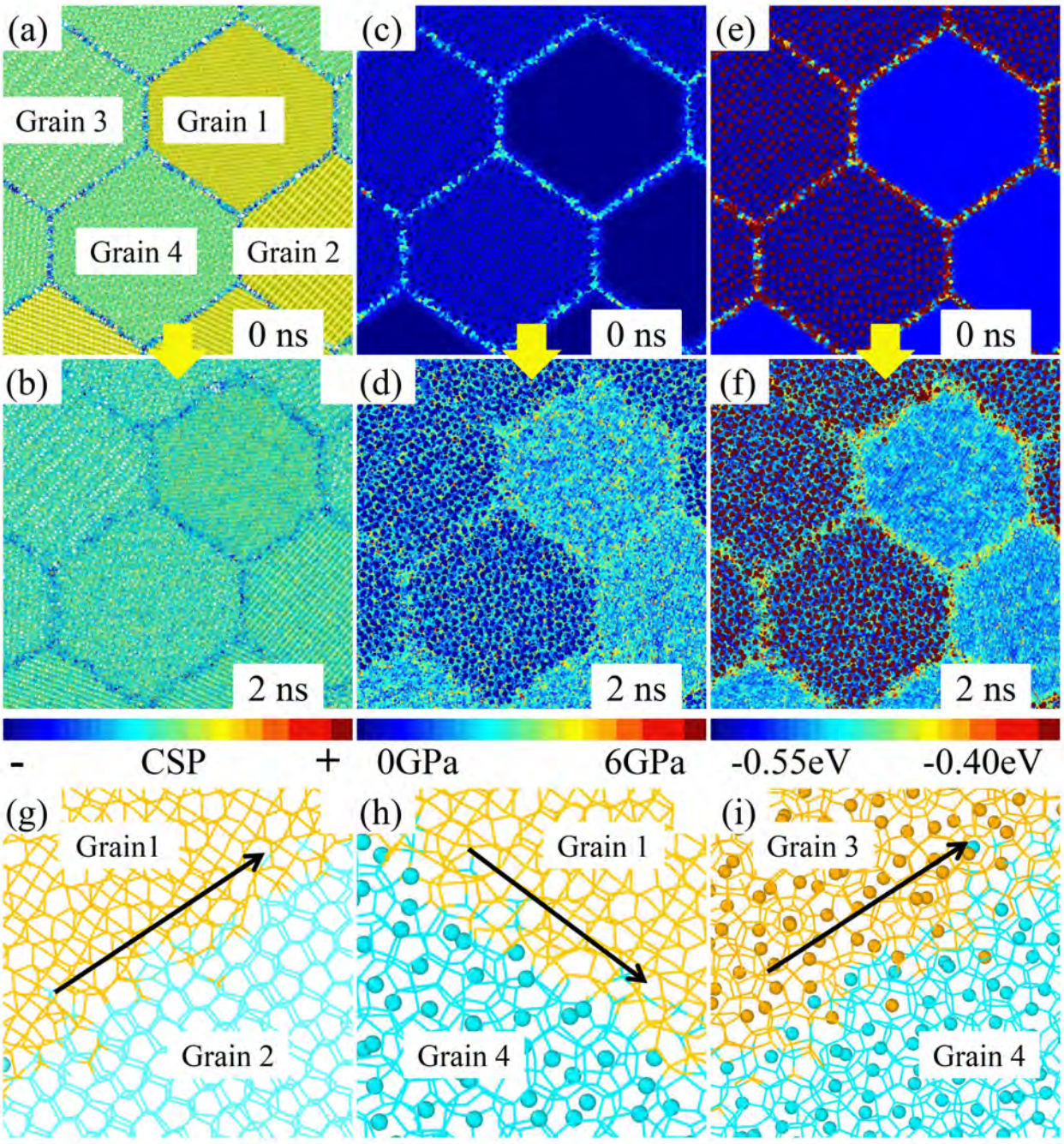

Figure 4. Typical localized molecule structures of hydrate-ice polycrystals with ice content of 50%.

(a)-(b) Cross-sectional snapshots of polycrystals before and after molecular dynamics (MD) relaxation,

respectively. All water particles are colored according to the centro-symmetry parameter (CSP) values. All methane particles are not shown to exhibit the different local lattice disorder clearly. (c)-(d) Cross-sectional snapshots of polycrystals before and after MD relaxation, respectively. All particles are colored according to the *von Mises* stress. (e)-(f) Cross-sectional snapshots of polycrystals before and after MD relaxation, respectively. All particles are colored according to the potential energy. (g)-(i) Cross-sectional snapshots of ice-ice, hydrate-ice, and hydrate-hydrate grain boundary structure in polycrystals, respectively. All particles are rendered according to the grain number.

Figure 5:

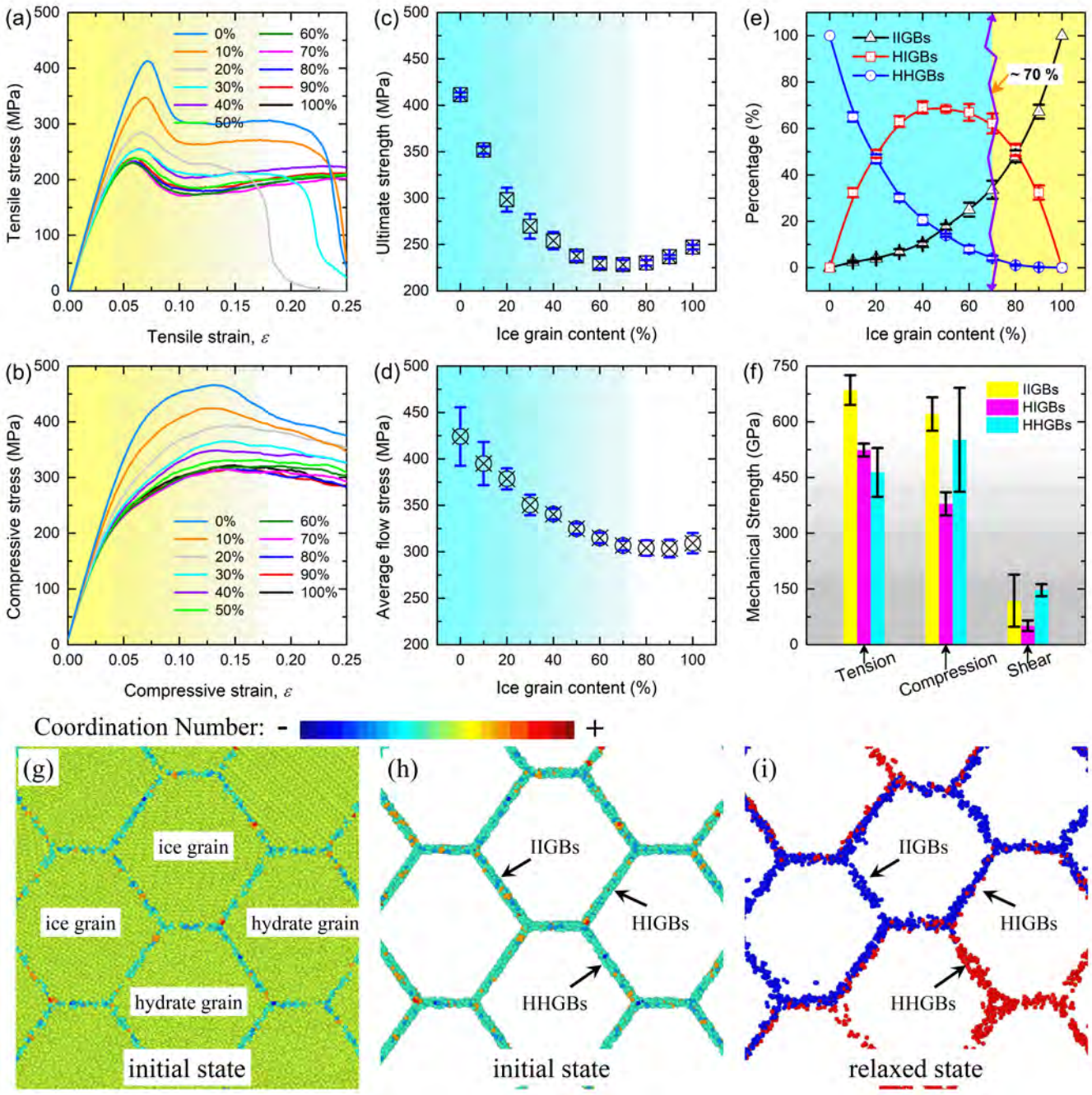

Figure 5. Mechanical properties of polycrystalline methane hydrate contained ice grains. (a)-(b) The stress-strain curves of polycrystals with different ice content under tension and compression, respectively. (c) Tensile maximum stress as a function of ice grain content. (d) Average compressive

flow stress as a function of ice grain content. (e) Percentages of three grain boundary types (IIGBs, HIGBs, and HHGBs) in polycrystals as a function of ice grain content. Firstly, all methane particles, water particles in both ice grain and hydrate grain interiors are removed as shown in Figure 6h and 6i. Secondly, the number of water particles located at IIGBs, HIGBs, and HHGBs can be roughly counted. Thirdly, the percentages of three grain boundary types can be roughly obtained through the number of water molecules located at three grain boundary types divided by the total number of water molecules at grain boundaries (See Supplementary Materials Note 3. Average Percentages of Three Grain Boundary Types). (f) Average mechanical strengths under different mechanical loads obtained from this simulations and a recent study [38] (See Supplementary Materials Sections S4. Mechanical Parameters). (g) Localized structures captured from the polycrystal with ice content of 50% at initial state. (h) Localized grain boundary structures captured from the polycrystal with ice content of 50% at initial state. Water atoms in polycrystals are colored according to the coordination number of water particles in Figure 5g and 5h. (i) Localized grain boundary structures captured from the polycrystal with ice content of 50% at relaxed state. Water particles in hydrate grains and ice grains are colored by red and blue, respectively, in Figure 5i. All methane particles in (g)-(i) are removed to clearly show grain boundaries.

Figure 6:

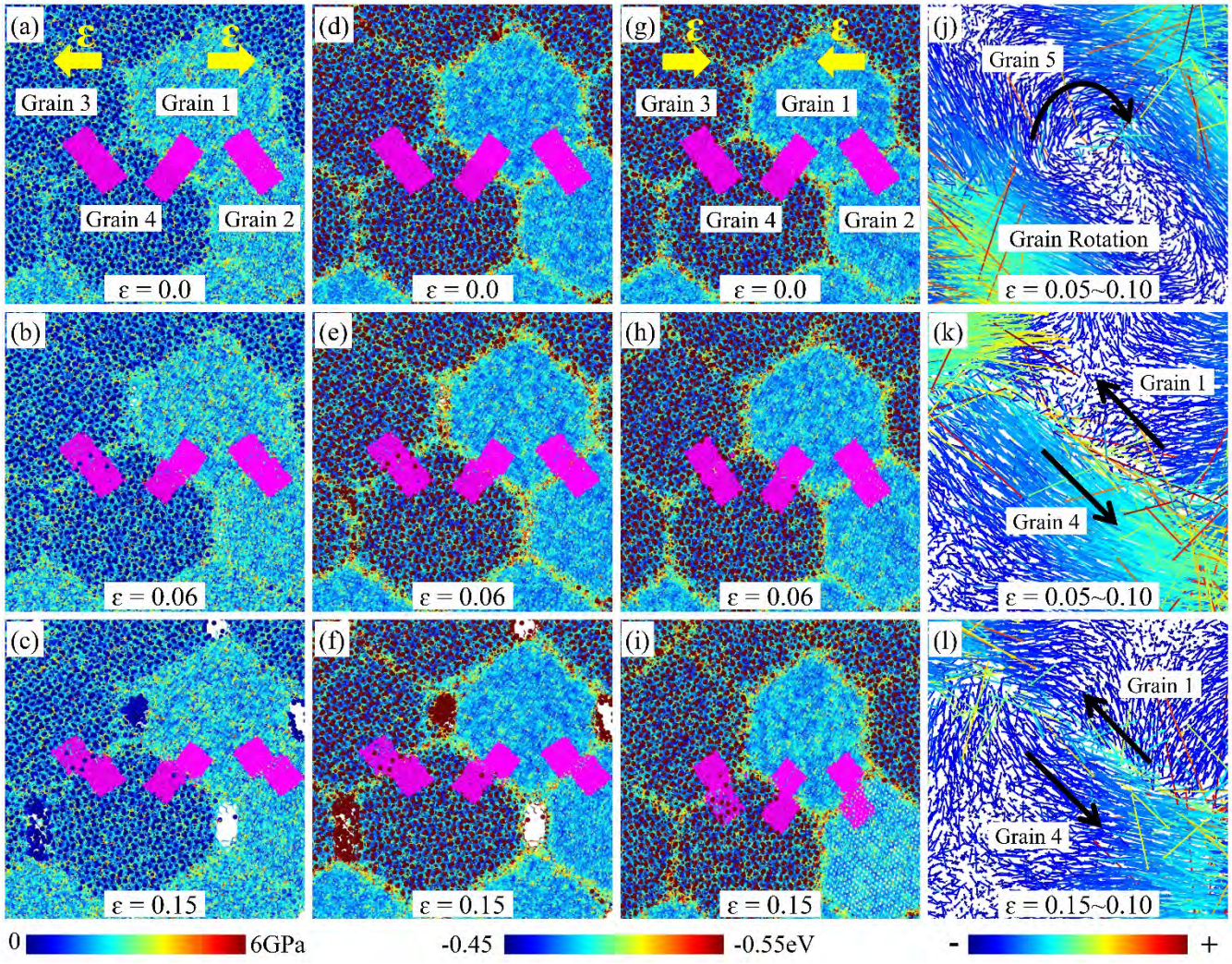

Figure 6. Cross-sectional snapshots of hydrate-ice polycrystals with ice content of 50% under uniaxial loadings. (a-c) Typically localized structures captured from the polycrystal at tensile strains of 0.00, 0.06 and 0.15, respectively. Atoms in polycrystals are colored according to the *von Mises* stress. (d-f) Typically localized structures captured from the polycrystal at tensile strains of 0.00, 0.06 and 0.15, respectively. Atoms in polycrystals are colored according to their potential energy. (g-i) Typically localized structures captured from the polycrystal at compressive strains of 0.00, 0.06 and 0.15,

respectively. Atoms in polycrystals are colored according to their potential energy. (j) Grain rotation of hydrate grain in the polycrystal under tension is captured. (k-l) grain boundary sliding in the polycrystal. Atoms in polycrystals are colored according to the values of displacement vectors in Figure 6j-6l. Grain 1-2 are ice grains and grain 3-5 are hydrate grains.

Table of Contents

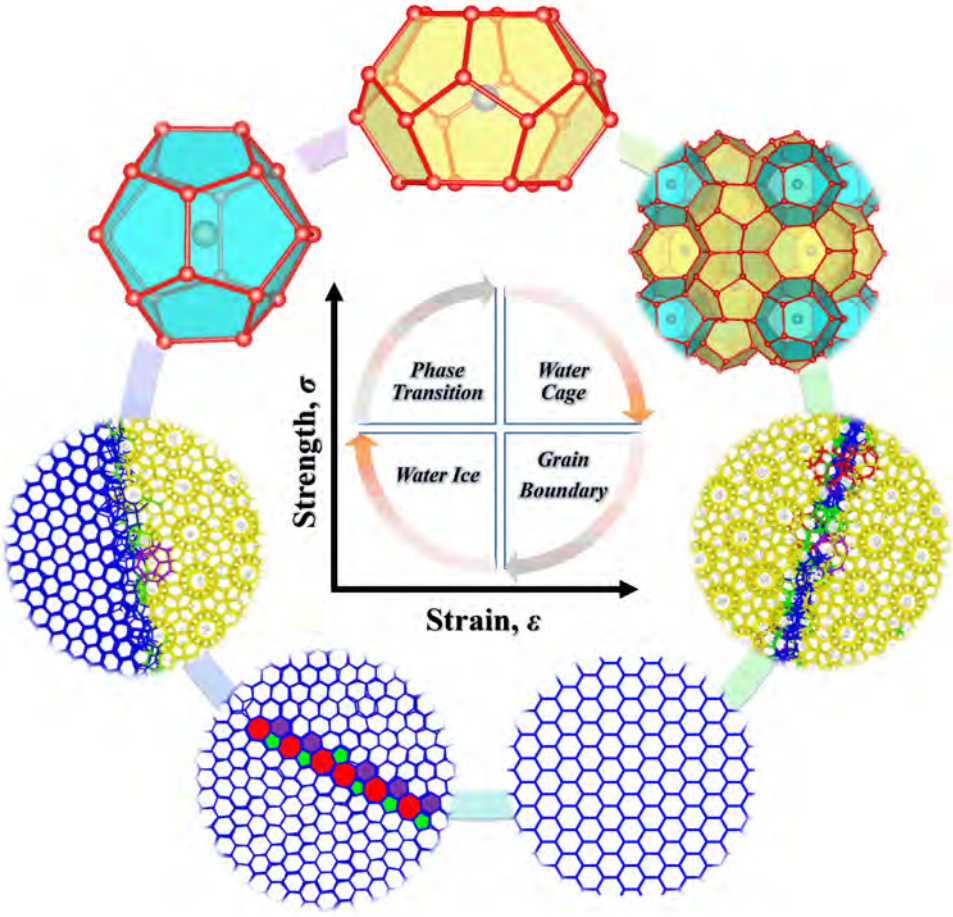

Supplementary Materials for

Mechanical Response of Nanocrytalline Ice-Contained Methane Hydrates: Key Role of Water Ice

Pinqiang Cao [1, 2, 3], Fulong Ning [1, 4, *], Jianyang Wu [3, 5, *], Boxiao Cao [2], Tianshu Li [2], Henrik Andersen Sveinsson [6], Zhichao Liu [1, 4], Thijs J.H. Vlugt [7], Masayuki Hyodo [8],

[1] Faculty of Engineering, China University of Geosciences, Wuhan, Hubei 430074, China.

[2] Department of Civil and Environmental Engineering, The George Washington University, Washington, DC 20052, U.S.A

[3] Department of Physics, Jiujiang Research Institute, Research Institute for Biomimetics and Soft Matter, Fujian Provincial Key Laboratory for Soft Functional Materials Research, Xiamen University, Xiamen 361005, China

[4] National Center for International Research on Deep Earth Drilling and Resource Development, Wuhan, Hubei 430074, China.

[*]Email: nflzx@cug.edu.cn; jianyang@xmu.edu.cn

[5] NTNU Nanomechanical Lab, Department of Structural Engineering, Norwegian University of Science and Technology (NTNU), Trondheim N-7491, Norway

[6] The Njord Center, Department of Physics, University of Oslo, Oslo, 0316, Norway

[7] Process & Energy Department, Delft University of Technology, Leeghwaterstraat 39, 2628CB Delft, The Netherlands

[8] Graduate School of Science and Technology for Innovation, Yamaguchi University, Yamaguchi City, Yamaguchi 753-8511, Japan

Email address:

Pinqiang@cug.edu.cn;

caoboxiao@gmail.com;

tsli@gwu.edu;

henrik.sveinsson@me.com;

liuzhichao121215@163.com;

T.J.H.Vlugt@tudelft.nl;

hyodo@yamaguchi-u.ac.jp;

*To whom correspondence should be addressed: nflzx@cug.edu.cn; jianyang@xmu.edu.cn;

This PDF file includes:

Supplementary Materials and Methods

Other Supplementary Material for this manuscript includes the following:

Movie. S1-S8 (.avi format). Animation of localized hydrate-ice bicrystals with different grain boundary structures under tension or compression strain.

Movie. S9-S16 (.avi format). Animation of localized hydrate-hydrate bicrystals with different grain boundary structures under tension or compression strain.

Movie. S17-S18 (.avi format). Animation of localized hydrate-ice bicrystals with $\{11\bar{2}0\}|\{1\,0\,0\}$ grain boundary structures under shear strain.

Movie. S19-S20 (.avi format). Animation of localized hydrate-hydrate bicrystals with $\{1\,0\,0\}|\{1\,1\,0\}$ grain boundary structures under shear strain.

Supplementary Materials and Methods

Section S1. System Preparations

This paper aims to present a systematic study of mechanical properties of hydrate-ice micro system by means of molecular dynamics (MD) simulations. Prime atomic structure of monocrystalline hexagonal ice was obtained by the X-ray diffraction experimental analysis data [1]. One unit cell of monocrystalline hexagonal ice is composed of 16 water molecules. The starting positions of water oxygen atoms of initial hydrate structure configuration were also taken from the X-ray diffraction analysis results for ethylene oxide hydrate [2]. One unit cell of structure I (sI) hydrate contains 46 water molecules. For hydrate-ice (HI) bicrystals, nine distinct bicrystals formed by two different adjacent monocrystals separated by a grain boundary (GB) were specifically constructed to study mechanical characteristics of HI bicrystals under tension, compression, and shear (See main manuscript Figure 1e). Each HI model contains around 19,242 ~ 23,544 water and methane molecules. For hydrate-hydrate (HH) bicrystals, three different bicrystals were also created to investigate mechanical properties with the same methods (See main manuscript Figure 1f). Each HH model has approximately 14,052 ~ 21,945 water and methane molecules. Polycrystalline hydrate-ice samples with ice content of 0%~100% were constructed with dimensions of $40 \times 40 \times 40$ nm^3 based on a Voronoi construction [3] (See main manuscript Figures1g-i). Both small 5^{12} and big $5^{12}6^2$ water cages were fully occupied by methane molecules. Each polycrystal contains around 54 grains. The grains in samples were taken to be random for crystalline orientations. The

81 average grain size in our study was about 6.58 nm. Four different polycrystals at each specific ice content
82 were constructed and calculated to facilitate further statistical analysis. Molecules which were in a
83 nearest-neighbour distance of less than 0.1 nm were deleted to form GBs and to avoid artificial atoms
84 overlaps in each polycrystal. Each polycrystal contains around 2,034,000 total water and methane
85 molecules. To obtain stable bicrystalline and polycrystalline structures, all created bicrystals and
86 polycrystals were equilibrated with relaxation time of 2,000 ps to eliminate low-or high-density regions
87 near GBs and GB junctions (GBJs). Firstly, all created bicrystals and polycrystals were all
88 quasi-statically relaxed to a local minimum energy configuration via the conjugate gradient method with
89 an energy tolerance of 1.0×10^{-4} eV and a force tolerance of 0.0 eV $Å^{-1}$. A simulation time of 1,000 ps
90 was chosen to relax all molecular structures at temperature of 223.15 K and pressure of 10 MPa under the
91 NPT ensemble (constant number of particles, constant pressure, and constant temperature) based on a
92 Nosé–Hoover barostat and Nosé–Hoover thermostat with damping times of τ_p = 1 ps and τ_T = 0.1 ps,
93 respectively. Subsequently, MD relaxation simulations were also performed with another simulation time
94 of 1,000 ps under the NVT ensemble (constant number of particles, constant volume, and constant
95 temperature) using the Nosé–Hoover thermostat with damping times of τ_T = 0.1 ps. The temperature and
96 pressure were controlled by Nosé-Hoover thermostat [4,5] and barostat methods [6], respectively. A constant
97 integration timestep of 1.0 fs with the velocity-Verlet algorithm was adopted. Periodic boundary
98 conditions were applied in 3-dimensional (3D) directions. Herein, stable specimens for mechanical tests
99 were prepared.

Section S2. Forcefield for System Simulations

All of our works were carried out based on the monatomic model that derives from the Stillinger-Weber (SW) potential [7] to describe both water and methane molecules in our models. Each water and methane molecule is represented as a single sphere, respectively, in the monatomic model. The coarse-grained mW water model omits hydrogen atoms or electrostatics. The water molecules can be able to form tetrahedral structures through three-body nonbonded interactions. This SW potential can model the tetrahedral short-ranged interaction potentials of monatomic water and those of water-water, water-methane and methane-methane interactions [8,9]. More importantly, such a coarse-grained mW water model could significantly reduce the computational cost compared to the full atomistic models [8], and it has been successfully verified to study mechanical properties of ice and methane hydrate systems [10].

Section S3. Mechanical Test Simulations

All calculations were performed using the Large-scale Atomic-Molecular Massively Parallel Simulator (LAMMPS) software package [11]. Periodic boundary conditions were applied along the three directions in our simulations. The mechanical loadings subjected to all bicrystals and polycrystals were simulated by the deformation control technique under the NPT ensemble. The procedure was performed at a strain rate of 1.0×10^8 s^{-1}. Both tensile and compressive loadings on bicrystals and polycrystals as well as shear loadings on bicrystals were simulated to investigate mechanical properties under the NPT ensembles. For shear loadings on bicrystals, simulated pressures in the directions that are perpendicular to

shear directions were carried out to be 10 MPa during shear loadings. This NPT ensemble with a Nosé–Hoover barostat and thermostat with damping time constant of τ_T = 1 ps and τ_p = 0.1 ps, respectively, allowed the bicrystals and polycrystals to experience expansion/contraction in the transverse directions as a result of the Poisson effect. A timestep of 1 fs with the velocity-Verlet algorithm was employed to integrate the equation of atomic motions. The deformation increment for bicrystals and polycrystals was updated every 1,000 time steps. The atomic stress per atom was calculated based on the *virial* definition of stress, using the forces on atoms collected during MD simulations. The atomic potential energy and atomic stress were averaged every 1,000 timesteps in order to eliminate the thermal oscillations.

Section S4. Mechanical Parameters

The Mechanical parameters used in this study are stated in this section. The engineering strain is defined as the ratio of total deformation length (ΔL) to the initial original length (L), tensile strain is defined as the ratio of total deformation length (ΔL) to the original length (L) under tension, and compressive strain is defined as the ratio of total deformation length (ΔL) to the original length (L) under compression.

$$\varepsilon = \frac{\Delta L}{L} = \frac{|l - L|}{L} \tag{1}$$

where ε is the engineering strain (*e.g.* tensile strain for tension and compressive strain for compression), L is the original length and l is the final length. Young's modulus defines the relationship between stress and strain in a material in the linear elasticity regime of a uniaxial deformation. Young's

modulus can be calculated by dividing the engineering stress by the engineering strain in the linear elastic regime of the loading curve as following,

$$E = \frac{\sigma}{\varepsilon} \quad (2)$$

where E is Young's modulus (GPa), σ is the uniaxial stress (GPa), ε is the engineering strain. In this work, the Young's modulus was determined by linearly fitting the stress-strain curves in the elastic strain regime. For the mechanical strengths in Figure 5f in our main manuscript, the Average mechanical strengths under different mechanical loads obtained from the work in our manuscript and a recent study [12]. For example, upon mechanical tensile strengths, they are the average values of the first peak strength obtained from the stress-strain curves of bicrystals with different GB structures.

Section S5. Quantitative Analysis of Water Cages

In this work, to identify water cages made of H_2O molecules in ice-contained polycrystalline methane hydrates, the half-cage order parameter (H-COP) was utilized [13,14]. H-COP was developed to recognize water cages based on the topological analysis of the tetrahedral network. And H-COP can be able to identify the water ring structure, half-polyhedral cages of water molecules, and the unique building blocks of water-based hydrates. H-COP was employed based on a cutoff distance of 3.2 Å in present work. To identify the hydrate cages, the computational protocol is shown as follows:

Firstly, a ring-statistics algorithm is utilized to distinguish all the four-membered rings, five-membered

rings, and six-membered rings. These membered rings can be used for the building blocks for the polyhedral cages in the hydrate systems.

Secondly, a topological analysis is employed to distinguish the formation of half-cages, *i.e.*, 5^6, 5^66^1, 5^66^2, $4^15^46^2$, $4^25^26^1$ and so on. For example, the 5^6 half-cage contains 15 water molecules, making up one central five-membered ring and five peripheral five-membered rings. Those half-cages are the key basis to form the water cages.

Lastly, a cluster-walk algorithm is preformed to identify the connectivity of the half-cages. Two half-cages are regarded to be connected if either of the following two criteria is met: (a) two half-cages share one and only one ring, regardless the types of the half-cages, and (b) two half-cages match their edges to form a complete cage. Hydrate water cages are obtained by iteratively finding all connected half-cages.

Section S6. Crystal Face Binding Energy

In this work, to compute the crystal face binding energy of bicrystals, all the simulation settings are identical to the procedure in preparing samples in the Section S1. System Preparations in our supplementary materials. Firstly, the energy of each given bicrystal at the equilibrium state is collected based on the mW water model. Secondly, the energy of each monocrystal with the same system size with the corresponding given bicrystals at the equilibrium state is also collected. Thirdly, the crystal face binding energy of bicrystals can be computed from the collected energy of the given bicrystal and the corresponding two monocrystals as the following equation:

$$E_{binding\ energy} = (E_{energy}^{bicrystal} - E_{energy}^{1} - E_{energy}^{2}) / S \quad (3)$$

where $E_{binding\ energy}$ is the crystal face binding energy of each given bicrystal, $E_{energy}^{bicrystal}$ is the energy of each given bicrystal at the equilibrium state, E_{energy}^{1} and E_{energy}^{2} is the energy of two monocrystals with the same system size with the corresponding given bicrystals at the equilibrium state, respectively. S is the connecting interfacial area of the given bicrystal.

Section S7. Centro-Symmetry Parameter

In solid-state systems, the centro-symmetry parameter (CSP) is a useful parameter of the local lattice disorder around a particle, and it is able to characterize whether the particle is part of a perfect lattice, a local defect, or at a surface. In our work, the CSP value is computed using the following equation from Kelchner *et al*.[15]

$$CSP = \sum_{i=1}^{N/2} \left| \vec{R}_i + \vec{R}_{i+N/2} \right|^2 \quad (4)$$

where the N is the nearest neighbors of each atom, $\vec{R}_i$ and $\vec{R}_{i+N/2}$ are vectors from the central atom to a particular pair of nearest neighbors. The nearest neighbors of each given water molecule in monocrystalline hydrate and ice grain interiors is different from that of each given water molecule in grain boundaries. In our work, the four nearest neighbors of each water molecule is used, and all the methane molecules are not shown to exhibit the different local lattice disorder clearly. As shown in Figure 4 in our main manuscript, the water molecules in GBs of the polycrystals show different CSP values with those in

187 the crystalline grain interiors, indicating different local lattice disorder between the GBs and crystalline
188 grain interiors.

189 **Section S8. Average Percentages of Three Grain Boundary Types**

190 In this work, the water molecules belonging to hydrate and ice grains were marked with different symbols
191 when we papered the polycrystals, *e.g.*, the water molecules in hydrate and ice grains were denoted by the
192 "$O_{hydrate}$" and "O_{ice}" respectively. As shown in Figure 5h and 5i in our main manuscript, all methane
193 particles are removed at first, and then the water particles in both ice and hydrate grain interiors are also
194 removed based on the so-called coordination number of a particle. The coordination number represents
195 the number of neighbors of each particle which are within a given cutoff radius. As we know, in perfect
196 hydrate and ice grain interiors, each water molecule is able to connect with four nearest water molecules
197 as neighbors. However, most of water particles at grain boundaries mainly have the different
198 coordination number. Though very few water particles at grain boundaries may have the same
199 coordination number as the water particles in both ice and hydrate grain interiors, this effect is negligible
200 as shown in Figure 5h in our main manuscript. To further eliminate this effect, four different sample
201 cases at each given ice grain content are analyzed to obtain the average percentages of three grain
202 boundary types (IIGBs, HIGBs, and HHGBs) in polycrystals as a function of ice grain content.

203 The water particles, which belong to hydrate and ice grains, can be distinguished from the marking
204 symbols above. Therefore, the water particles located at IIGBs, HIGBs, and HHGBs are able to have the

205 different combinations of marking symbols for water particles. For example, the water particles at
206 HIGBs are marked by the two symbols of "$O_{hydrate}$" and "O_{ice}" belonging to hydrate and ice grains,
207 respectively. Firstly, the number of water particles belonging to hydrate and ice grains can be roughly
208 counted based on the marking symbols, respectively. Then, if the distance between one water particle
209 belonging to hydrate grains and the other water particle belonging to ice grains is less than the given
210 value, we can roughly define that the two water particles belong to HIGBs. In this study, the given value is
211 set as 10 Å based on the analysis of the width of grain boundary structures and the diffusion of the water
212 particles at grain boundaries. Moreover, the number of water particles located at IIGBs and HHGBs can
213 also be roughly counted as the following equation:

214 $$N = N_{o-hydrate} + N_{o-ice} \tag{5}$$

215 $$N_{o-HHGBs} = N_{o-hydrate} - N_{o-HIGBs} \tag{6}$$

216 $$N_{o-IIGBs} = N_{o-ice} - N_{o-HIGBs} \tag{7}$$

217 where the N, $N_{o-hydrate}$, and N_{o-ice} is the total number of water particles at grain boundaries, the
218 number of water particles belonging to hydrate grains, and the number of water particles belonging to ice
219 grains, respectively. The $N_{o-HHGBs}$, $N_{o-HIGBs}$, and $N_{o-IIGBs}$ is the number of water particles at HHGBs,
220 HIGBs and IIGBs, respectively. At last, the percentages of three grain boundary types can be roughly
221 obtained through the number of water molecules located at three grain boundary types divided by the
222 total number of water molecules at grain boundaries.

223 **Supplementary Figures and Tables**

224 **Table S1:**

225 **Table S1. Maximum tensile strength of hydrate-ice polycrystals in our molecular simulation.**

Ice Content (%)	0	10	20	30	40	50
Confining Pressure (MPa)	10					
Maximum Tensile Strength (MPa)	411.38	351.96	298.38	269.65	254.04	237.56
Ice Content (%)	60	70	80	90	100	
Confining Pressure (MPa)	10					
Maximum Tensile Strength (MPa)	229.57	228.42	230.20	236.79	247.15	

226

Figure S1:

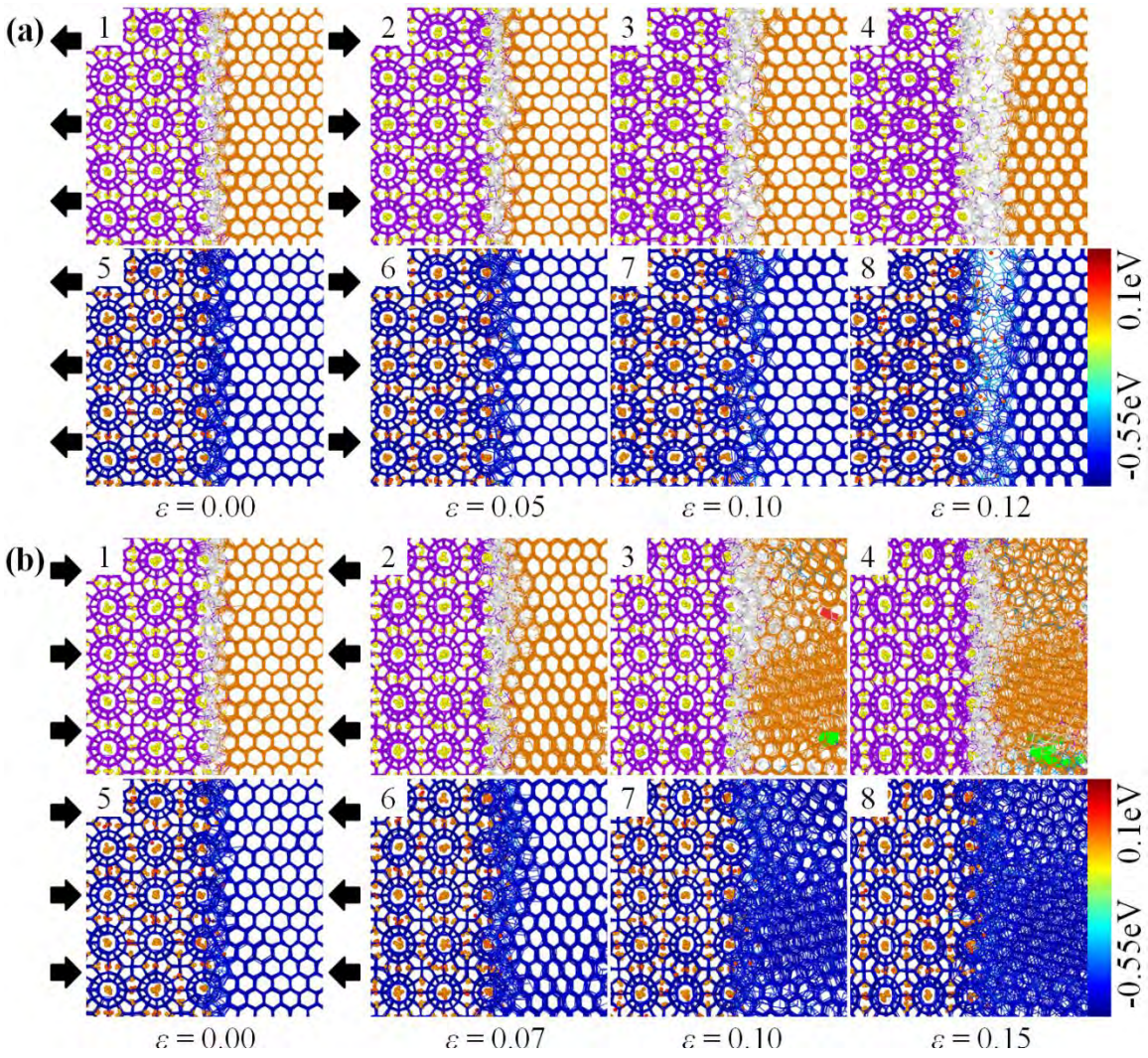

Figure S1. Localized snapshots of hydrate-ice (HI) bicrystals with $\{01\bar{1}0\}|\{1\,0\,0\}$ grain boundary structures. (a) Molecular snapshots of HI bicrystals under tension at different strains, respectively. (b) Molecular snapshots of HI bicrystals under compression at different strains, respectively. Water particles which form hexagonal ice in snapshots #1-4 are colored according to the identified type of structural phase; Hexagonal, cubic and unidentified water structures are rendered by orange, light blue and white for

clarification, respectively. Strain-induced dislocations in HI bicrystals are illustrated by solid segments. Different colored segments represent different type of dislocation; $1/3\langle 1\,\bar{2}\,1\,0\rangle$, $\langle 0\,0\,0\,1\rangle$, $\langle 1\,\bar{1}\,0\,0\rangle$, $1/3\langle 1\,\bar{1}\,0\,0\rangle$, and unidentified dislocations are rendered by green, yellow, pink, sky-blue and red for clarification, respectively. Water particles and methane particles which form sI structure methane hydrate in snapshots #1-4 are colored by purple and yellow, respectively. All particles in snapshots #5-8 are rendered according to their potential energy.

Figure S2:

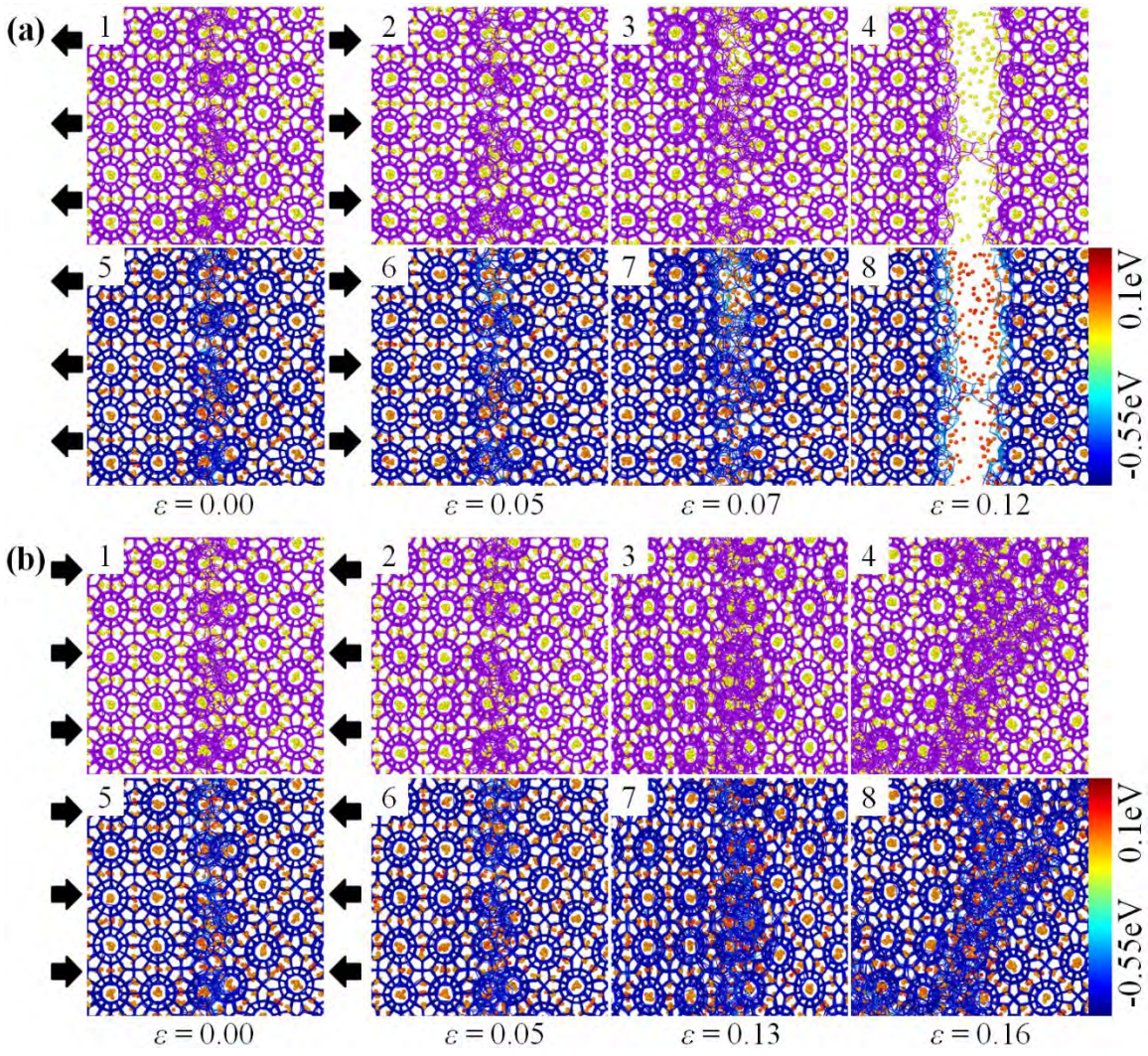

Figure S2. Localized snapshots of hydrate-hydrate (HH) bicrystals with {1 0 0} | {1 1 0} **grain boundary structures.** (a) Molecular snapshots of HH bicrystals under tension at different strains, respectively. (b) Molecular snapshots of HH bicrystals under compression at different strains, respectively. Water particles and methane particles in snapshots #1-4 are colored by purple and yellow, respectively. All particles in snapshots #5-8 are rendered according to their potential energy.

247 **Figure S3:**

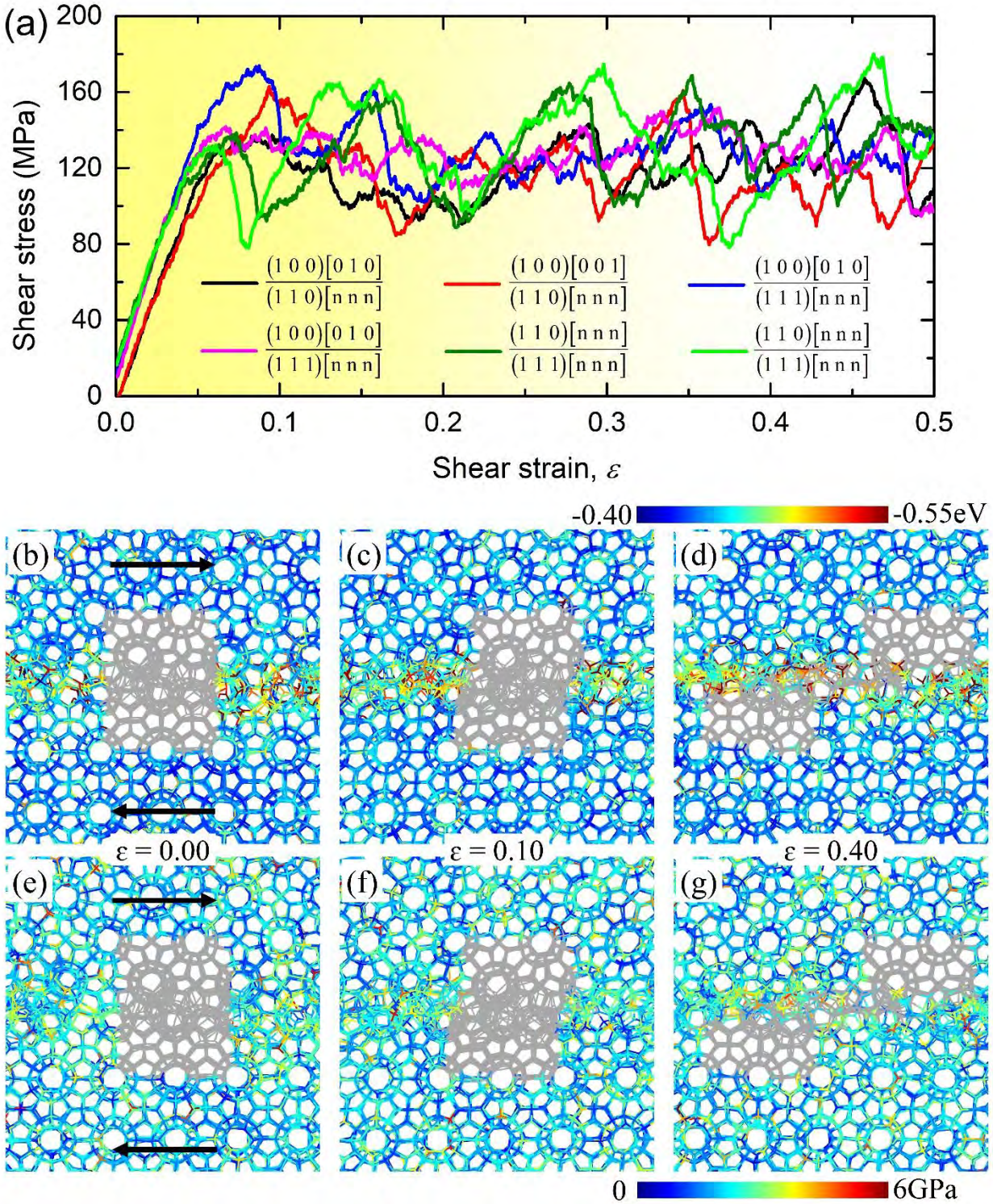

248

Figure S3. Mechanical shear response of hydrate-hydrate (HH) bicrystalline structures. (a) The shear stress-strain curves of bicrystals with different grain boundary structures under nonequivalent directional shear deformation, respectively. (b)-(g) Localized snapshots of bicrystalline HH with $\{1\,0\,0\}\,|\,\{1\,1\,0\}$ grain boundary structure subjected to $\frac{(1\,0\,0)[0\,0\,1]}{(1\,1\,0)[\mathrm{n\,n\,n}]}$ directional shear loadings at different strains, respectively. Black arrows indicate the shear loading directions. The notation of "n n n" represents these undetermined shearing directions. As we seen in in Figure S3a, all shear responses are very similar in molecular dynamics simulations. It is not important to determine the shearing directions. Water particles in Figure S3b-S3d are rendered according to their potential energy. Water particles in Figure S3e-S3g are colored according to the *von Mises* stress. All methane particles are removed to observe the grain boundary changes. The selected particles are rendered by gray in Figure S3b-S3g to monitor grain boundary sliding.

Figure S4:

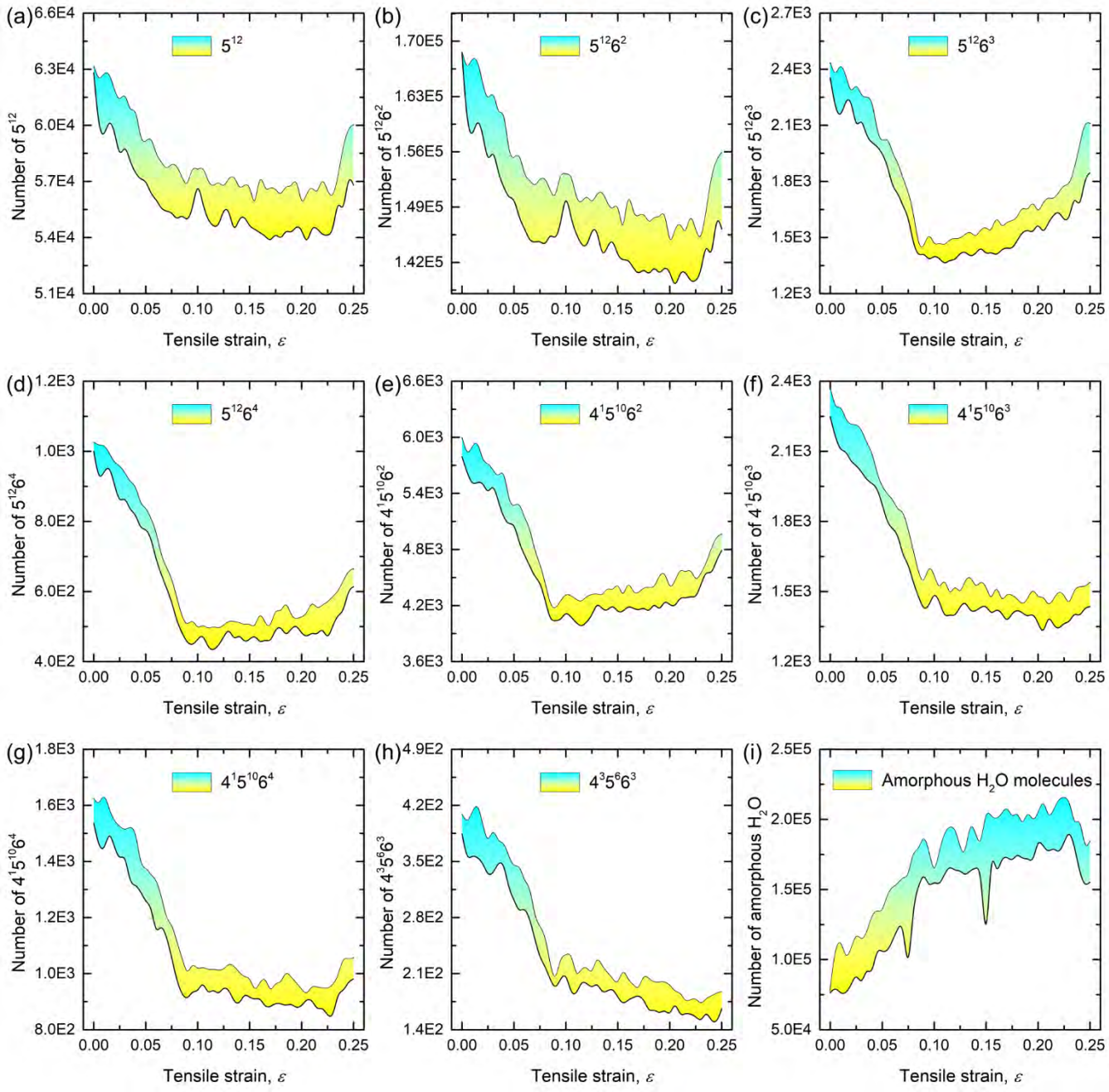

Figure S4. The number of identified water cages in sI hydrate polycrystals containing 0% water ice under tension. Eight types of water polyhedral cages and amorphous water ice are respectively identified

during the whole tensile deformation. (a) 5^{12} water cages. (b) $5^{12}6^2$ water cages. (c) $5^{12}6^3$ water cages. (d) $5^{12}6^4$ water cages. (e) $4^15^{10}6^2$ water cages. (f) $4^15^{10}6^3$ water cages. (g) $4^15^{10}6^4$ water cages. (h) $4^35^66^3$ water cages. (i) Amorphous water molecules.

Figure S5:

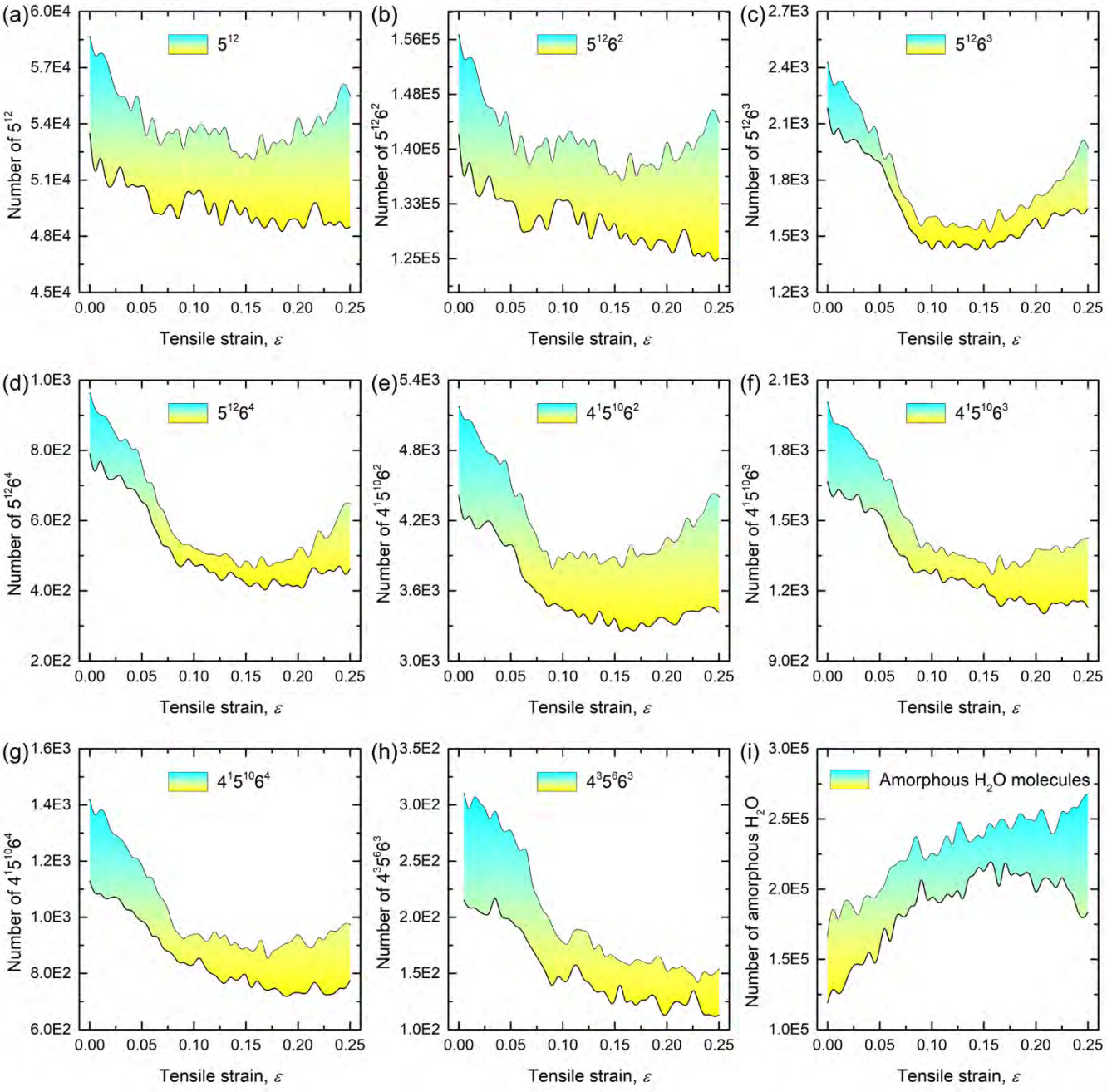

Figure S5. The number of identified water cages in sI hydrate polycrystals containing 10% water ice under tension. Eight types of water polyhedral cages and amorphous water ice are respectively

identified during the whole tensile deformation. (a) 5^{12} water cages. (b) $5^{12}6^2$ water cages. (c) $5^{12}6^3$ water cages. (d) $5^{12}6^4$ water cages. (e) $4^15^{10}6^2$ water cages. (f) $4^15^{10}6^3$ water cages. (g) $4^15^{10}6^4$ water cages. (h) $4^35^66^3$ water cages. (i) Amorphous water molecules.

Figure S6:

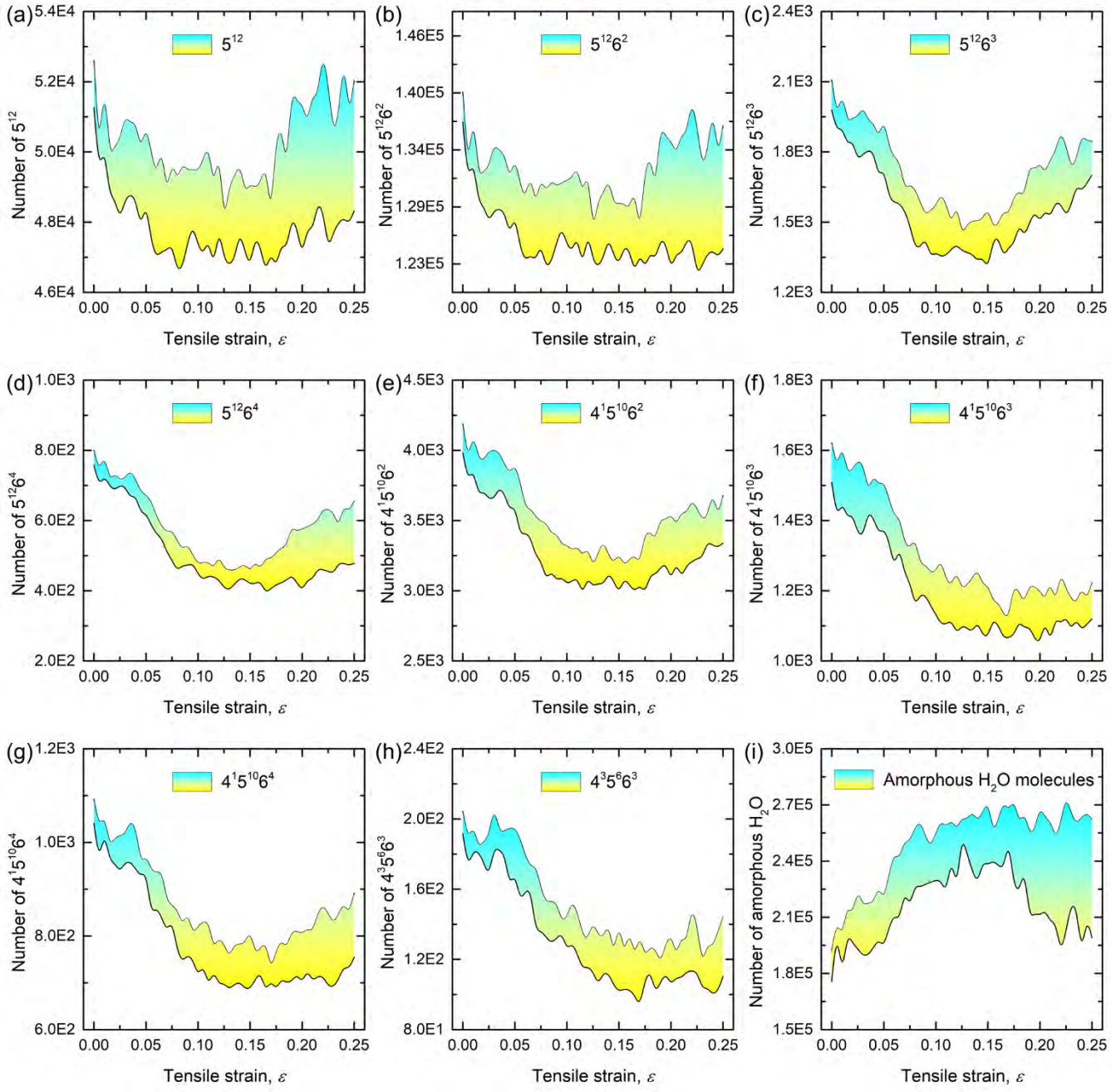

Figure S6. The number of identified water cages in sI hydrate polycrystals containing 20% water ice under tension. Eight types of water polyhedral cages and amorphous water ice are respectively

identified during the whole tensile deformation. (a) 5^{12} water cages. (b) $5^{12}6^2$ water cages. (c) $5^{12}6^3$ water cages. (d) $5^{12}6^4$ water cages. (e) $4^15^{10}6^2$ water cages. (f) $4^15^{10}6^3$ water cages. (g) $4^15^{10}6^4$ water cages. (h) $4^35^66^3$ water cages. (i) Amorphous water molecules.

294 **Figure S7:**

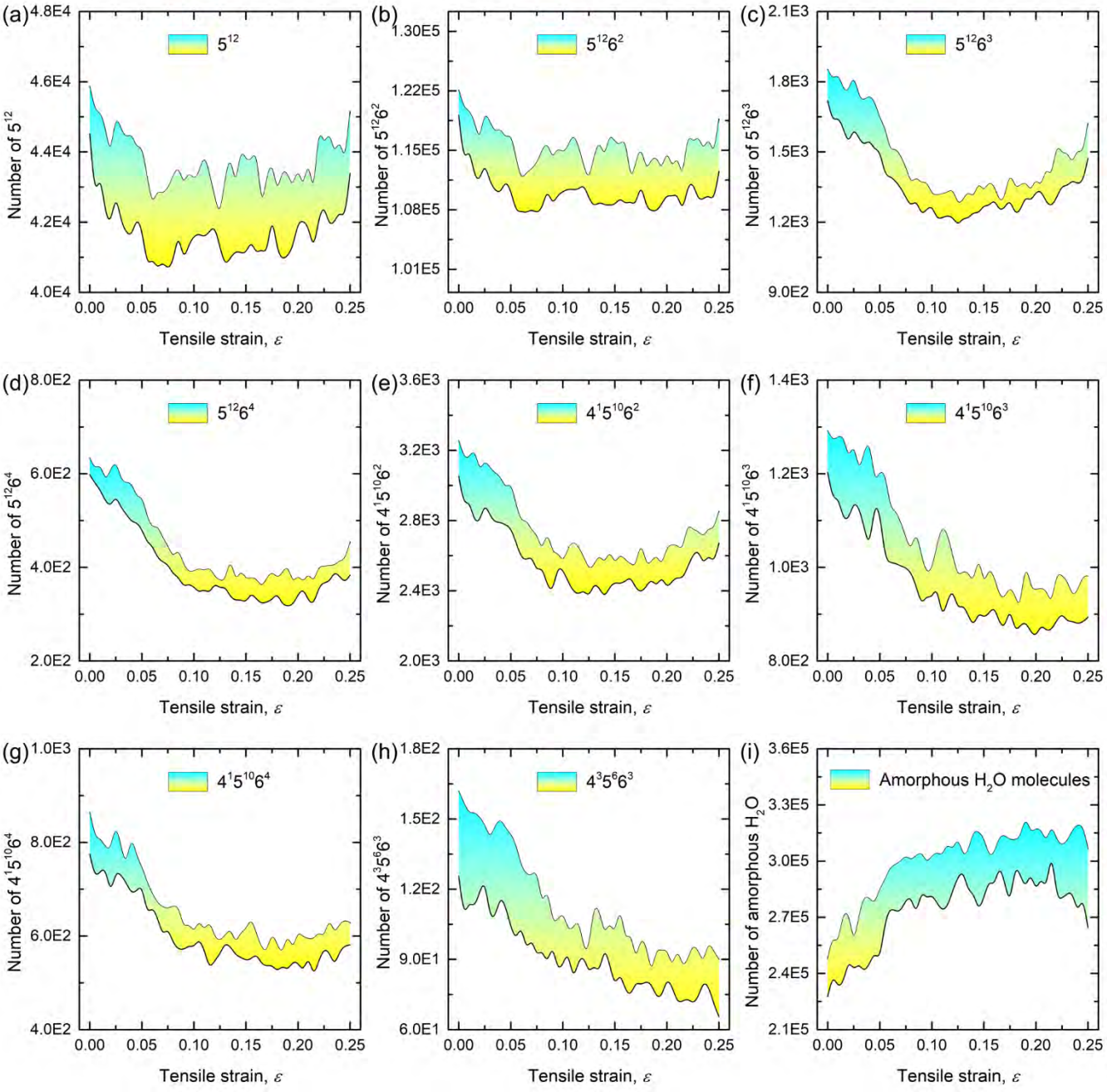

295

296 **Figure S7. The number of identified water cages in sI hydrate polycrystals containing 30% water**

297 **ice under tension.** Eight types of water polyhedral cages and amorphous water ice are respectively

identified during the whole tensile deformation. (a) 5^{12} water cages. (b) $5^{12}6^2$ water cages. (c) $5^{12}6^3$ water cages. (d) $5^{12}6^4$ water cages. (e) $4^15^{10}6^2$ water cages. (f) $4^15^{10}6^3$ water cages. (g) $4^15^{10}6^4$ water cages. (h) $4^35^66^3$ water cages. (i) Amorphous water molecules.

Figure S8:

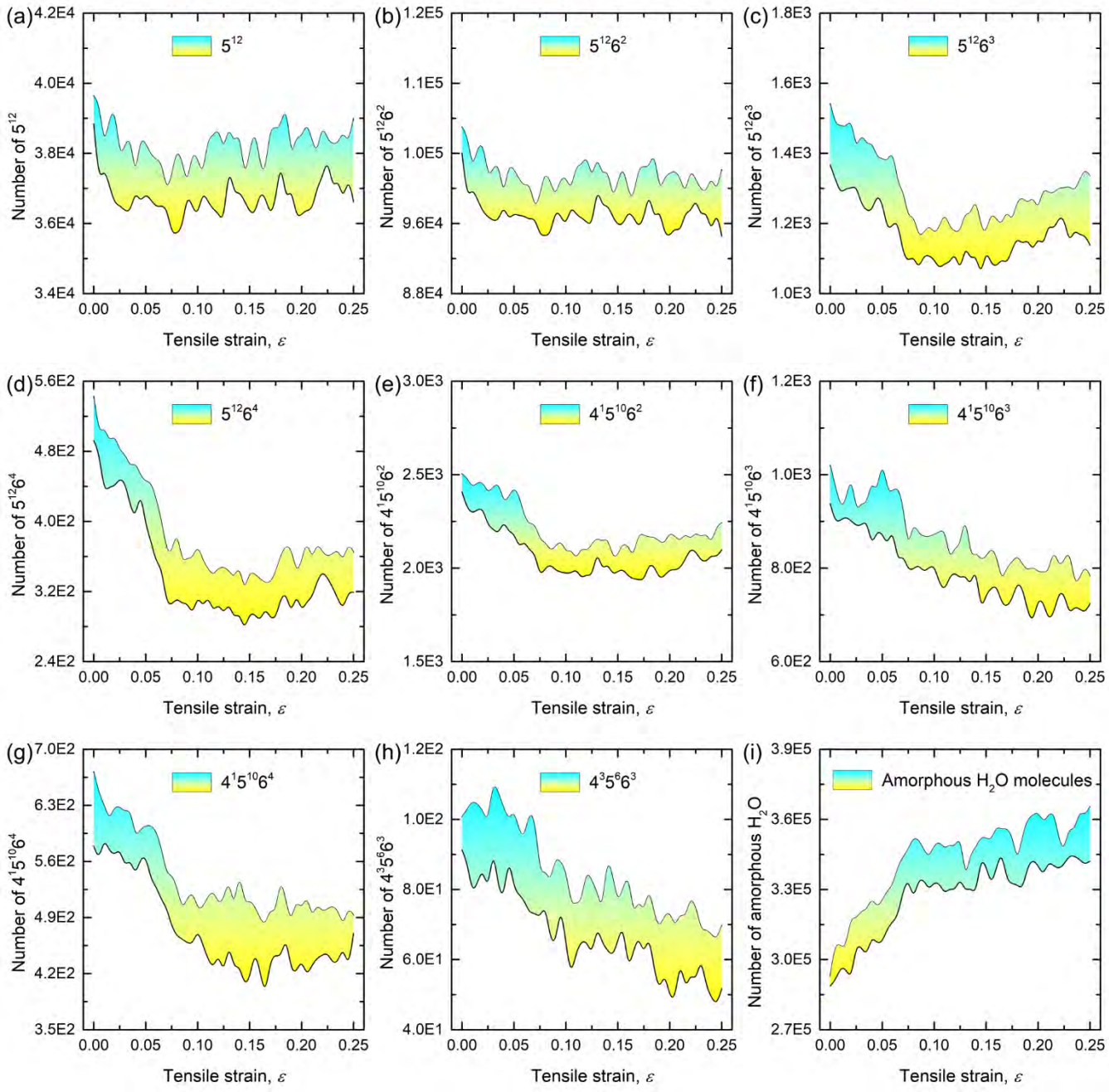

Figure S8. The number of identified water cages in sI hydrate polycrystals containing 40% water ice under tension. Eight types of water polyhedral cages and amorphous water ice are respectively

identified during the whole tensile deformation. (a) 5^{12} water cages. (b) $5^{12}6^2$ water cages. (c) $5^{12}6^3$ water cages. (d) $5^{12}6^4$ water cages. (e) $4^15^{10}6^2$ water cages. (f) $4^15^{10}6^3$ water cages. (g) $4^15^{10}6^4$ water cages. (h) $4^35^66^3$ water cages. (i) Amorphous water molecules.

Figure S9:

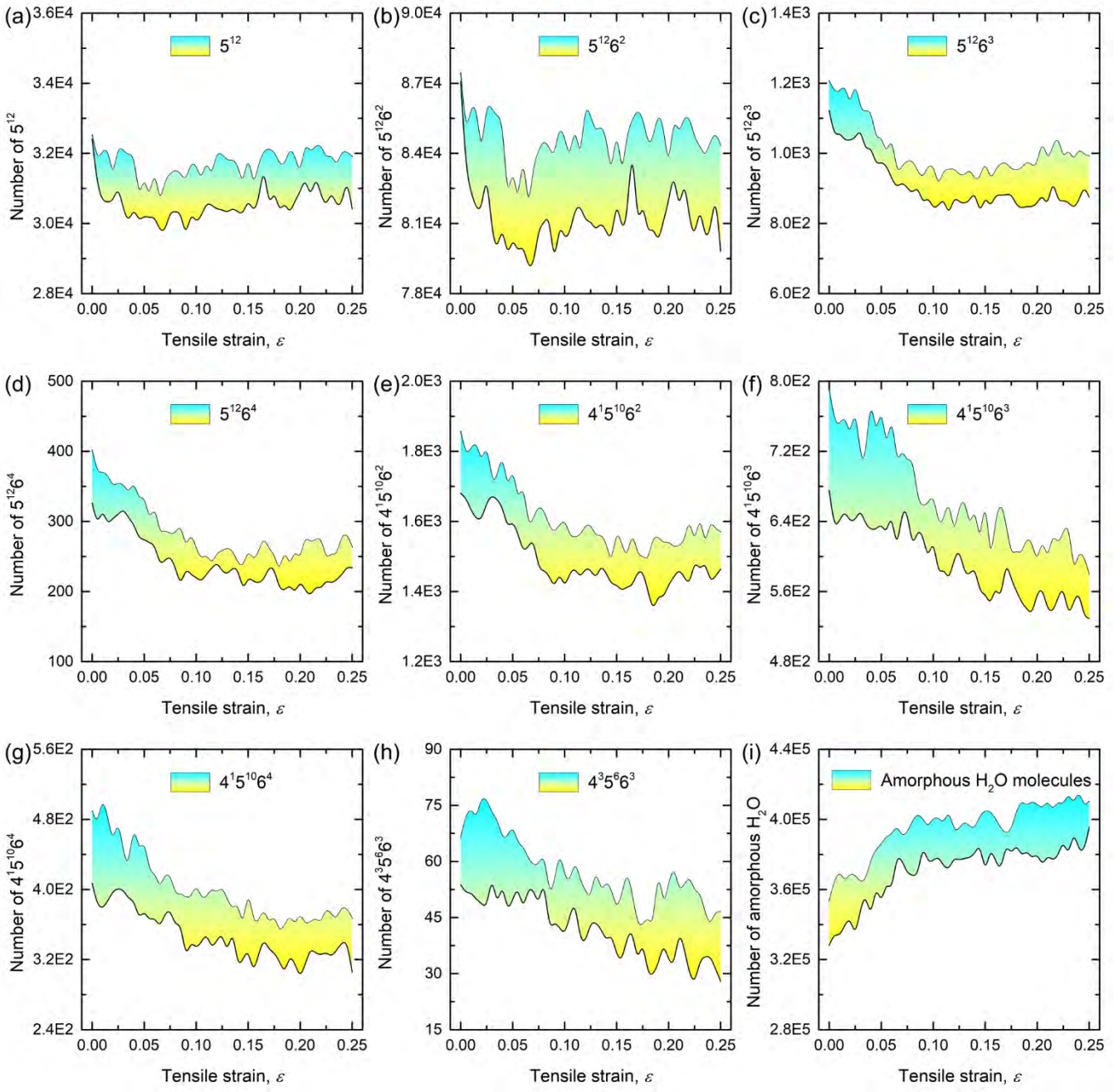

Figure S9. The number of identified water cages in sI hydrate polycrystals containing 50% water ice under tension. Eight types of water polyhedral cages and amorphous water ice are respectively

identified during the whole tensile deformation. (a) 5^{12} water cages. (b) $5^{12}6^2$ water cages. (c) $5^{12}6^3$ water cages. (d) $5^{12}6^4$ water cages. (e) $4^15^{10}6^2$ water cages. (f) $4^15^{10}6^3$ water cages. (g) $4^15^{10}6^4$ water cages. (h) $4^35^66^3$ water cages. (i) Amorphous water molecules.

Figure S10:

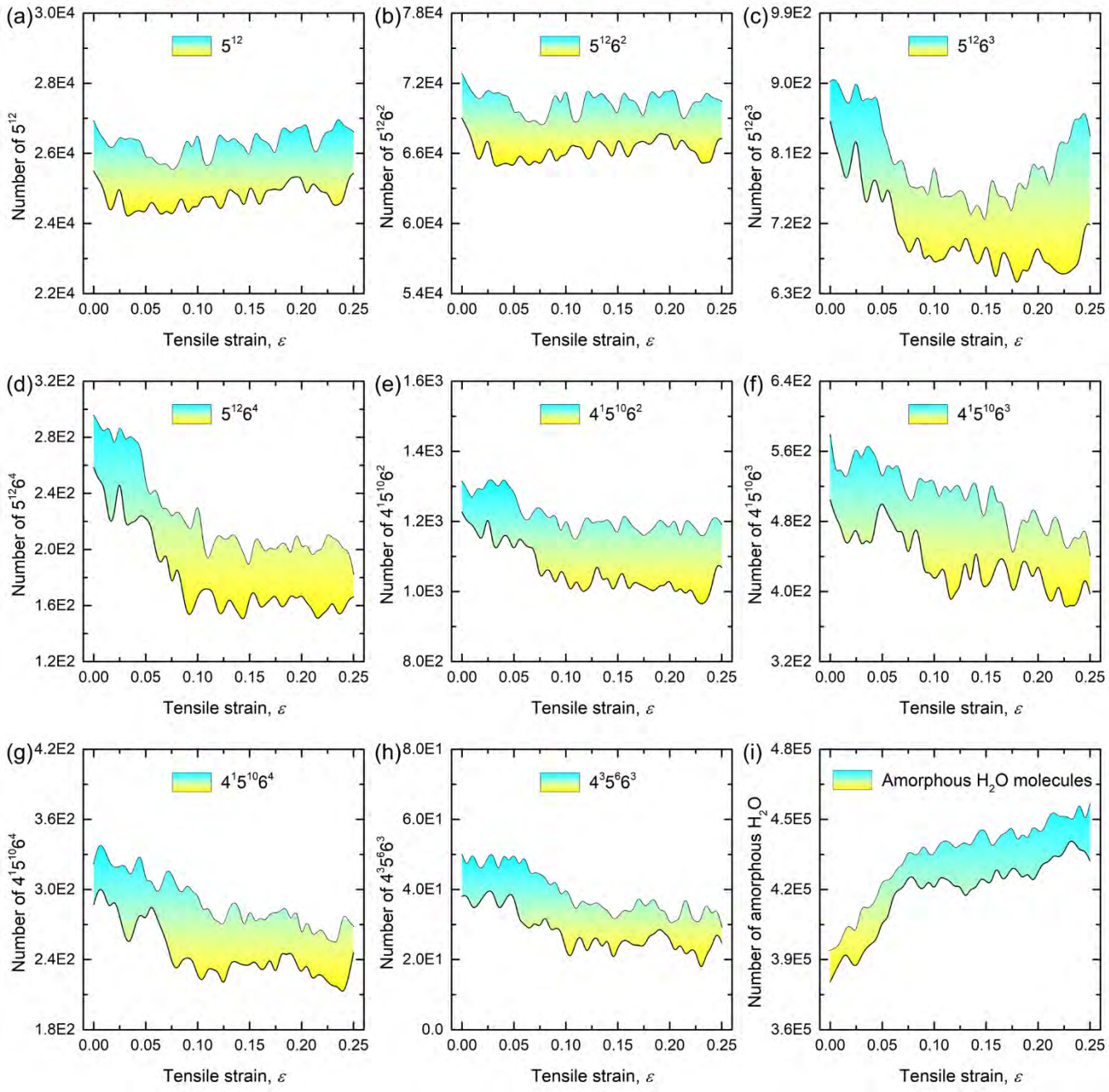

Figure S10. The number of identified water cages in sI hydrate polycrystals containing 60% water ice under tension. Eight types of water polyhedral cages and amorphous water ice are respectively

identified during the whole tensile deformation. (a) 5^{12} water cages. (b) $5^{12}6^2$ water cages. (c) $5^{12}6^3$ water cages. (d) $5^{12}6^4$ water cages. (e) $4^15^{10}6^2$ water cages. (f) $4^15^{10}6^3$ water cages. (g) $4^15^{10}6^4$ water cages. (h) $4^35^66^3$ water cages. (i) Amorphous water molecules.

Figure S11:

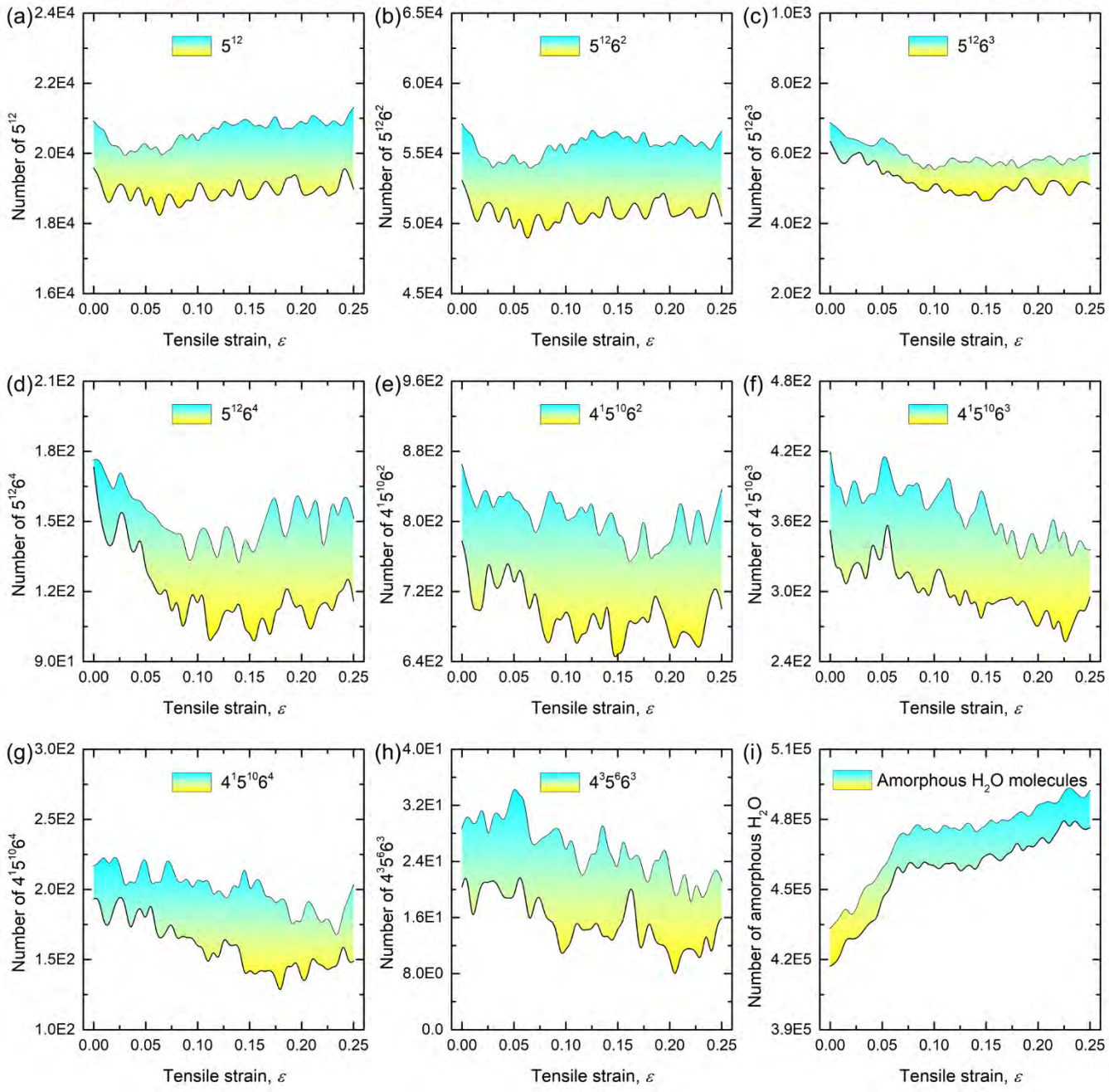

Figure S11. The number of identified water cages in sI hydrate polycrystals containing 70% water ice under tension. Eight types of water polyhedral cages and amorphous water ice are respectively

identified during the whole tensile deformation. (a) 5^{12} water cages. (b) $5^{12}6^2$ water cages. (c) $5^{12}6^3$ water cages. (d) $5^{12}6^4$ water cages. (e) $4^15^{10}6^2$ water cages. (f) $4^15^{10}6^3$ water cages. (g) $4^15^{10}6^4$ water cages. (h) $4^35^66^3$ water cages. (i) Amorphous water molecules.

Figure S12:

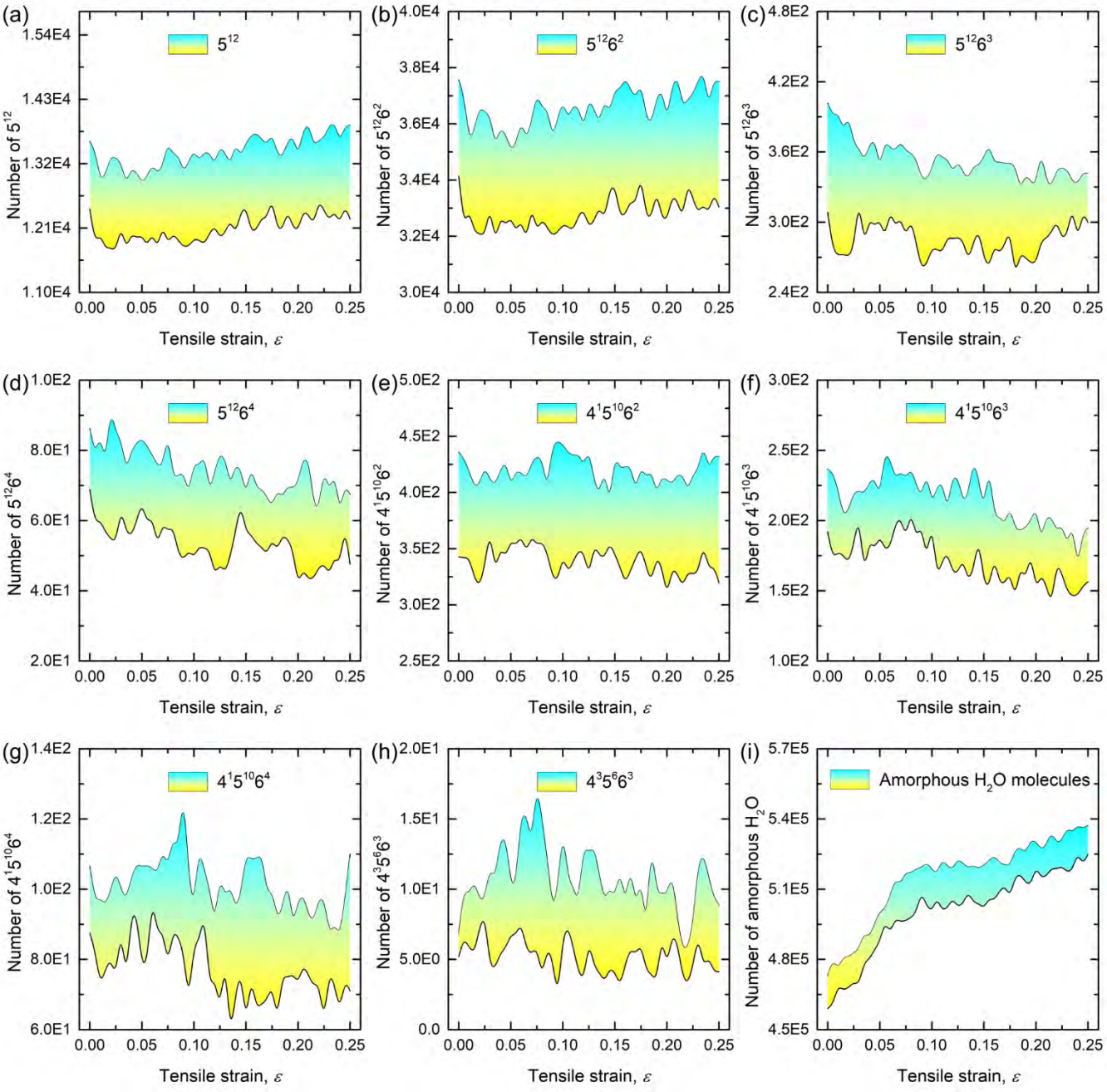

Figure S12. The number of identified water cages in sI hydrate polycrystals containing 80% water ice under tension. Eight types of water polyhedral cages and amorphous water ice are respectively

identified during the whole tensile deformation. (a) 5^{12} water cages. (b) $5^{12}6^2$ water cages. (c) $5^{12}6^3$ water cages. (d) $5^{12}6^4$ water cages. (e) $4^15^{10}6^2$ water cages. (f) $4^15^{10}6^3$ water cages. (g) $4^15^{10}6^4$ water cages. (h) $4^35^66^3$ water cages. (i) Amorphous water molecules.

Figure S13:

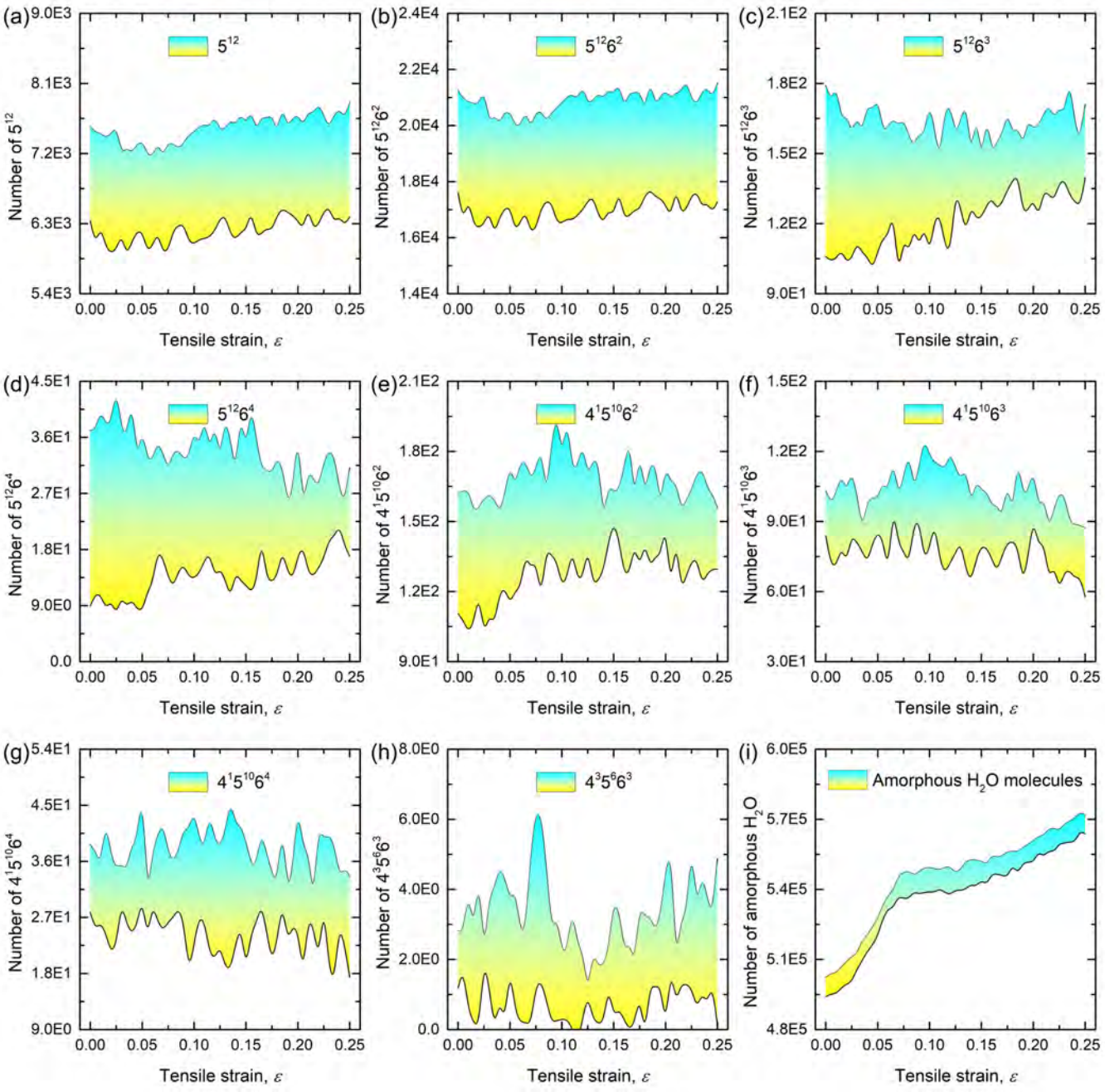

Figure 13. The number of identified water cages in sI hydrate polycrystals containing 90% water ice under tension. Eight types of water polyhedral cages and amorphous water ice are respectively

identified during the whole tensile deformation. (a) 5^{12} water cages. (b) $5^{12}6^2$ water cages. (c) $5^{12}6^3$ water cages. (d) $5^{12}6^4$ water cages. (e) $4^15^{10}6^2$ water cages. (f) $4^15^{10}6^3$ water cages. (g) $4^15^{10}6^4$ water cages. (h) $4^35^66^3$ water cages. (i) Amorphous water molecules.

Figure S14:

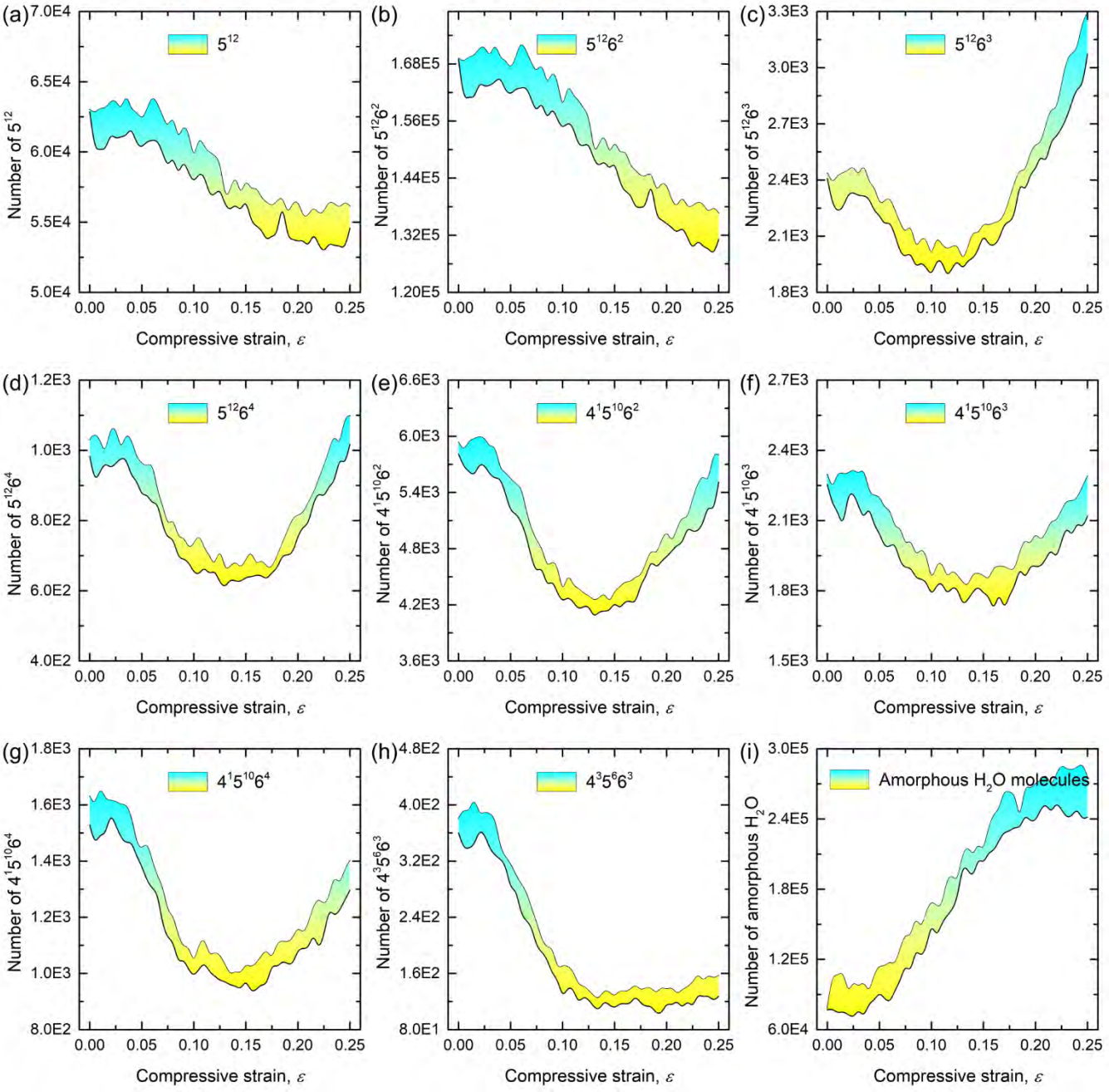

Figure S14. The number of identified water cages in sI hydrate polycrystals containing 0% water ice under compression. Eight types of water polyhedral cages and amorphous water ice are respectively

identified during the whole compressive deformation. (a) 5^{12} water cages. (b) $5^{12}6^2$ water cages. (c) $5^{12}6^3$ water cages. (d) $5^{12}6^4$ water cages. (e) $4^15^{10}6^2$ water cages. (f) $4^15^{10}6^3$ water cages. (g) $4^15^{10}6^4$ water cages. (h) $4^35^66^3$ water cages. (i) Amorphous water molecules.

Figure S15:

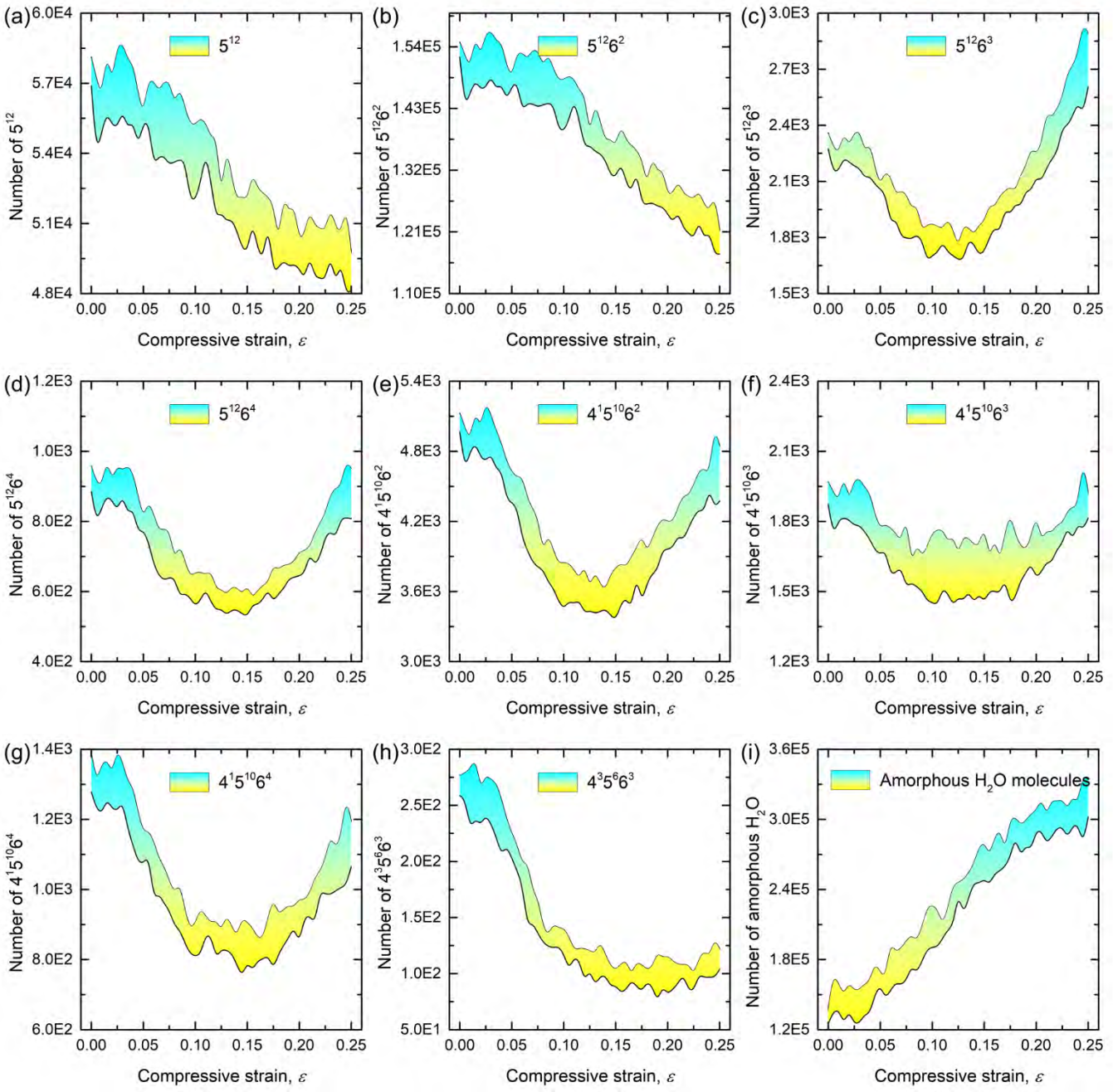

Figure S15. The number of identified water cages in sI hydrate polycrystals containing 10% water ice under compression. Eight types of water polyhedral cages and amorphous water ice are respectively

identified during the whole compressive deformation. (a) 5^{12} water cages. (b) $5^{12}6^2$ water cages. (c) $5^{12}6^3$ water cages. (d) $5^{12}6^4$ water cages. (e) $4^15^{10}6^2$ water cages. (f) $4^15^{10}6^3$ water cages. (g) $4^15^{10}6^4$ water cages. (h) $4^35^66^3$ water cages. (i) Amorphous water molecules.

Figure S16:

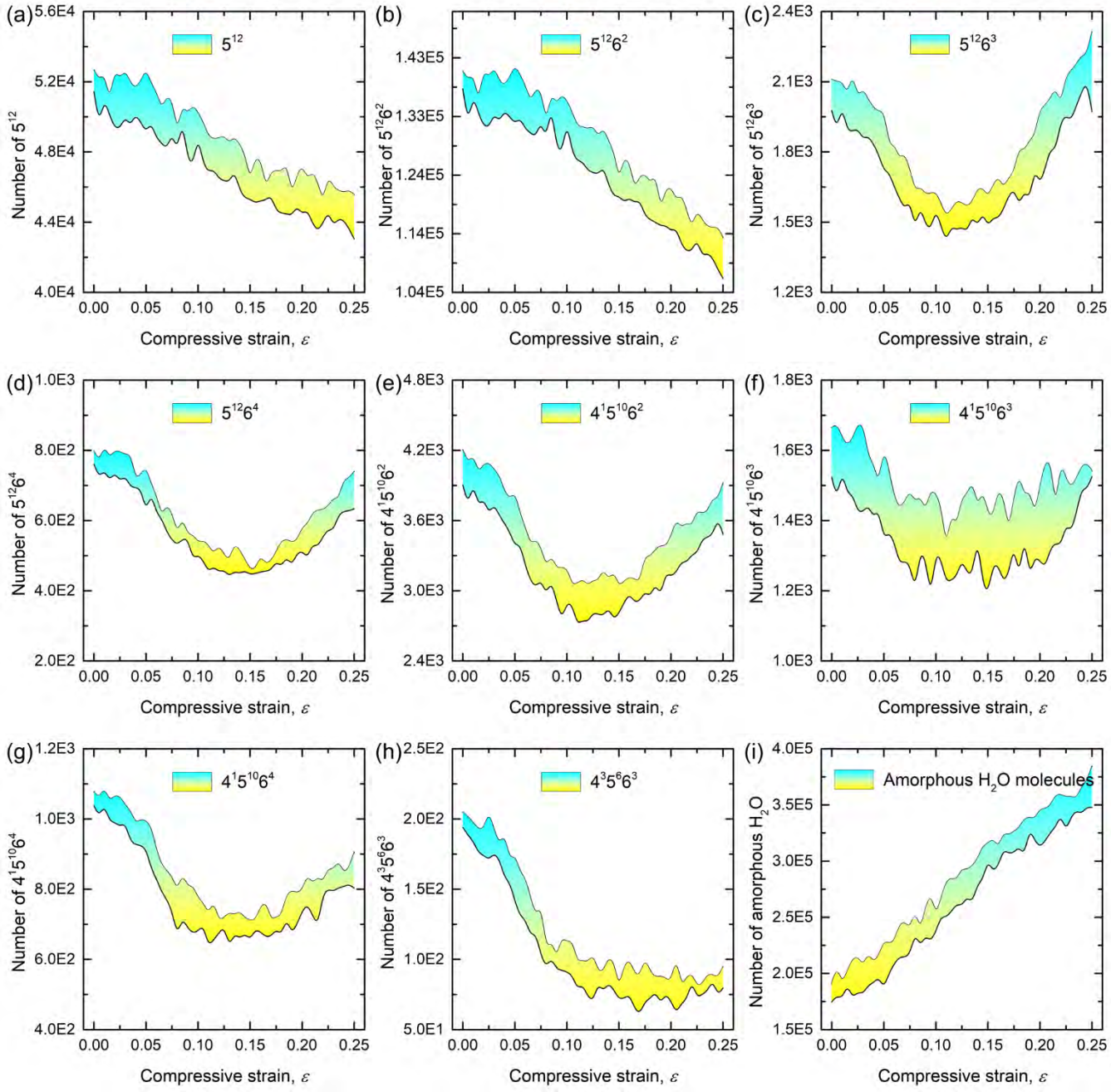

Figure S16. The number of identified water cages in sI hydrate polycrystals containing 20% water ice under compression. Eight types of water polyhedral cages and amorphous water ice are respectively

identified during the whole compressive deformation. (a) 5^{12} water cages. (b) $5^{12}6^2$ water cages. (c) $5^{12}6^3$ water cages. (d) $5^{12}6^4$ water cages. (e) $4^15^{10}6^2$ water cages. (f) $4^15^{10}6^3$ water cages. (g) $4^15^{10}6^4$ water cages. (h) $4^35^66^3$ water cages. (i) Amorphous water molecules.

Figure S17:

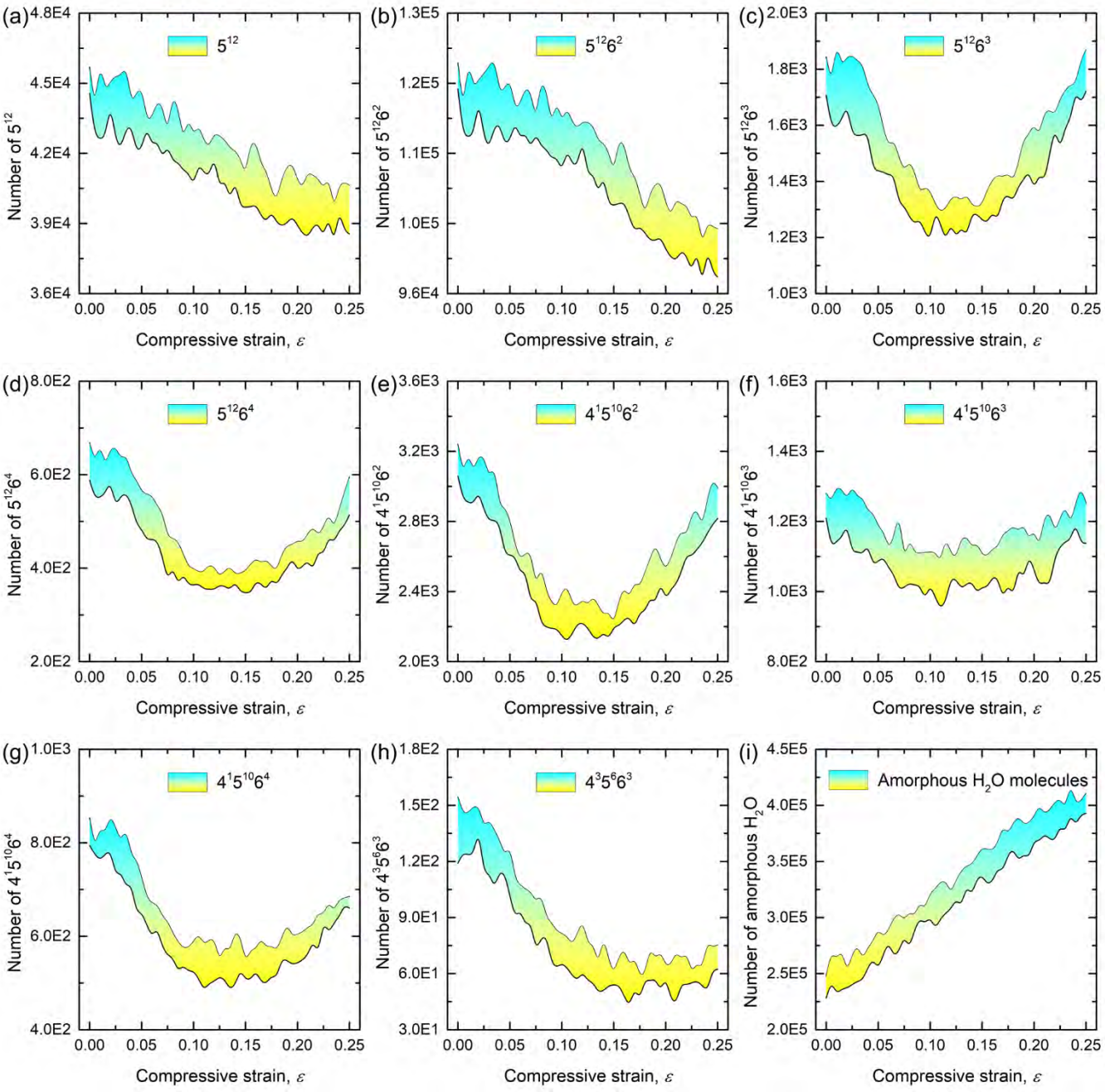

Figure S17. The number of identified water cages in sI hydrate polycrystals containing 30% water ice under compression. Eight types of water polyhedral cages and amorphous water ice are respectively

identified during the whole compressive deformation. (a) 5^{12} water cages. (b) $5^{12}6^2$ water cages. (c) $5^{12}6^3$ water cages. (d) $5^{12}6^4$ water cages. (e) $4^15^{10}6^2$ water cages. (f) $4^15^{10}6^3$ water cages. (g) $4^15^{10}6^4$ water cages. (h) $4^35^66^3$ water cages. (i) Amorphous water molecules.

Figure S18:

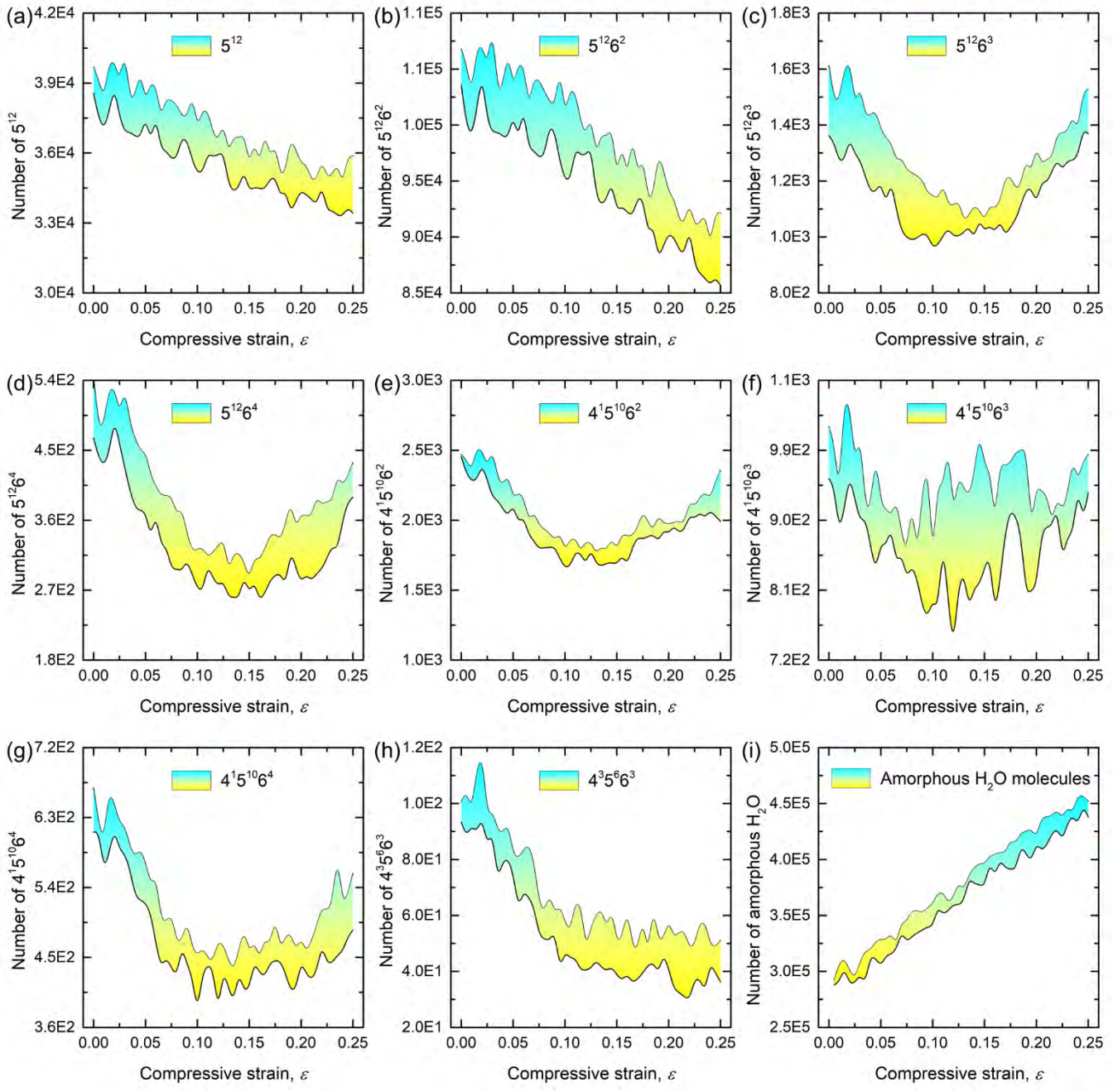

Figure S18. The number of identified water cages in sI hydrate polycrystals containing 40% water ice under compression. Eight types of water polyhedral cages and amorphous water ice are respectively

identified during the whole compressive deformation. (a) 5^{12} water cages. (b) $5^{12}6^2$ water cages. (c) $5^{12}6^3$ water cages. (d) $5^{12}6^4$ water cages. (e) $4^15^{10}6^2$ water cages. (f) $4^15^{10}6^3$ water cages. (g) $4^15^{10}6^4$ water cages. (h) $4^35^66^3$ water cages. (i) Amorphous water molecules.

Figure S19:

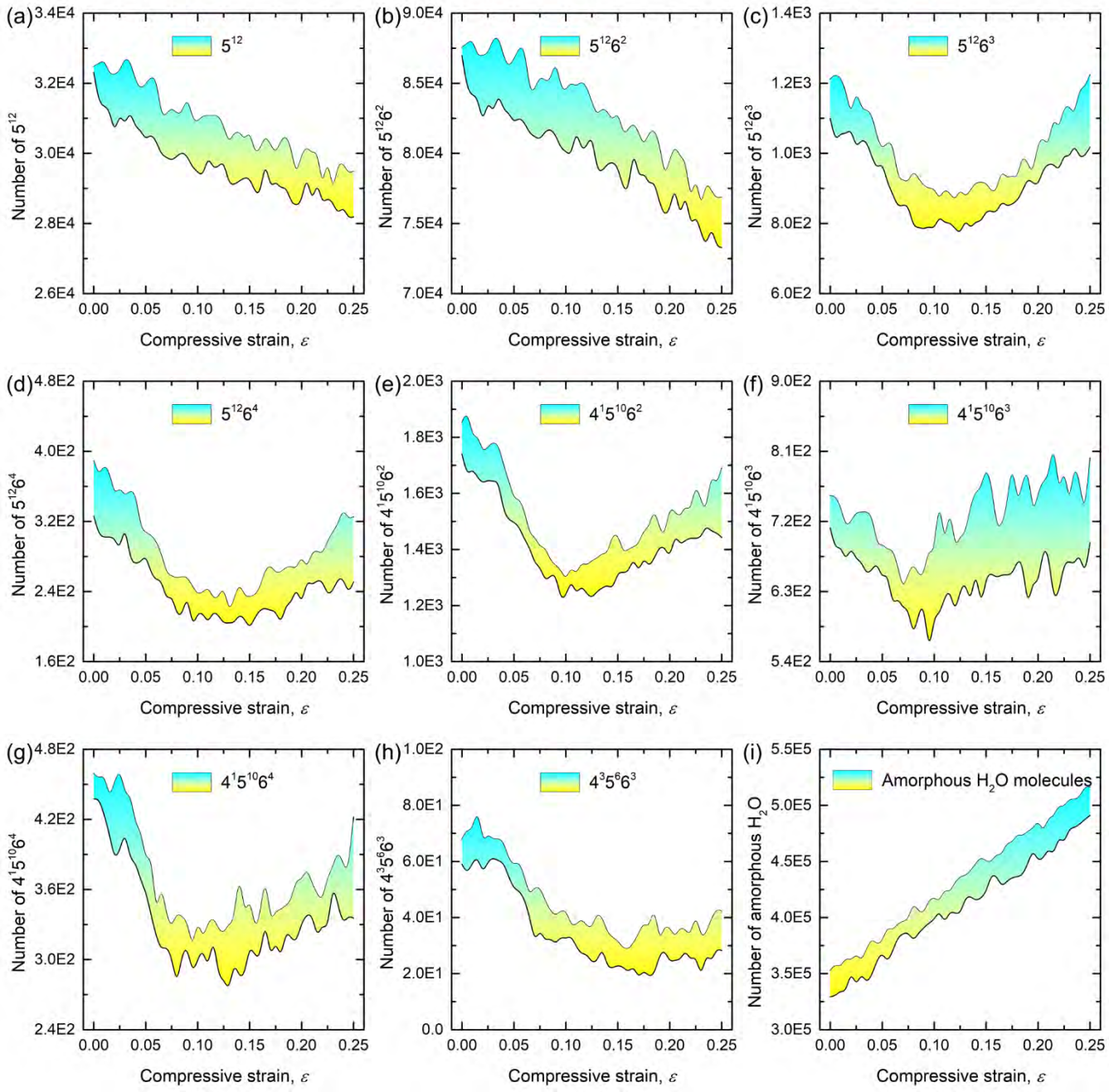

Figure S19. The number of identified water cages in sI hydrate polycrystals containing 50% water ice under compression. Eight types of water polyhedral cages and amorphous water ice are respectively

identified during the whole compressive deformation. (a) 5^{12} water cages. (b) $5^{12}6^2$ water cages. (c) $5^{12}6^3$ water cages. (d) $5^{12}6^4$ water cages. (e) $4^15^{10}6^2$ water cages. (f) $4^15^{10}6^3$ water cages. (g) $4^15^{10}6^4$ water cages. (h) $4^35^66^3$ water cages. (i) Amorphous water molecules.

Figure S20:

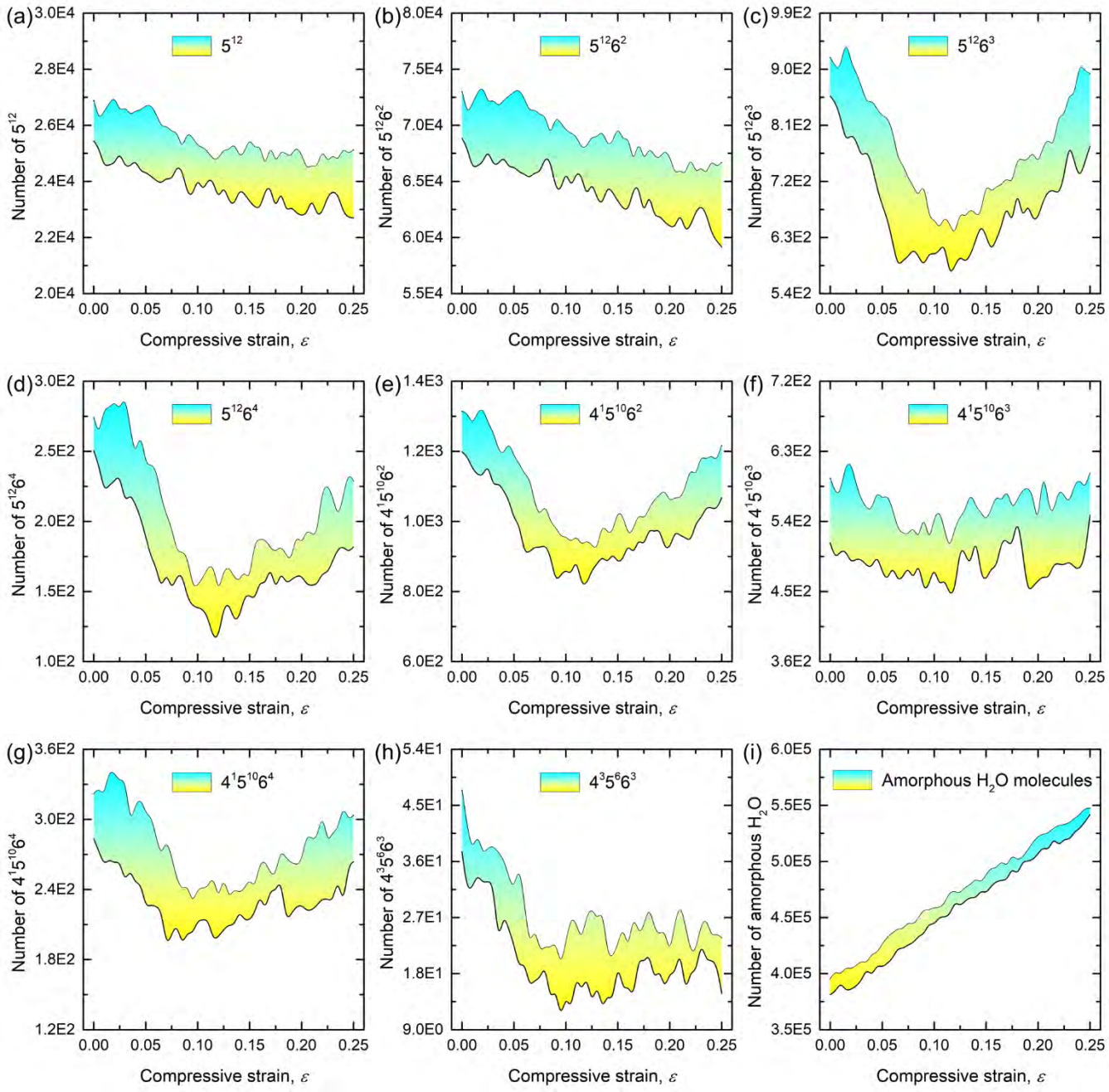

Figure S20. The number of identified water cages in sI hydrate polycrystals containing 60% water ice under compression. Eight types of water polyhedral cages and amorphous water ice are respectively

identified during the whole compressive deformation. (a) 5^{12} water cages. (b) $5^{12}6^2$ water cages. (c) $5^{12}6^3$ water cages. (d) $5^{12}6^4$ water cages. (e) $4^15^{10}6^2$ water cages. (f) $4^15^{10}6^3$ water cages. (g) $4^15^{10}6^4$ water cages. (h) $4^35^66^3$ water cages. (i) Amorphous water molecules.

Figure S21:

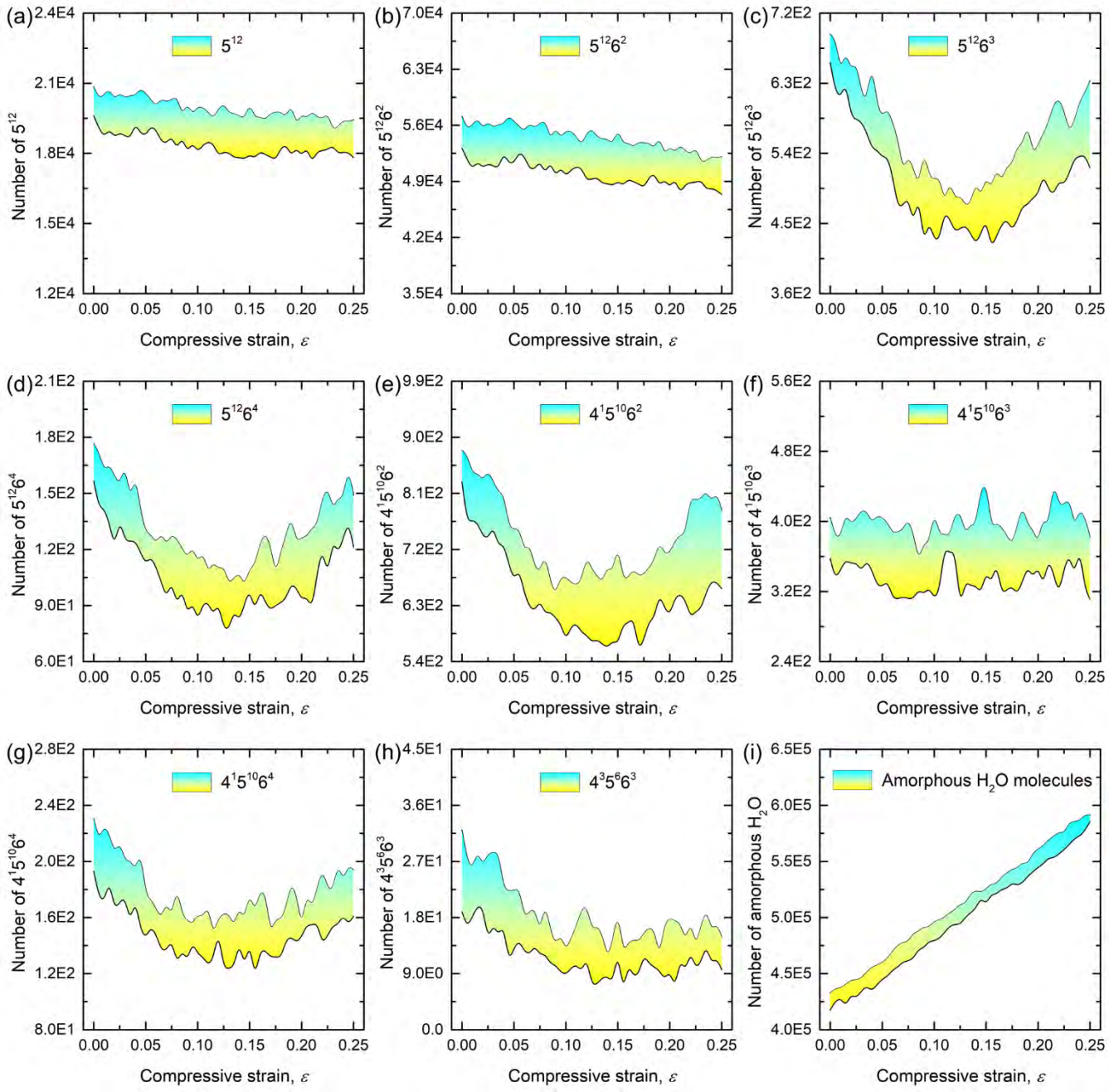

Figure S21. The number of identified water cages in sI hydrate polycrystals containing 70% water ice under compression. Eight types of water polyhedral cages and amorphous water ice are respectively

identified during the whole compressive deformation. (a) 5^{12} water cages. (b) $5^{12}6^2$ water cages. (c) $5^{12}6^3$ water cages. (d) $5^{12}6^4$ water cages. (e) $4^15^{10}6^2$ water cages. (f) $4^15^{10}6^3$ water cages. (g) $4^15^{10}6^4$ water cages. (h) $4^35^66^3$ water cages. (i) Amorphous water molecules.

Figure S22:

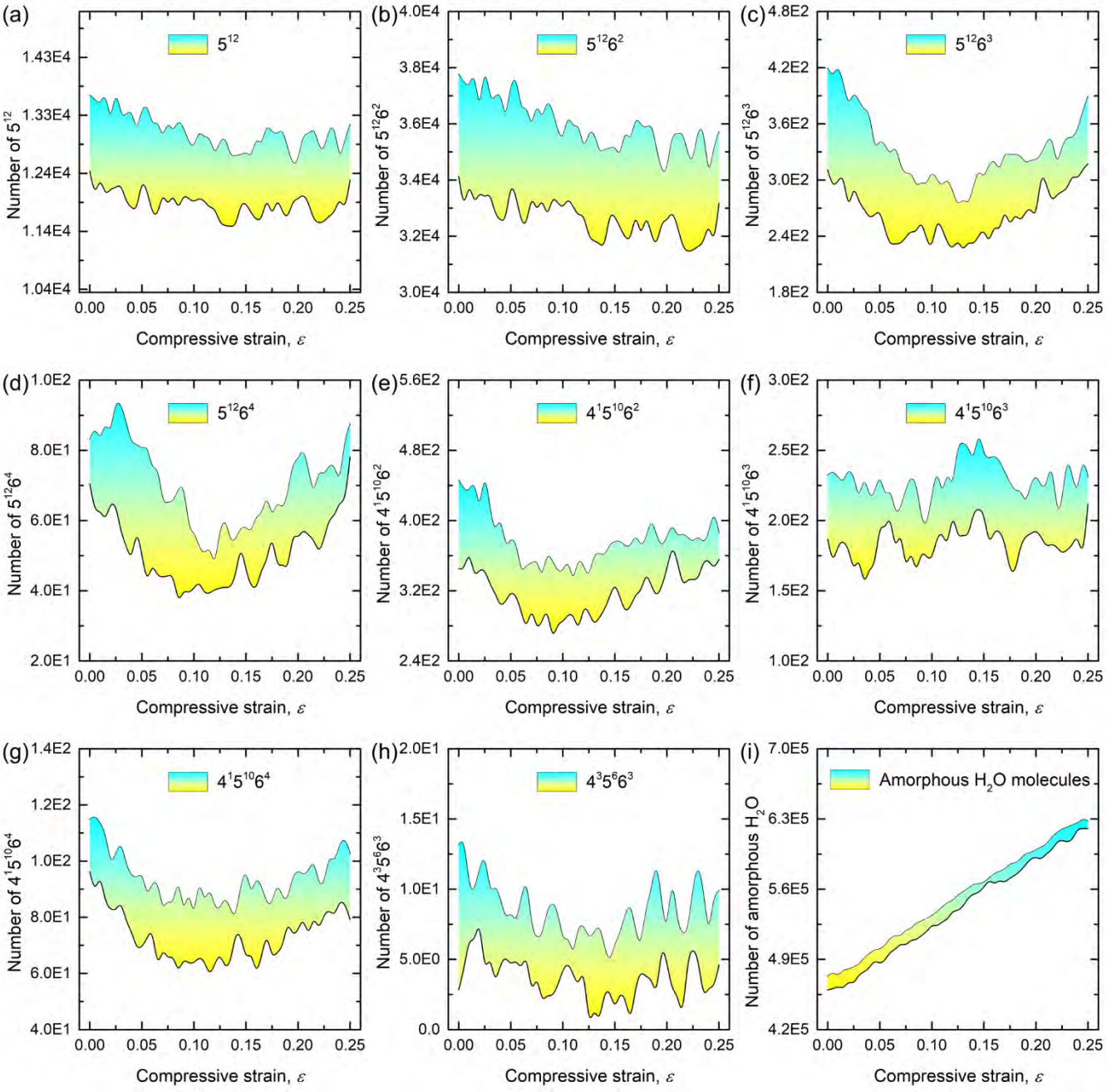

Figure S22. The number of identified water cages in sI hydrate polycrystals containing 80% water ice under compression. Eight types of water polyhedral cages and amorphous water ice are respectively

identified during the whole compressive deformation. (a) 5^{12} water cages. (b) $5^{12}6^2$ water cages. (c) $5^{12}6^3$ water cages. (d) $5^{12}6^4$ water cages. (e) $4^15^{10}6^2$ water cages. (f) $4^15^{10}6^3$ water cages. (g) $4^15^{10}6^4$ water cages. (h) $4^35^66^3$ water cages. (i) Amorphous water molecules.

406 **Figure S23:**

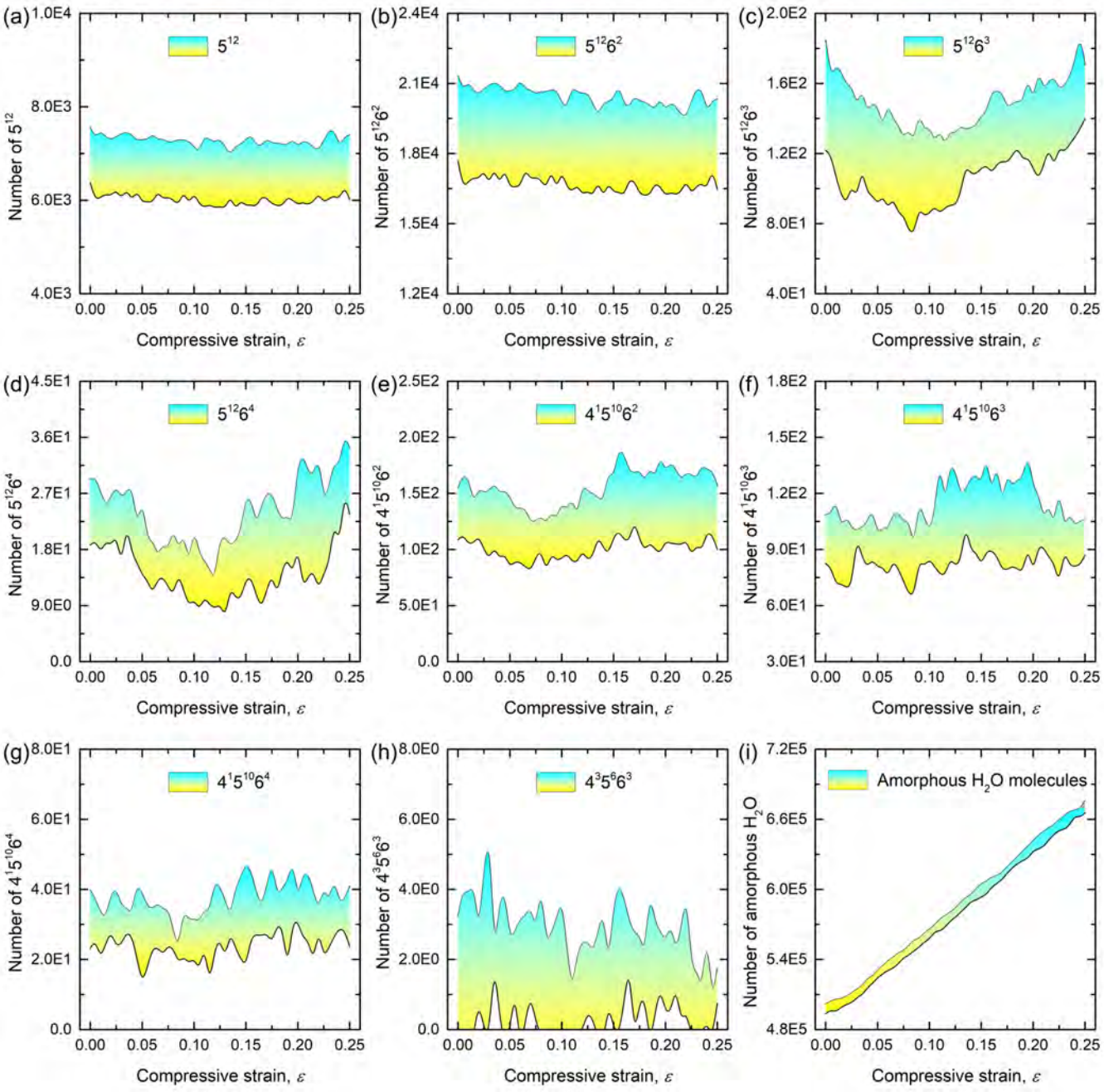

407

408 **Figure S23. The number of identified water cages in sI hydrate polycrystals containing 90% water**

409 **ice under compression.** Eight types of water polyhedral cages and amorphous water ice are respectively

identified during the whole compressive deformation. (a) 5^{12} water cages. (b) $5^{12}6^2$ water cages. (c) $5^{12}6^3$ water cages. (d) $5^{12}6^4$ water cages. (e) $4^15^{10}6^2$ water cages. (f) $4^15^{10}6^3$ water cages. (g) $4^15^{10}6^4$ water cages. (h) $4^35^66^3$ water cages. (i) Amorphous water molecules.

Figure S24.

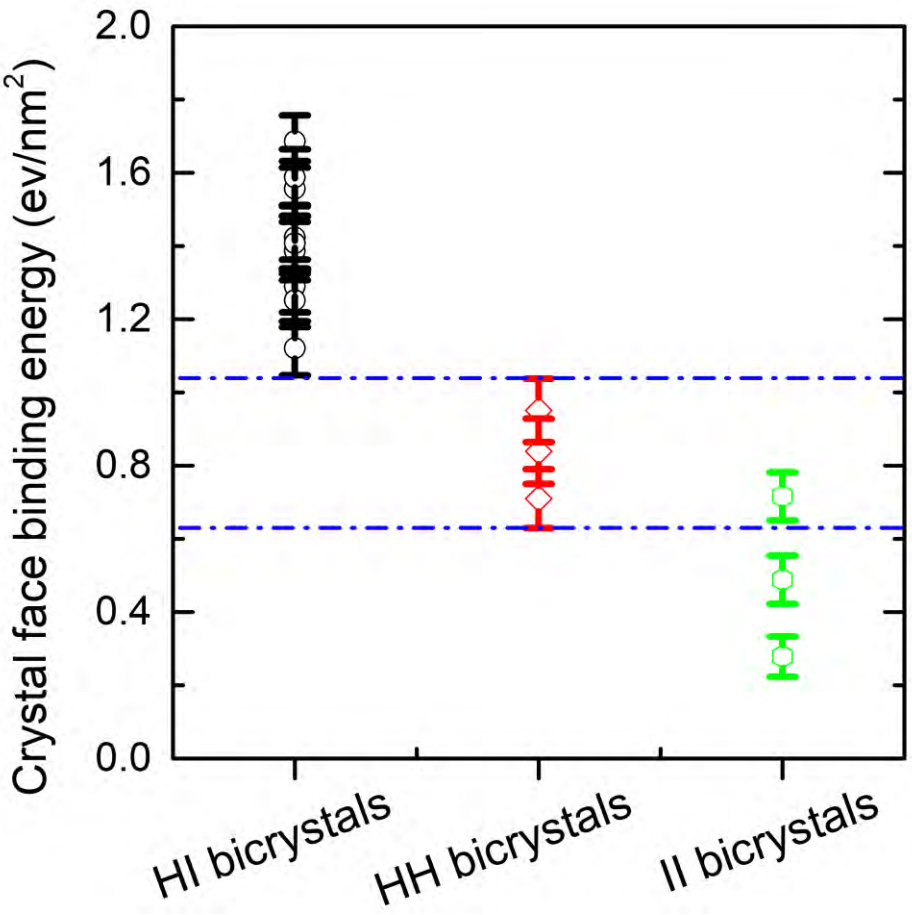

Figure S24. Crystal face binding energy of different bicrystals. Crystal face binding energy of nine hydrate-ice bicrystals with different GB structures, *e.g.*, $\{11\bar{2}0\}|\{1\,0\,0\}$, $\{11\bar{2}0\}|\{1\,1\,0\}$, $\{11\bar{2}0\}|\{1\,1\,1\}$,

$\{0\,0\,0\,1\}|\{1\,0\,0\}$, $\{0\,0\,0\,1\}|\{1\,1\,0\}$, $\{0\,0\,0\,1\}|\{1\,1\,1\}$, $\{01\bar{1}0\}|\{1\,0\,0\}$, $\{01\bar{1}0\}|\{1\,1\,0\}$, and $\{01\bar{1}0\}|\{1\,1\,1\}$ are computed in this work. Crystal face binding energy of three hydrate-hydrate bicrystals with different GB structures, *e.g.*, $\{1\,0\,0\}|\{1\,1\,0\}$, $\{1\,0\,0\}|\{1\,1\,1\}$, and $\{1\,1\,0\}|\{1\,1\,1\}$ are computed in this work. The crystal face binding energy of three ice-ice bicrystals in this figure is modified from the recent work [12].

Figure S25.

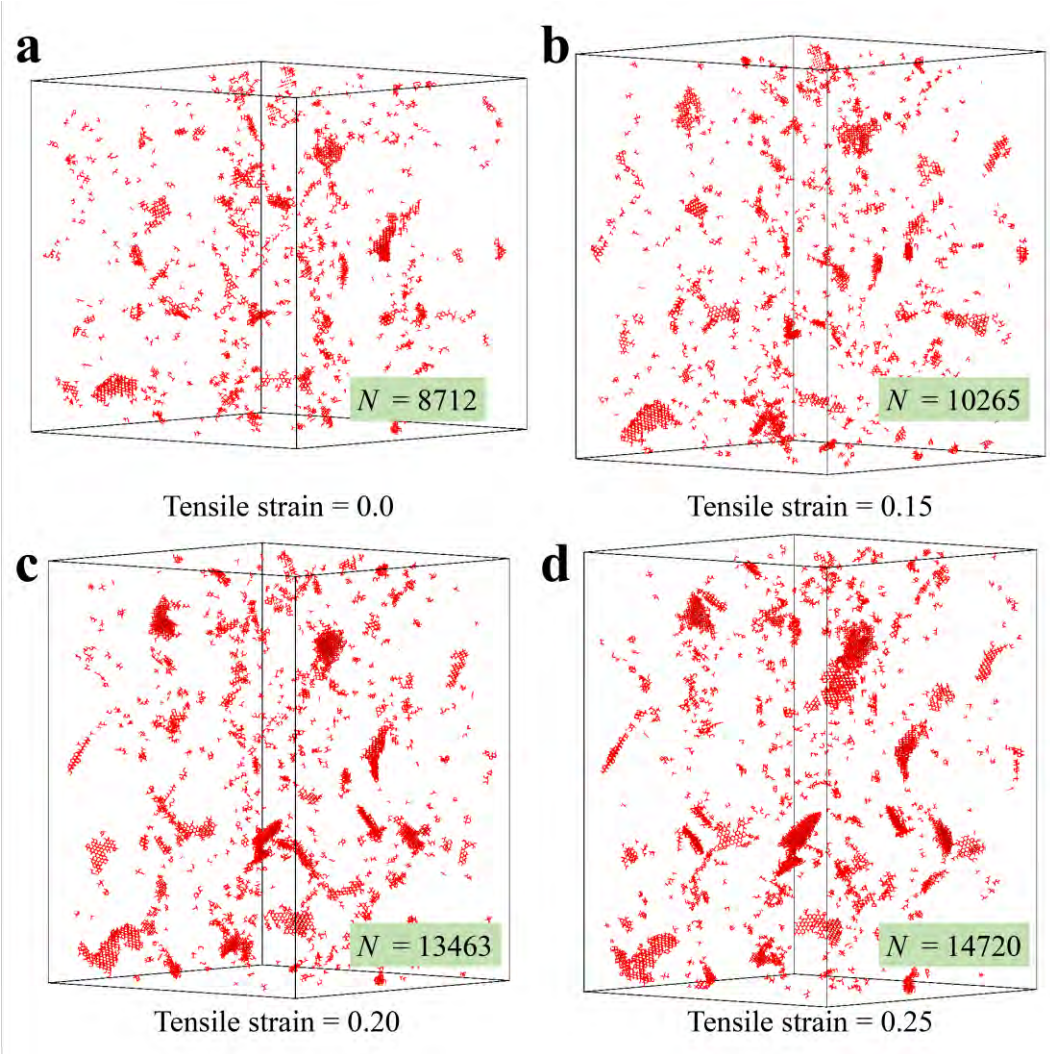

Figure S25. Cubic ice in polycrystals with 100% ice content under different mechanical strains. (a) tensile strain of 0.0 (b) tensile strain of 0.15 (c) tensile strain of 0.20 (d) tensile strain of 0.25. The "*N*" represents the number of water molecules in the form of I_c ice. The structure of I_h and I_c is identified by the structure algorithm [16].

Supplementary Movies:

Movie S1:

Movie S1. Animation of localized hydrate-ice bicrystals with $\{0\,1\,\bar{1}\,0\}|\{1\,0\,0\}$ grain boundary structures under tension strain. Water particles are colored based on their potential energy (-0.40 ~ 0.55 eV). All methane particles are colored by white for clarification.

Movie S2:

Movie S2. Animation of localized hydrate-ice bicrystals with $\{0\,1\,\bar{1}\,0\}|\{1\,0\,0\}$ grain boundary structures under tension strain. Water particles which form hexagonal ice are colored according to the identified type of structural phase; Hexagonal, cubic and unidentified water structures are rendered by orange, sky-blue and blue for clarification, respectively. Water particles which form sI structure methane hydrate are colored by purple. All methane particles are rendered by white for clarification.

Movie S3:

Movie S3. Animation of localized hydrate-ice bicrystals with $\{0\,1\,\bar{1}\,0\}|\{1\,0\,0\}$ grain boundary structures under compression strain. Water particles are colored based on their potential energy (-0.40 ~ 0.55 eV). All methane particles are colored by white for clarification.

Movie S4:

Movie S4. Animation of localized hydrate-ice bicrystals with $\{0\,1\,\bar{1}\,0\}|\{1\,0\,0\}$ grain boundary structures under compression strain. Water particles which form hexagonal ice are colored according to the identified type of structural phase; Hexagonal, cubic and unidentified water structures are rendered by orange, sky-blue and blue for clarification, respectively. Strain-induced dislocations in hydrate-ice bicrystals are illustrated by solid segments. Different colored segments represent different type of dislocation; $1/3\langle 1\,\bar{2}\,1\,0\rangle$, $\langle 0\,0\,0\,1\rangle$, $\langle 1\,\bar{1}\,0\,0\rangle$, $1/3\langle 1\,\bar{1}\,0\,0\rangle$, and unidentified dislocations are rendered by green, yellow, pink, sky-blue and red for clarification, respectively. Water particles which form sI structure methane hydrate are colored by purple. All methane particles are rendered by white for clarification.

Movie S5:

Movie S5. Animation of localized hydrate-ice bicrystals with $\{11\bar{2}0\}|\{1\,0\,0\}$ grain boundary structures under tension strain. Water particles are colored based on their potential energy (-0.40 ~ 0.55 eV). All methane particles are colored by white for clarification.

Movie S6:

Movie S6. Animation of localized hydrate-ice bicrystals with $\{11\bar{2}0\}|\{1\,0\,0\}$ grain boundary structures under compression strain. Water particles are colored based on their potential energy (-0.40 ~ 0.55 eV). All methane particles are colored by white for clarification.

Movie S7:

Movie S7. Animation of localized hydrate-ice bicrystals with $\{0\,0\,0\,1\}|\{1\,0\,0\}$ grain boundary structures under tension strain. Water particles are colored based on their potential energy (-0.40 ~ 0.55 eV). All methane particles are colored by white for clarification.

Movie S8:

Movie S8. Animation of localized hydrate-ice bicrystals with $\{0\,0\,0\,1\}|\{1\,0\,0\}$ grain boundary structures under compression strain. Water particles are colored based on their potential energy (-0.40 ~

0.55 eV). All methane particles are colored by white for clarification.

Movie S9:

Movie S9. Animation of localized hydrate-hydrate bicrystals with {1 0 0}|{1 1 0} grain boundary structures under tension strain. Water particles are colored based on their potential energy (-0.40 ~ 0.55 eV). All methane particles are not shown for clarification.

Movie S10:

Movie S10. Animation of localized hydrate-hydrate bicrystals with {1 0 0}|{1 1 0} grain boundary structures under tension strain. Water particles are colored according to the *von Mises* stress (0 ~ 6 GPa). All methane particles are not shown for clarification.

Movie S11:

Movie S11. Animation of localized hydrate-hydrate bicrystals with {1 0 0}|{1 1 0} grain boundary structures under compression strain. Water particles are colored based on their potential energy (-0.40 ~ 0.55 eV). All methane particles are not shown for clarification.

Movie S12:

Movie S12. Animation of localized hydrate-hydrate bicrystals with {1 0 0}|{1 1 0} grain boundary

structures under compression strain. Water particles are colored according to the *von Mises* stress (0 ~ 6 GPa). All methane particles are not shown for clarification.

Movie S13:

Movie S13. Animation of localized hydrate-hydrate bicrystals with {1 0 0}|{1 1 1} grain boundary structures under tension strain. Water particles are colored based on their potential energy (-0.40 ~ 0.55 eV). All methane particles are not shown for clarification.

Movie S14:

Movie S14. Animation of localized hydrate-hydrate bicrystals with {1 0 0}|{1 1 1} grain boundary structures under compression strain. Water particles are colored based on their potential energy (-0.40 ~ 0.55 eV). All methane particles are not shown for clarification.

Movie S15:

Movie S15. Animation of localized hydrate-hydrate bicrystals with {1 1 0}|{1 1 1} grain boundary structures under tension strain. Water particles are colored based on their potential energy (-0.40 ~ 0.55 eV). All methane particles are not shown for clarification.

Movie S16:

Movie S15. Animation of localized hydrate-hydrate bicrystals with $\{1\ 1\ 0\}|\{1\ 1\ 1\}$ grain boundary structures under compression strain. Water particles are colored based on their potential energy (-0.40 ~ 0.55 eV). All methane particles are not shown for clarification.

Movie S17:

Movie S17. Animation of localized hydrate-ice bicrystals with $\{11\ \bar{2}\ 0\}|\{1\ 0\ 0\}$ grain boundary structures subjected to $\frac{(1\ 1\ \bar{2}\ 0)[0\ 1\ \bar{1}\ 0]}{(1\ 0\ 0)[0\ 0\ 1]}$ directional shear loadings. Except that specific water particles are rendered by gray to monitor grain boundary sliding. Water particles are colored based on their potential energy (-0.40 ~ 0.55 eV). All methane particles are not shown for clarification.

Movie S18:

Movie S18. Animation of localized hydrate-ice bicrystals with $\{11\ \bar{2}\ 0\}|\{1\ 0\ 0\}$ grain boundary structures subjected to $\frac{(1\ 1\ \bar{2}\ 0)[0\ 1\ \bar{1}\ 0]}{(1\ 0\ 0)[0\ 0\ 1]}$ directional shear loadings. Except that specific water particles are rendered by gray to monitor grain boundary sliding. Water particles which form hexagonal ice are colored according to the identified type of structural phase; Hexagonal, cubic and unidentified water structures are rendered by orange, sky-blue and blue for clarification, respectively. Water particles which form sI structure methane hydrate are colored by purple. All methane particles are not shown for clarification.

Movie S19:

Movie S19. Animation of localized hydrate-hydrate bicrystals with $\{1\,0\,0\}\,|\,\{1\,1\,0\}$ grain boundary structures subjected to $\frac{(1\,0\,0)[0\,0\,1]}{(1\,1\,0)[\mathrm{n\,n\,n}]}$ directional shear loadings. Except that specific water particles are rendered by gray to monitor grain boundary sliding. Water particles are colored based on their potential energy (-0.40 ~ 0.55 eV). All methane particles are not shown for clarification.

Movie S20:

Movie S20. Animation of localized hydrate-hydrate bicrystals with $\{1\,0\,0\}\,|\,\{1\,1\,0\}$ grain boundary structures subjected to $\frac{(1\,0\,0)[0\,0\,1]}{(1\,1\,0)[\mathrm{n\,n\,n}]}$ directional shear loadings. Except that specific water particles are rendered by gray to monitor grain boundary sliding. Water particles are colored based on the *von Mises* stress (0 ~ 6 GPa). All methane particles are not shown for clarification.

References

(1) Bernal, J. D.; Fowler, R. H. A Theory of Water and Ionic Solution, with Particular Reference to Hydrogen and Hydroxyl Ions. *J. Chem. Phys.* **1933**, *1*, 515-548.

(2) McMullan, R. K.; Jeffrey, G. A. Polyhedral Clathrate Hydrates. IX. Structure of Ethylene Oxide Hydrate. *J. Chem. Phys.* **1965**, *42*, 2725.

(3) Voronoi, G. F. Nouvelles applications des parametres continus a la theorie des formes quadratiques. Duesieme memoire: recherches sur les parallelodères primitifs. *J. Reine Angew. Math.* **1908**, *134*, 198-287.

(4) Nosé, S. A molecular dynamics method for simulations in the canonical ensemble. *Mol. Phys.* **1984**, *52*, 255-268.

(5) Hoover, W. G. Canonical dynamics: Equilibrium phase-space distributions. *Phys. Rev. A* **1985**, *31*, 1695-1697.

(6) Parrinello, M.; Rahman, A. Polymorphic transitions in single crystals: A new molecular dynamics method. *J. Appl. Phys.* **1981**, *52*, 7182-7190.

(7) Stillinger, F. H.; Weber, T. A. Computer Simulation of Local Order in Condensed Phases of Silicon. *Phys. Rev. B* **1985**, *31*, 5262-5271.

(8) Molinero, V.; Moore, E. B. Water Modeled as an Intermediate Element between Carbon and Silicon. *J. Phys. Chem. B* **2009**, *113*, 4008-4016.

(9) Jacobson, L. C.; Molinero, V. A Methane-Water Model for Coarse-Grained Simulations of Solutions and Clathrate Hydrates. *J. Phys. Chem. B* **2010**, *114*, 7302-7311.

(10) Wu, J.; Ning, F.; Trinh, T. T.; Kjelstrup, S.; Vlugt, T. J.; He, J.; Skallerud, B. H.; Zhang, Z. Mechanical instability of monocrystalline and polycrystalline methane hydrates. *Nat Commun* **2015**, *6*, 8743.

(11) Plimpton, S. Fast Parallel Algorithms for Short-Range Molecular Dynamics. *J. Comput. Phys.* **1995**, *117*, 1-19.

(12) Cao, P.; Wu, J.; Zhang, Z.; Fang, B.; Peng, L.; Li, T.; Vlugt, T. J. H.; Ning, F. Mechanical properties of bi- and poly-crystalline ice. *AIP Advances* **2018**, *8*, 125108.

(13) Bi, Y.; Li, T. Probing Methane Hydrate Nucleation through the Forward Flux Sampling Method. *J. Phys. Chem. B* **2014**, *118*, 13324-13332.

(14) Bi, Y.; Porras, A.; Li, T. Free energy landscape and molecular pathways of gas hydrate nucleation. *J. Chem. Phys.* **2016**, *145*, 211909.

(15) Kelchner, C. L.; Plimpton, S. J.; Hamilton, J. C. Dislocation nucleation and defect structure during surface indentation. *Phys. Rev. B* **1998**, *58*, 11085-11088.

(16) Maras, E.; Trushin, O.; Stukowski, A.; Ala-Nissila, T.; Jónsson, H. Global transition path search for dislocation formation in Ge on Si(001). *Comput. Phys. Commun.* **2016**, *205*, 13-21.